New Views of the Hot and Diffuse Gaseous Universe with the Thermal Sunyaev–Zel'dovich Effect

by

Cameron T. Pratt

A dissertation submitted in partial fulfillment
of the requirements for the degree of
Doctor of Philosophy
(Astronomy and Astrophysics)
in the University of Michigan
2024

Doctoral Committee:

Professor Joel Bregman, Chair
Professor Dragan Huterer
Professor Christopher Miller
Professor Keren Sharon

Cameron T. Pratt
campratt@umich.edu
ORCID iD: 0000-0002-6653-8490

© Cameron T. Pratt 2024

DEDICATION

I dedicate this to my Grandmother who was always so proud of me and pushed me to be a better person.

ACKNOWLEDGEMENTS

First off, I must acknowledge my committee members for their genuine dedication during this dissertation work. Thank you for providing constructive feedback and also offering great advice. Next is my advisor, Joel Bregman, who has my utmost respect and appreciation. Not only did I have the honor to work with one of the most renowned astronomers in the world, but Joel became such an important mentor in my life. Joel has a creative and ambitious scientific mind that is contagious and makes working on difficult tasks enjoyable. He encouraged me to try things I never thought I could do, and this instilled confidence that I will carry with me for the rest of my life. Aside from our scientific relation, Joel is one of those people that makes anyone's life better. He shows empathy when his colleagues experience difficult times, shares fascinating stories about his life, and has an amazing ability to connect people together. Finally, Joel and I have developed a unique friendship that I know will continue to last. I will always remember our conversations about sports, world issues, and other topics most people can only talk about with those they are comfortable with. Thank you for everything, Joel.

I also owe a ton of gratitude to Zhijie Qu as he played a pivotal role in my success during graduate school. I was very lucky to learn from such a skilled scientist, and I am extremely grateful for his willingness to mentor me even when he left for Chicago. Zhijie, thank you for your patience, wisdom, and selflessness. The field of Astronomy is lucky to have you.

I would also like to acknowledge the other brilliant scientists I've worked alongside in Joel's research group. I want to thank Anne Blackwell, who has been with me through most of my graduate career, and is a dear friend. We helped each other get through classes, the pandemic, and attempted to get through Zoom meetings without laughing. I also want to thank Jiangtao Li and Rui Huang. While we all worked on different projects, you still have given me inspiration.

My graduate school experience could not have been as great without the amazing graduate students in our department. I have learned so much from my peers as we studied the physics of our complex Universe. The conversations I have had with my cohort helped me develop intuition that I still use today. Whether it was homework assignments or just talking about interesting topics in the office, I am lucky to have been alongside some of the most talented

individuals—some who I truly believe will change the world. Every graduate student (young and old) has helped me become a better person and I care about them dearly.

I am also very grateful for my teachers who helped me learn in the classroom. Taking the time and effort to be an effective teacher is something I seriously appreciate. I would like to point out a couple of the exceptional instructors who clearly went the extra mile for their students: Eric Bell, Elena Gallo, and Nuria Calvet. I also observed the same efforts from Kayhan Gultekin and John Monnier as I taught undergraduate courses with them.

Additionally, I would like to recognize the remarkable efforts of our department chair, Ted Bergin. From my point of view, Ted could not have ran a more well-oiled ship, and it is very clear that he cares about everyone in the department. Also, the supporting staff have been extremely important in helping me get through the non-scientific parts of graduate school. Thank you for being so cordial and supportive every time we have talked. I also must thank John Theils and Charles Antonelli who have provided me with great computational support during my thesis work.

Lastly, I owe a huge amount of gratitude to the many important people outside of Astronomy. This includes my family and friends who have supported me over six long years. Without them I would have never made it to the finish line. Thank you all for listening to my rants about science, asking me questions, and laying down to look at the stars with me. Finally, I would like to thank my sassy dog, Jake, for giving me joy when I needed it the most.

TABLE OF CONTENTS

DEDICATION ii

ACKNOWLEDGEMENTS iii

LIST OF FIGURES viii

LIST OF TABLES xiv

ABSTRACT xv

CHAPTER

1 Introduction 1

1.1 The Gaseous Content of the Universe 1
1.1.1 Hot Halos 2
1.1.2 Feedback 3
1.1.3 The Missing Baryon Problem 4
1.2 The Sunyaev–Zel'dovich (SZ) Effect 9
1.2.1 Inverse-Compton Scattering 9
1.2.2 Complementary Nature of X-rays and the SZ Effect 10
1.2.3 Noise Contamination in Observations 11
1.2.4 Component Separation 12
1.3 This Thesis 13

2 SZ Scaling Relations of Galaxy Groups and Clusters Near the North Ecliptic Pole 15

2.1 Abstract 15
2.2 Introduction 15
2.3 NEP Sample 18
2.4 Extraction of the SZ Signal 19
2.4.1 Sources of Contamination 19
2.4.2 Uncertainties 20
2.4.3 Unresolved Sources 21
2.4.4 Detections vs. Nondetections 23
2.5 Scaling Relations 24
2.5.1 X-ray Properties 24
2.5.2 Regression Methods 25

2.6 Analysis and Discussion . . . 33
2.6.1 Comparisons of Scaling Relations . . . 33
2.6.2 Caveats . . . 34
2.6.3 Future Work . . . 38
2.7 Summary and Conclusions . . . 39
3 The Resolved Sunyaev–Zel'dovich Profiles of Nearby Galaxy Groups . . . 41
3.1 Abstract . . . 41
3.2 Introduction . . . 41
3.3 Sample of Galaxy Groups . . . 43
3.4 SZ Map Making . . . 47
3.4.1 Frequency Maps . . . 47
3.4.2 Internal Linear Combination . . . 48
3.4.3 Needlet Analysis . . . 50
3.5 SZ Extraction of Galaxy Groups . . . 52
3.5.1 Contamination . . . 52
3.5.2 Uncertainty . . . 55
3.5.3 Stacking Methods . . . 55
3.5.4 Bias . . . 56
3.6 Results . . . 60
3.6.1 Surface Brightness Profile . . . 60
3.6.2 Extended SZ Profile . . . 60
3.6.3 Cumulative Signal . . . 61
3.7 Discussion . . . 63
3.7.1 Data Release Versions . . . 63
3.7.2 Baryon Fraction . . . 63
3.7.3 Bump Feature . . . 65
3.8 Summary . . . 67
3.9 Appendix . . . 69
3.9.1 Individual Surface Brightness Profiles . . . 69
3.9.2 Weighted Average Stacked Profile . . . 71
4 Optimizing NILC Extractions of the Thermal Sunyaev–Zel'dovich Effect with Deep Learning . . . 72
4.1 Abstract . . . 72
4.2 Introduction . . . 72
4.3 Methods . . . 74
4.3.1 Simulations . . . 74
4.3.2 SZ Signal Extraction . . . 77
4.4 Results . . . 86
4.4.1 Residual Power Spectra . . . 86
4.4.2 Bias and Scatter . . . 87
4.4.3 Component Correlation . . . 88
4.4.4 Radial Profiles of Resolved Systems . . . 89
4.5 Discussion . . . 92

4.5.1 Deep-NILC vs. Fixed Spatial Parameter . . . 92
4.5.2 Caveats . . . 92
4.6 Summary . . . 95
4.7 Appendix . . . 96
4.7.1 Wavelet Bands . . . 96
4.7.2 Bias and Scatter of Radial Profiles . . . 96

5 Extracting the Thermal Sunyaev–Zel'dovich Effect with a 3D Convolutional Neural Network . . . 99

5.1 Abstract . . . 99
5.2 Introduction . . . 99
5.3 Methods . . . 101
5.3.1 Simulations . . . 101
5.3.2 Modeling . . . 104
5.4 Results . . . 106
5.4.1 Performance on Test Data . . . 106
5.4.2 Performance on Real Data . . . 108
5.5 Discussion . . . 110
5.5.1 NILC . . . 111
5.5.2 3D-CNN . . . 111
5.6 Summary . . . 112

6 Summary and Future Work . . . 114

6.1 Summary . . . 114
6.1.1 X-ray and SZ Scaling Relations with Low-mass Systems . . . 114
6.1.2 The Resolved SZ Profiles of Galaxy Groups . . . 115
6.1.3 Improving NILC SZ Extractions with Deep Learning . . . 116
6.1.4 Comparison of Current NILC Extractions for Galaxy Groups . . . 118
6.1.5 SZ Extraction with a 3D-CNN . . . 119
6.2 Future Work . . . 121

BIBLIOGRAPHY . . . 123

LIST OF FIGURES

FIGURE

1.1 Simulation showing the stellar and gas spatial distributions for a galaxy group. In the absence of black hole feedback (i.e., AGN feedback), a galaxy group is able to compress gas at small radii and produce highly concentrated star formation. Taken from Figure 1 in Bhattacharya et al. (2008). 5

1.2 The measured baryon fractions for galaxies, galaxy groups, and galaxy clusters as a function of circular velocity taken from Dai et al. (2010). The dotted line near the top denotes the cosmological prediction of f_b, and the dashed line represents a broken power-law that has been fit to the data. The main point of this plot is to show that only the highest mass systems (i.e., galaxy clusters) retain their baryons and the census is consistent with the cosmological value. On the other hand, individual galaxies and galaxy groups show a decreasing f_b with decreasing gravitational potential depth. 6

1.3 Different estimations of the baryon budget over the last decade taken from Figure 1 of Driver (2021). The leftmost data show the measured baryon census taken from Shull et al. (2012), which demonstrated $\sim 30\%$ of the baryons were missing. The middle-left data show the census derived by Nicastro et al. (2018) who claim to have found the missing baryons with marginal OVII detections. The middle-right data show the missing baryons could have been found by Macquart et al. (2020) using fast radio bursts, albeit with large uncertainties. The rightmost data show the results compiled from recent literature and outlining where baryons are bound and unbound. 7

1.4 Plots of the gas, stellar, and baryon fractions taken from Figure 3 in Oppenheimer et al. (2021). The average values and scatter are shown for different simulations. There is clear tension between the results, especially at low masses. The main difference is caused by the different prescriptions of AGN feedback. 9

1.5 General contributions from different emissions near the CMB frequencies. Figure taken from Figure 4 in Planck Collaboration et al. (2020a). 11

2.1 Histogram displaying the amount of contamination stemming from radio sources that were not identified in our manual removal program (see text). The p-values from the two-sided Student's t-test and the Wilcoxon signed-rank test were 0.13 and 0.10 respectively. These are the probabilities of measuring a mean of zero purely by chance. 20

2.2 Best fit power law used to estimate the standard deviation in the Compton parameter as a function of area. 21

2.3 SNR distributions for 62 groups/clusters and 101 random regions near the NEP. Included are normalized histograms (probability distribution functions [PDFs]) and cumulative fractions. The top figures are the distributions in the NILC maps and the bottom are those from the MILCA maps. The vertical and horizontal dashed lines in the right panels indicate where the cumulative fractions of SNRs for the random regions reach 90% and 95%. 24
2.4 The left column shows the SZ data using the UPP and the right column is from the BPP. The solid black lines in each plot represents the best fit using our Bayesian method on bias corrected data described in subsection 2.5.2. The black data with error bars represent the SZ detections with SNR > 1.35 while the red triangles are the nondetections placed at 3σ. The shaded regions in the top two rows denote the 95% confidence bands around the best fit relation. Results from previous studies are also shown for comparison. In the bottom row, the black line and dashed green line appear to lie on top of each other, but the black line is slightly below the dashed green line (1:1 relation). 35
2.5 In both panels, the red line represents the best fit Gaussian curve and the dashed gray line indicates 2σ above the mean. The left panel shows the full distribution of the average values of circles for the entire random array. The right panel is zoomed in to clearly show the outliers. 38

3.1 The predicted S/N of stacked groups by subsequently adding lower mass objects to the sample (note the backwards mass scale). For clarity, the second leftmost datum is the S/N one would expect when stacking the two most massive objects in the sample. The stacked S/N appears to stop increasing around $M_{500} \sim 10^{13.6}$ $M_\odot$ and we used this as a threshold for the lower mass limit. 45
3.2 Needlet window functions used to filter the difference maps in multipole space. These filters captured features on scales $\gtrsim 10^{'}$ and $\lesssim 10^{o}$ 51
3.3 (*left panel*) SZ two-point angular autocorrelation profiles for different y-maps binned by $\frac{1}{4}^\circ$ increments with the first bin omitted. Sources of contamination such as the galactic plane, galaxy clusters, and point sources, were masked for this calculation. Uncertainties were determined in a Monte Carlo manner. PR2NILC showed the strongest background correlations on most angular scales while PR3NILC and PR4NILC appeared similar beyond 2°. (*right panel*) Same as the top but represents the angular cross-correlation between the y-maps and the 857 GHz map which was used as a proxy for the dust emission. Once can see strong anti-correlations on scales $\sim 1^\circ$ and 3°. 54

3.4 Results of stacking 100 simulated galaxy group profiles that were injected into the *Planck* and *WMAP* frequency maps, and recovered in the PR4NILC maps. (*top panel*) The blue squares represent the recovered stacked profile using the bootstrap method, and the orange stars were calculated with a weighted average. Strong sources of contamination were removed before each extraction, and bias corrections were applied from the bottom panel. The dotted line denoted the input signal defined to be the median of all AGN 8.0 profiles from L15, each convolved with the PSF. (*bottom panel*) The open markers are the estimated bias values calculated from "refined" SZ profiles. They represent the simulated profiles after subtracting off the real SZ portion covering the same region, leaving behind a contamination-free signal. Refined profiles quantified the amount of bias introduced by our NILC algorithm and stacking procedures, which was $\lesssim 5\%$. . 57

3.5 The stacked sample of galaxy groups using three different y-maps. PR2NILC (red triangles) represents on of the public y-maps while PR3NILC (green diamonds) and PR4NILC (black squares) represent the extractions from our own NILC extraction using later versions of *Planck* data with the addition of *WMAP* data. The stacked values and their uncertainties were calculated using the bootstrap method. Uncertainties are shown only for PR4NILC for clarity, but the errors for the other profiles are similar. Bias corrections were applied to PR3NILC and PR4NILC data, but this was not possible for PR2NILC data. The dotted gray line is the predicted profiles from A10, while the dashed and solid lines are two different AGN feedback models from L15. 58

3.6 Significance profiles when trying to measure a bump feature both in the simulated and real data sets. First, AGN 8.0 profiles were fit to the data outside of the bump region (1.3 - 2.9 R_{500}). Then residuals were calculated between the best-fit model and the data over the bump region. The significance was calculated by simply dividing each residual by the uncertainty of the measurements. 61

3.7 Cumulative cylindrically integrated profiles. The black data represent the cumulative $Y_{\rm cyl}$ for the PR4NILC data while the different lines denote the three model predictions considered in this study. 62

3.8 A randomly selected patch showing the difference between PR4NILC and PR3NILC. The region is centered at the coordinates ($l = 161.431^\circ$, $b = 84.516^\circ$) with a field-of-view $22^\circ \times 22^\circ$. There are clear striping features that coincide with the *Planck* scanning pattern. Since the NILC method was the same for PR3NILC and PR4NILC, the difference in the y-maps is purely due to data processing. . . 64

3.9 Individual SZ surface brightness profiles. Red triangles, green diamonds, and black squares represent the profiles from PR2NILC, PR3NILC, and PR4NILC respectively. Uncertainties are shown only for PR4NILC and were estimated locally depending on the size and location of the extraction annulus (see subsection 3.5.2). The PCG identification represents the objects in Table 3.1; the corresponding BCG IDs are provided as well. Blue lines indicate the 1° scale for each object. 70

3.10 Weighted average stacked profiles using the full (blue squares), low-mass (orange triangles), and high-mass (purple diamonds) samples. The data are slightly offset on the horizontal axis for clarity; the blue and orange data are shifted to the left and the right of each purple diamond respectively. The weighted stack was calculated using the empirical variance estimated for each local field. The low-mass sample does not show a value for the innermost bin because it was smaller than the 20' exclusion radius (i.e., 0.25 $R_{500} < 20'$). 71

4.1 An example of how different values of Γ affect the NILC extraction of the SZ signal. The images in the top row are $10°x10°$ and centered around a strong simulated SZ source. The leftmost panel denotes the input SZ signal. The panels to the right show residuals between the input and reconstructed y-maps using three values of Γ. The eight panels below display the different estimates of the center pixel in the above images. They are shown as a function of wavelet scale and Γ. The best possible NILC solution given an array of Γ values are shown as filled circles; this is the closest estimate to the true value which is shown as a horizontal line in red. Summing the true values (red lines) on each wavelet scale yields the total SZ signal. The main point of this plot is to demonstrate how the choice of Γ impacts the estimate of the SZ signal. It also shows that larger values of Γ are typically preferred when performing extractions where the SZ signal is strong. 81

4.2 Same as Figure 4.1 except for the change in location of the sky. This example is centered around a pixel with a weak SZ signal, but it is also centered around a known radio source from the simulations. Smaller values of Γ were preferred in this scenario, which were generally true for pixels with weak SZ signals and/or strongly contaminated regions. 82

4.3 Average residual power spectra for the three validation y-maps. The gray line denotes the residual for the best possible NILC solution and black is the results from Deep-NILC. The blue, green, and red are the residuals for $\Gamma = 1, 4.64, 10$ respectively. 86

4.4 (top-left) The fractional bias as a function of SZ signal strength. We show the results for the three nominal values of Γ, Deep-NILC, and the best possible NILC solution. (top-right) Same as top-left panel but for the empirical scatter. (bottom-left) Displays the contributions from each source of error. The dashed lines show the absolute values of the top-left panel, solid lines show those from the top-right panel, and the circles denote the total contribution from both components. (bottom-right) The expected S/N for the pixel values. The y-axis is truncated at S/N= 1 and where $\log_{10}\mathrm{y} = -5$. 88

4.5 Cross-correlation coefficients using the residuals from y', Deep-NILC, and the three nominal values of Γ. (left) Correlation between the residuals and the SZ signal. The best possible NILC solution is in gray and lies just below zero for all ℓ. (right) Same as left panel but for the CIB. The main takeaway here is that Deep-NILC (black line) closely followed the best NILC solution (gray line) which was desirable. 90

4.6 The left column shows the stack of ten radial profiles for three resolved signals. The right column shows the cumulative SZ flux. The group-, Coma-, and Virgo-like signals are shown in the top, middle and bottom panels respectively. The results from different values of Γ are shown as stars, those from Deep-NILC as black circles, and the true signal as cyan squares. The stars and circles are slightly offset in the horizontal direction to help with visualization. Extractions for Γ = 4.64 are not shown in the group- and Coma-like panels to avoid overcrowding. The black line shows the profile that was injected into the simulated y-map, and the dotted brown lines indicate the positions of 1, 2, and 3 R_{500}. The error bars show the standard deviation of the mean for each annulus. The cyan points do not exactly match the input profile since the injected signal has been convolved with other nearby SZ signals. The error bars on the cyan squares are the statistical fluctuations of the true signal within the stack after some masking. The main point of this plot is to show how well resolved signals are recovered with Deep-NILC and different values of Γ. 93
4.7 Harmonic window functions as a function of multipole. 97
4.8 The average bias, scatter, and total error for galaxy group-like signals are shown in the top, middle, and bottom panels respectively. These quantities are shown in the left column while they are shown as a fraction of the SZ signal in the right column. 97
4.9 Same as Figure 4.8 but for a Coma-like system. 98
4.10 Same as Figure 4.8 but for a Virgo-like system. 98

5.1 Flowchart describing the 3D-CNN architecture. D represents the dimension of the output after passing through that layer. The first two dimensions were always 128x128 since padding was the same for all layers. For the 3D layers, the third dimension remained at 12 which represents the number of spectral bands, and the fourth dimension represented the number of feature channels. A leaky ReLU activation function was also applied at the end of each 3D convolution layer; a linear activation was used for the output, which comes from the 2D point-wise convolution. 103
5.2 The top panel shows the MSE for both the training set (blue) and the test set (orange) as a function of training epoch. The MSE was used as the training loss function. The bottom panel shows the same as the top panel but for the MAE. These plots demonstrate that training was able to eventually converge in both metrics. 106

5.3 An example of the extraction for a random patch of sky in the test set ($l = 96.1°$, $b = -59.6°$). The left column presents data from the NILC extraction, and the right column is that for the NN. The middle column shows the distribution of pixel values for the respective rows. The top row shows the true values i.e., the SZ signal that was input to the simulations. The NILC pixel values are represented by the blue histograms while the NN data are shown in orange. In order to compare the two different extractions, we subtracted their median values to center the distribution around zero. The second row shows the results from the NILC and 3D-CNN predictions, and the last row shows the residuals between the input y-map and the recovered y-map. 107
5.4 Statistical evaluations of the NILC and 3D-CNN methods. The left panel shows the results for 250 patches using one of the full-sky test maps. The solid blue line shows the median variance and the dashed blue lines denote the 5%-95% spread of the pixels in the ground truth map; the same is shown in green for the WebSky simulations. The squares and error bars show the same statistics but for the recovered y-maps. The middle panel shows the same as the left but for real data. Stars represent the calculated σ_y values after masking known galaxy groups and clusters. We do not show horizontal lines in the middle panel since we do not know the ground truth. In the right panel, the open histograms show the distributions of simulated data, and the filled represent the real data. 108
5.5 Example 2D cutouts for the 3D-CNN and NILC extractions of the real sky. The field was randomly selected and centered around the Galactic coordinates of $l = 227.61°, b = 53.52°$. A few known galaxy clusters are present in this field which were identified in all-sky X-ray and SZ catalogs (Piffaretti et al. 2011, Planck Collaboration et al. 2016a) at pixel positions near (x=60,y=100) and (x=45,y=50). 109

6.1 Estimated gas fractions compiled from various X-ray selected studies taken from Figure 7 of Eckert et al. (2021). The result from Pratt et al. (2021) is shown as a black cross, which lies at the lower range of X-ray values. 117
6.2 Comparison of different results for the stacked sample of galaxy groups studied in Chapter 3. Shown as shaded bands are the results from: (black) Deep-NILC, (green) the NILC solution from Pratt et al. (2021), (red) the publicly available NILC map from Planck Collaboration et al. (2016b), (yellow) one of the results from McCarthy & Hill (2024), (blue) the MILCA solution also released by Planck Collaboration et al. (2016b), and (magenta) the NILC solution from Chandran et al. (2023). The mean of all six solutions are shown as black circles. 120

LIST OF TABLES

TABLE

2.1 The first four columns and column 6 are directly from Henry et al. (2006). Column 5 is the X-ray luminosity in 0.5-2.0 keV band within R_{500} (see text). Column 7 is the halo mass within R_{500} estimated from the $M_{500} - T_X$ relation from Kettula et al. (2015) given the temperature in column 6. Column 8 is the X-ray analog of the SZ luminosity within R_{500}. Column 9 is the SZ signal-to-noise ratio calculated using Equation 2.5. Column 10 is the total SZ flux computed from Equation 2.4. 29

2.2 Estimated parameters for various scaling relations under the assumption that all systems follow the "universal pressure profile" from Arnaud et al. (2010). 30

2.3 Same as Table 2.2 but assuming each system follows the mass dependent pressure profile from Battaglia et al. (2010). 31

2.4 Presented are the coordinates of the regions which have high SNR values (SNR ≥ 4) and the number of groups/clusters within a $10'$ radius according NED. *a* - These are overlapping regions that contain the same cluster within $10'$. *b* - This region contains a confirmed cluster detected by Gioia et al. (2003) which was the optical identification program used to construct the X-ray NEP catalog. Henry et al. (2006) did not include this in their catalog as it did not meet all requisites for their final catalog. 36

3.1 The first column (1) is the "PCG" identification number used to distinguish galaxy groups in KT17; (2) and (3) are the galactic coordinates in degrees; (4) is the identification of the system in the MCXC catalog if it existed; (5) is the logarithm of the estimated mass (in solar units) within R_{500} ; (6) is the angular size of R_{500} for each system in arcminutes; (7) is the recessional velocity of each galaxy group; (8) is the measured distance and (9) is its fractional uncertainty; (10) is the NGC identification for the BCG. 46

4.1 Neural Network Parameters 85

4.2 Percent Difference in Y. 91

5.1 Standard deviation values of the real frequency data that were used as normalization factors to the input data. 104

ABSTRACT

Most of the baryonic matter in the Universe is expected to exist as diffuse gas surrounding galaxies, galaxy groups, and galaxy clusters. Detecting this is a difficult task, especially when it is too diffuse to see in X-ray emission. The Sunyaev-Zel'dovich (SZ) effect offers an independent view of cosmological gas by measuring spectral distortions in the cosmic microwave background (CMB). In this thesis, I present the process of extracting SZ maps (y-maps) from *Planck* and *WMAP* data. These y-maps are used to estimate the gaseous contents around individual systems, particularly galaxy groups. Moreover, part of this work includes the first resolved SZ signal measured from a stack of nearby galaxy groups. Then I describe the efforts made improve the quality of current SZ data using machine learning. Specifically, I discuss two methodologies to extract the SZ signal with deep learning. Finally, I will conclude with a statement regarding the current state of SZ data and the notable caveats of using mock data and supervised learning to make real-world predictions.

CHAPTER 1

Introduction

Observational cosmology relies on our ability to map the matter and energy contents of the Universe. While this has already been accomplished for the most massive galaxy clusters, much of the baryons are still unaccounted for in lower density regions. It is imperative to be able to detect such gas since its presence, or absence, will dictate the future of cosmological models and, ultimately, will put ΛCDM to the test. In order to do this, we need to understand the vast baryonic reservoir that pervades our Universe.

1.1 The Gaseous Content of the Universe

Around 380,000 years after the Big Bang, the Universe consisted of mostly free-streaming photons and neutral hydrogen. At this early time, no coherent structures had formed, however, there still existed density perturbations. As the Universe continued to expand and cool, neutral hydrogen gas collapsed into molecular clouds which created the seeds for the first episode of star formation.

The first generation of stars were likely very massive, producing high amounts of ionizing radiation which commenced the era of reionization (Klessen & Glover 2023). After living relatively short lives, these stars ended in supernovae (SNe) explosions, and dispersed their materials into their surroundings. This included heavy elements, known as metals (i.e., heavier than hydrogen), which are generated inside stellar cores via nuclear fusion. Much of the SNe debris could have escaped the potential wells of the primordial dwarf galaxies, but a non-trivial amount remained to form the next generation of stars.

As the over-dense regions of the Universe continued to grow, the gravitational potentials eventually became deep enough to prevent SNe material from reaching the escape velocity of the first galaxies. At the same time, pristine gas was being accreted at an accelerated rate. These inflowing and outflowing components mixed to create multi-phase atmospheres. As gravitational energy was converted into kinetic energy, gas temperatures started to rise.

As some point, the thermal pressure stabilized against gravity and formed structures known as hot halos.

1.1.1 Hot Halos

Hot halos are the result of collapsed gas that is at or near virial equilibrium. In this scenario, one can assume particles are moving at the circular velocity

$$v_c = \sqrt{\frac{GM}{R}} \tag{1.1}$$

where M is the mass enclosed within radius R, and G is the gravitational constant. Then we can use the circular velocity to estimate some thermodynamic properties of the gas. The internal energy is related to the kinetic energy (per particle) as

$$\frac{1}{2}\mu m_H v_c^2 = \frac{3}{2}k_B T_{vir} \tag{1.2}$$

where k_B is the Boltzmann constant, m_H is the mass of hydrogen, and μ is the mean molecular weight which is ≈ 0.6 for ionized cosmic gas, and T_{vir} is the virial temperature. Putting typical values into Equation 1.2, the hot halos from galaxies to galaxy clusters can range from $\lesssim 10^6$ K to $\gtrsim 10^7$ K respectively.

Because halos are heated via gravitational collapse, one might expect them to heat in a self-similar manner since gravity is a scale-free force. Using the arguments above, we can write a scaling relation between the halo mass and the temperature. The virial theorem tells us

$$KE \propto U \propto PE \tag{1.3}$$

where KE is the total kinetic energy, U is the total internal energy, and PE is the total potential energy. From the ideal gas law, we know $U \propto NT$; and the total gravitational energy is $PE \propto \frac{M^2}{R}$. We then define some radius, R_Δ, that is the radius where the average enclosed density is Δ times the critical density of the Universe, ρ_c, where

$$R_\Delta = \sqrt[3]{\frac{M_\Delta}{\frac{4}{3}\pi\Delta\rho_c}} \tag{1.4}$$

. From here one can see that

$$T_\Delta \propto \frac{M_\Delta}{R} \propto M_\Delta^{\frac{2}{3}} \tag{1.5}$$

. Equation 1.5 says the temperature should scale self-similarly with the mass of the system.

This argument holds to first-order as it is really only applicable for collisionless dark matter. The electromagnetic interactions between baryons, however, can cause significant deviations from this relation.

Baryons can lose energy via the escape of radiation which causes gas to cool and condense. The time scale at which this occurs is given by

$$\tau_{cool} = \frac{3(n_e + n_i)k_B T_e}{2n_i^2 \Lambda(T_e, Z)} \tag{1.6}$$

where n_e and n_i are the electron and ion number densities respectively, T_e is the temperature of the electrons, Z is the metallicity, and Λ is the cooling function (Dopita & Sutherland 2003). Assuming Bremsstrahlung emission and typical metallicty values, one can approximate the cooling time as

$$\tau_{cool} \sim 5 \times 10^7 n_i^{-1} T_8^{\frac{1}{2}} [\text{years}] \tag{1.7}$$

where T_8 is the temperature in units of 10^8 Kelvin and n_i is in cm^{-3} (Dopita & Sutherland 2003). In order for stars and galaxies to form, the τ_{cool} must be $\lesssim$ the free-fall time, which is generally true toward the centers of hot halos (Stern et al. 2019).

Near the centers of galaxy clusters, the density is so high such that gas can efficiently cool, and this can explain the observed cool core phenomenon (Rossetti & Molendi 2010, Hudson et al. 2010). One could then imagine that such efficient cooling should cause a plethora of star formation to occur inside cool cores. However, the observed star formation rates inside galaxy clusters do not live up to the theoretical prediction—this is the well-known cooling flow problem (Gaspari et al. 2013, McDonald et al. 2018). It is now understood that inner halo gas manifests an entropy floor, alluding to the idea that some external mechanisms that are hindering the runaway cooling effect (Roychowdhury et al. 2004, McNamara & Nulsen 2007a).

1.1.2 Feedback

Halo gas provides galaxies with the fuel necessary for star formation. In return, increased star formation yields higher SNe activity which provides pressure against the accreting gas. Accreting halo gas also feeds the supermassive black holes (SMBHs) that reside at the center of galaxies. Such processes impose feedback via thermal heating and mechanical outflows, suppressing the further accretion of halo gas. There is indication, however, that the feedback strength cannot be too large such that it destroys galaxies as a whole, so there must exist some balance (Gaspari et al. 2013).

Observations show that SNe feedback is dominant in galaxies of $M_h < 10^{12} M_\odot$ which is

reflected in the stellar mass-halo mass relation (Behroozi et al. 2013). At higher halo masses, star formation decreases and SNe feedback becomes less important, but AGN feedback plays a more pivotal role. AGNs inside galaxy clusters often exhibit large radio lobes that drive outflows and inflate the pressure on accreting gas (Giodini et al. 2010, Pasini et al. 2020). At low redshifts ($z \lesssim 1$), this feedback is enough to account for the lack of observed star formation inside galaxy clusters (Gaspari et al. 2013, Prasad et al. 2020). Furthermore, AGN jets appear to only affect the core of galaxy clusters ($\frac{R}{R_{500}} < 0.15$) as they encounter resistance from the weight of the outer gas (Pratt et al. 2009, Mantz et al. 2016). Beyond the core region, the thermodynamic properties of cluster gas behaves remarkably self-similar, making them excellent mass proxies.

Galaxy groups encapsulate the middle-ground between individual galaxies and galaxy clusters. In this regime, it is theorized that the binding energy of the gas becomes comparable to AGN feedback energy, so it is possible for some of the gas to be expelled beyond the virial radius (Bhattacharya et al. 2008, McCarthy et al. 2011, Le Brun et al. 2015, Paul et al. 2017, Farahi et al. 2018). A visualization of this scenario is shown in Figure 1.1. It shows the effect of SMBH feedback on the distribution of halo gas and star formation. Specifically, gas gets removed from the center and pushed to the outskirts. As a result, the star formation becomes further distributed from the center of mass. This displacement of high-entropy gas into the cosmic web is the preferred explanation to the "missing baryon problem".

1.1.3 The Missing Baryon Problem

According to ΛCDM, the energy budget of the Universe today is shared among three major components: dark energy, dark matter, and baryonic matter. Formally, the density parameter, $\Omega_x = \frac{\rho_x}{\rho_c}$, for all components must sum to unity for a flat Universe to exist

$$\Omega_\Lambda + \Omega_{\rm DM} + \Omega_{\rm b} = 1 \tag{1.8}$$

. In concordance with observations of the CMB power spectrum, we know the relative contribution from each component as a function of redshift. In particular, we calculate the baryon fraction $f_b = \Omega_{\rm b}/\Omega_{\rm DM} \approx 0.17$ (Planck Collaboration et al. 2020b). This value should not change as a function of redshift as dark matter and baryonic matter share the same equation of state. Observations at high redshifts are consistent with this value (Weinberg et al. 1997), however, it is severely underpredicted at low redshifts ($z \sim 0$). More specifically, we find good agreement in $\Omega_{\rm DM}$, but $\Omega_{\rm b}$ falls short of the cosmological prediction, and this has become known as the "missing baryon problem".

Today, baryonic matter exists over a range of states inside galaxies. The amount locked

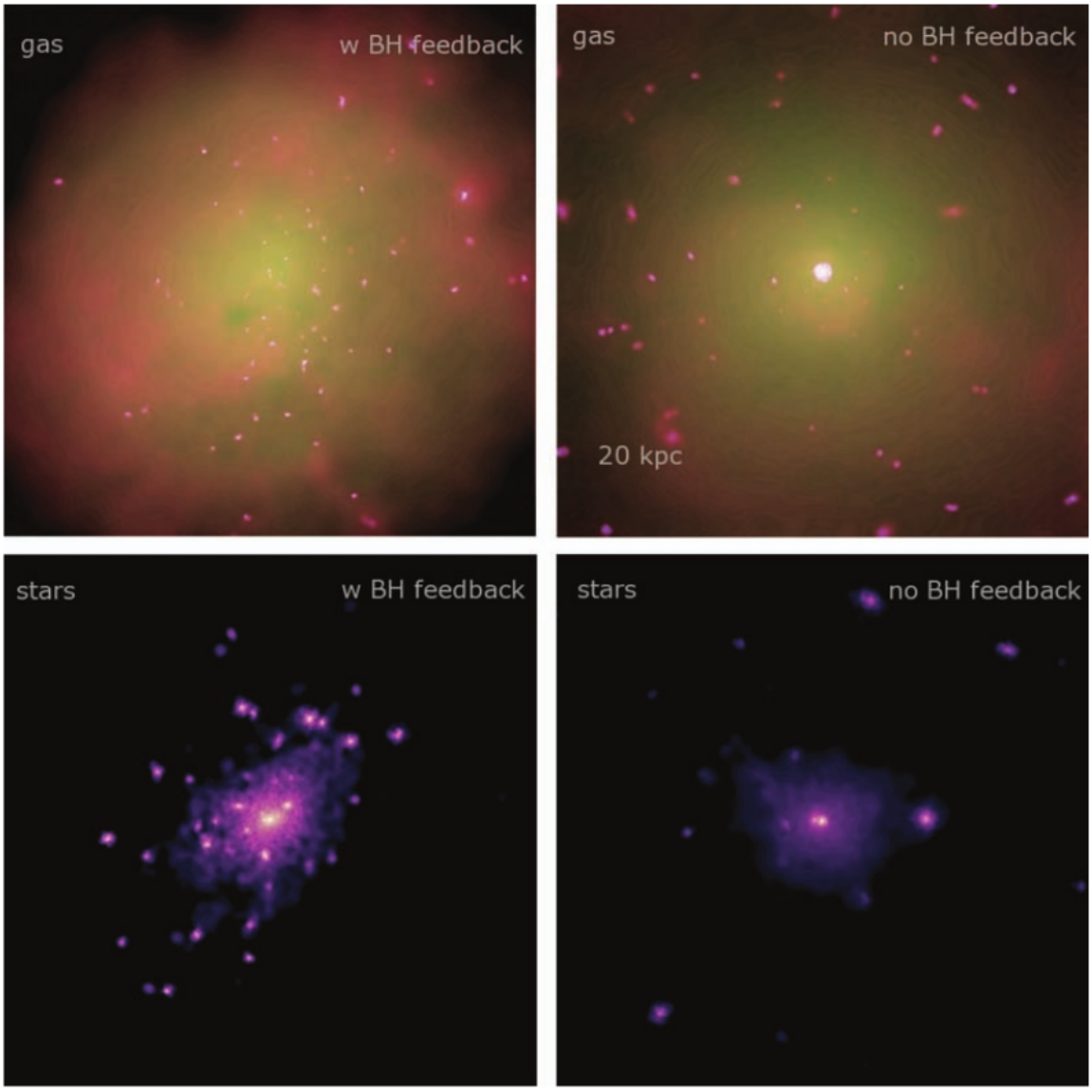


Figure 1.1 Simulation showing the stellar and gas spatial distributions for a galaxy group. In the absence of black hole feedback (i.e., AGN feedback), a galaxy group is able to compress gas at small radii and produce highly concentrated star formation. Taken from Figure 1 in Bhattacharya et al. (2008).

away in stars is usually inferred from the optical and/or infrared (IR) luminosities of a galaxy. In general, it is more appropriate to use IR wavelengths since most of the stellar mass resides inside low-mass stars. Using apparent magnitudes and colors, one can get an estimate of the mass-to-light ratio (Bell et al. 2003). The interstellar gas mostly exists as molecular (H_2), neutral (HI), or ionized hydrogen (HII). Molecular hydrogen is typically inferred using CO line emission since H_2 is highly self-shielding, HI is directly observed via the 21 cm

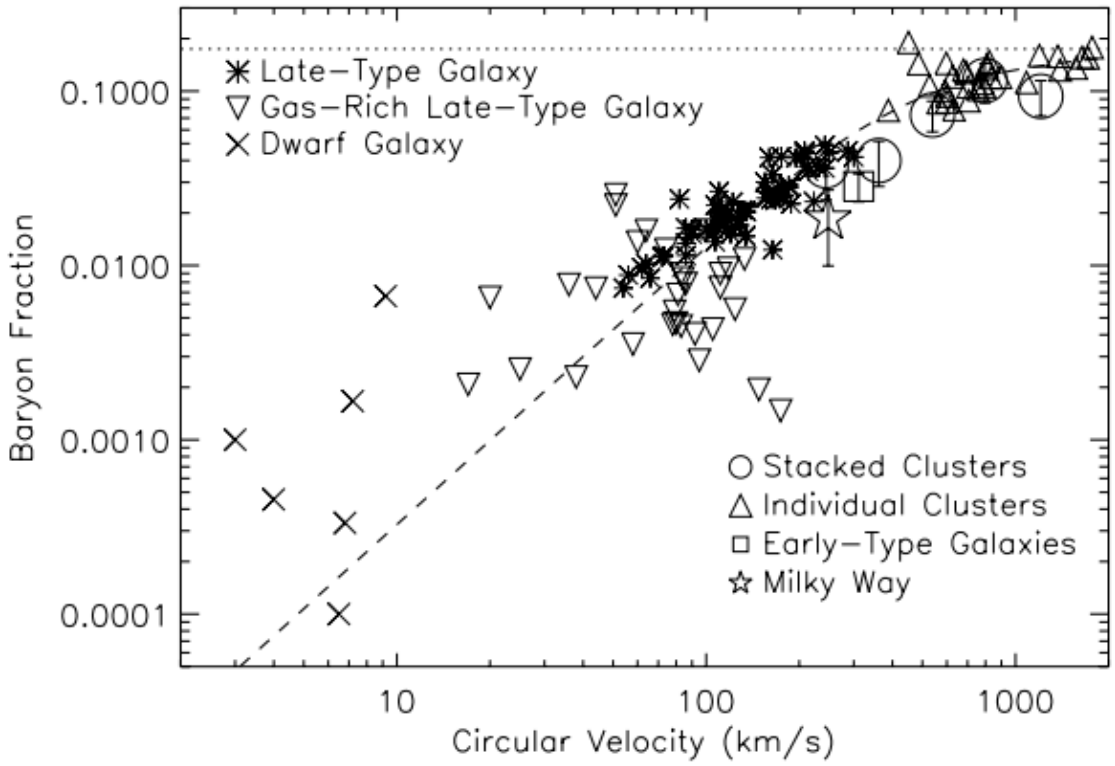


Figure 1.2 The measured baryon fractions for galaxies, galaxy groups, and galaxy clusters as a function of circular velocity taken from Dai et al. (2010). The dotted line near the top denotes the cosmological prediction of f_b, and the dashed line represents a broken power-law that has been fit to the data. The main point of this plot is to show that only the highest mass systems (i.e., galaxy clusters) retain their baryons and the census is consistent with the cosmological value. On the other hand, individual galaxies and galaxy groups show a decreasing f_b with decreasing gravitational potential depth.

hyperfine structure line, and HII is detected from the Balmer series. For most galaxies in the low-z Universe, the total contribution from stars and interstellar gas to the predicted baryon budget is $< 10\%$ as shown in Figure 1.3. Thus, galaxies appear to be "missing" their baryons at low-z.

The proposed hypothesis to the missing baryon problem is there is an invisible gas component beyond the stellar domain. The mixture of inflowing and outflowing gas inside a galaxy's dark matter halo constitutes the circumgalactic medium (CGM; Donahue & Voit 2022). This includes pristine inflows as well as outflows that get recycled back into star-forming regions. Much of this gas is hot enough to produce ions at ultraviolet (UV) energies, known as the warm-hot CGM, and these have been mapped via decades of QSO abosorption studies (Stocke et al. 2006, Bregman 2007, Tripp et al. 2008, Stocke et al. 2014). Moreover, galaxies commonly live inside galaxy groups which have virial temperatures at higher

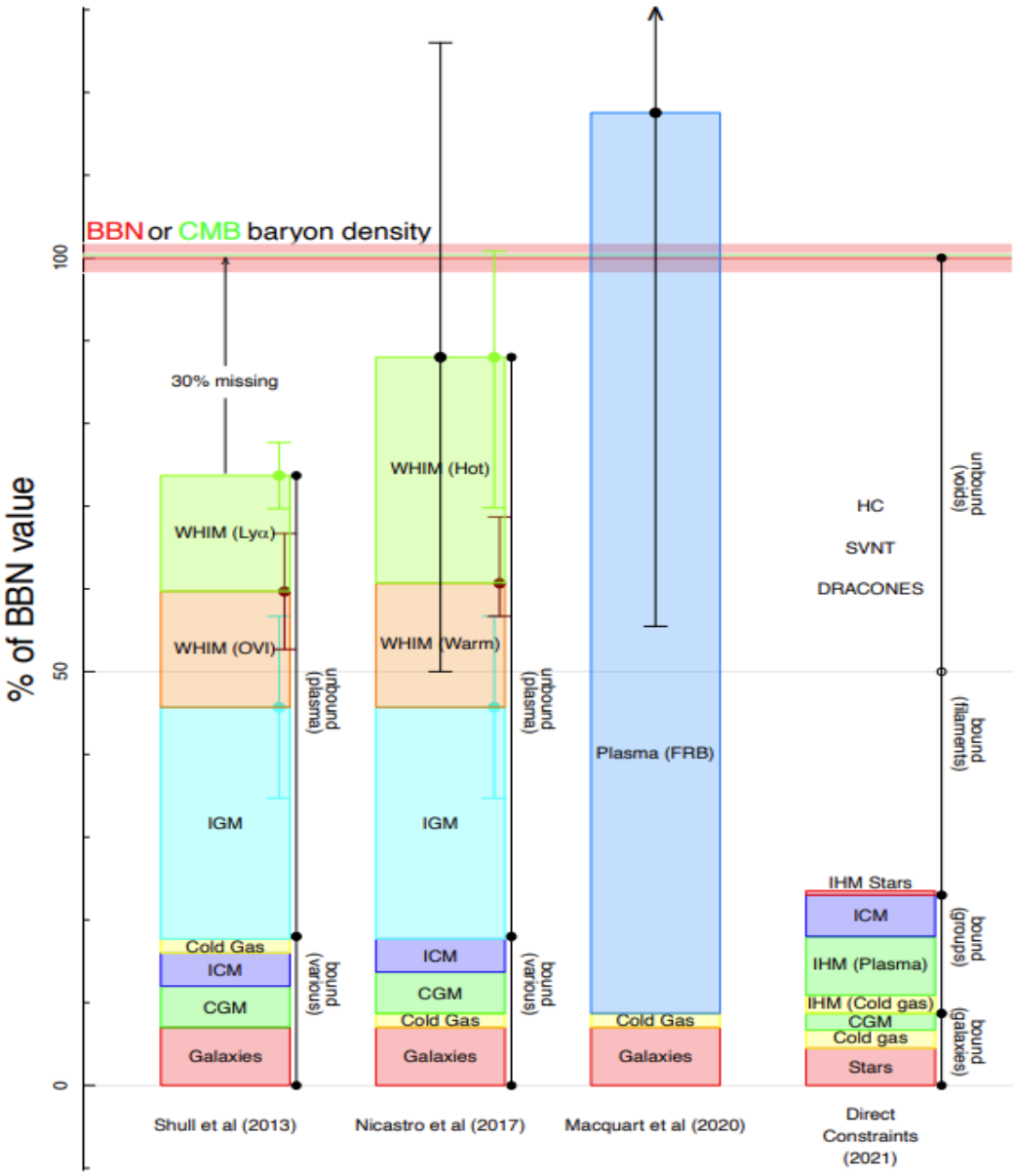


Figure 1.3 Different estimations of the baryon budget over the last decade taken from Figure 1 of Driver (2021). The leftmost data show the measured baryon census taken from Shull et al. (2012), which demonstrated $\sim 30\%$ of the baryons were missing. The middle-left data show the census derived by Nicastro et al. (2018) who claim to have found the missing baryons with marginal OVII detections. The middle-right data show the missing baryons could have been found by Macquart et al. (2020) using fast radio bursts, albeit with large uncertainties. The rightmost data show the results compiled from recent literature and outlining where baryons are bound and unbound.

UV energies. Furthermore, some galaxy groups, and certainly most galaxy clusters, are hot enough to produce/absorb X-rays.

From Figure 1.3 one can see that most of the detected baryons are not associated with collapsed structures or their halos. Instead, they lie in the vast space between galaxies known as the intergalactic medium (IGM). Much of this material is neutral hydrogen, and can detected via Lyα absorption—. OVI also exists in the IGM, along with broad Lyα absorption, which indicates the presence of a warm-hot intergalactic medium (WHIM; Danforth & Shull 2005). According to Shull et al. (2012), adding all these components still cannot account for $\sim 30\%$ of the baryons.

It is believed the remaining baryons exists in a hotter ($T > 10^6$ K) and more diffuse medium than what has been previously detected. The best tracers for such gas are OVII and OVIII absorption lines, which occur at X-ray energies. Unfortunately, current X-ray telescopes are not well-suited for this task (Bregman 2007). Nevertheless, a few marginal detections of OVII have been reported in external L* galaxies (Nicastro et al. 2023, Mathur et al. 2023), as well as the Milky Way (Locatelli et al. 2024). These studies claim to close the baryon census, albeit with notable uncertainties.

For galaxy clusters, most of the baryons exist in the hot ICM and are easily detected by X-ray telescopes. Because their large gravitational wells can provide strong resistance against AGN feedback, their observed f_b values are near the cosmological prediction as seen in Figure 1.2. At lower masses, there is a clear trend of decreasing baryon fraction with decreasing halo mass. In fact, X-ray observations of galaxy groups and poor clusters typically can only account for half of the predicted baryons (Eckert et al. 2021). Moreover, most of such studies contain X-ray selected samples which are known to be selectively biased toward virialized systems. Such systems are likely at the "tip of the iceberg" and not representative of the typical population. Many galaxy groups are X-ray faint (Mulchaey 2000) either because they are dynamically young or experienced strong episodes of feedback. This means the median baryon fraction for such low-mass systems could be even smaller.

The baryon fraction is an important value needed to constrain cosmological simulations. One of the major challenges is tuning the strength of feedback to match the baryon distribution reported by observations. As shown in Figure 1.4, there is clear tension between different state-of-the-art cosmological simulations for the gas, stellar, and baryon fractions, most notably at low masses. This mostly stems from the different prescriptions of AGN feedback. It is difficult to constrain the governing parameters, largely because many baryons are still missing. In turn, it is imperative for observations to capture the hot and diffuse baryons that have been elusive for decades. In the next section, we introduce the Sunyaev-Zel'dovich (SZ) effect as another tool for solving the missing baryon problem.

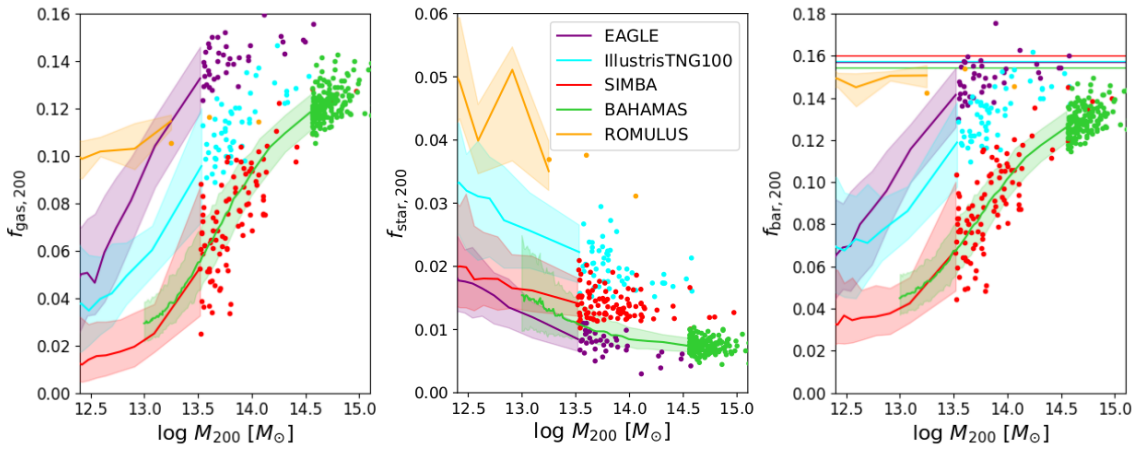


Figure 1.4 Plots of the gas, stellar, and baryon fractions taken from Figure 3 in Oppenheimer et al. (2021). The average values and scatter are shown for different simulations. There is clear tension between the results, especially at low masses. The main difference is caused by the different prescriptions of AGN feedback.

1.2 The Sunyaev–Zel'dovich (SZ) Effect

1.2.1 Inverse-Compton Scattering

The SZ effect was first derived by Zeldovich & Sunyaev (1969) when considering the inverse-Compton scattering between low-energy CMB photons and hot electrons. Overall, kinetic energy is transferred from the electrons and given to the photons. First, one can calculate the probability that a single scattering event will cause a given frequency shift to an incoming photon. Then the net energy transferred can be determined by averaging over the electron velocity distribution, assuming isotropic momenta of both the electrons and photons (Shimon & Rephaeli 2004, Rephaeli et al. 2006).

In the non-relativistic limit where $h\nu << k_b T_e$ and $T_e >> T_r$, the scattering process is simplified and given by the Kompaneetz equation

$$\frac{\partial n}{\partial y} = x^{-2}\frac{\partial}{\partial x}x^4\frac{\partial n}{\partial x} \tag{1.9}$$

where n is the occupation index of the photons, and $x = \frac{h\nu}{k_b T_r}$, and $T_r = T_{\rm CMB}$ is the radiation temperature equal to that of the CMB, and Zeldovich & Sunyaev (1969) famously introduced the variable

$$y = \int \frac{k_b T_e}{m_e c^2} n_e \sigma_T c dt \tag{1.10}$$

where m_e is the mass of an electron, c is the speed of light, σ_T is the Thompson cross-section,

and dt is the differential unit of time. The time integral above can be changed into a path length traveled by the photons, $\int cdt = \int dl$, and is customary to write this as

$$y = \int \frac{\sigma_T k_b T_e(l) n_e(l)}{m_e c^2} dl \tag{1.11}$$

and this is proportional to the thermal electron pressure, $P_e \propto n_e T_e$, along a line of sight.

Assuming the scattering causes small deviations to the Planck function, I_ν, one can approximate the change in the photon occupation index as a first-order power series (Fabbri et al. 1978). The change in occupation index leads to a change in the radiation intensity

$$\frac{\Delta n}{n_0} = \frac{\Delta I_\nu}{I_{\nu,0}} = y \left[\frac{x e^x}{e^x - 1} \left(\frac{x}{\tanh(x/2)} - 4 \right) \right] \tag{1.12}$$

where $n_0 = (e^x - 1)^{-1}$ and $I_{\nu,0}$ is the unperturbed intensity of the radiation (i.e., the CMB). The same equation can also be expressed in temperature units of the CMB such that

$$\frac{\Delta T}{T_{\rm CMB}} = y g(x) \tag{1.13}$$

where $g(x) = x\coth(x/2) - 4$ (Planck Collaboration et al. 2016b). This is an important result because $g(x)$ has a fixed spectral shape. Therefore, the observed quantity, $\frac{\Delta T}{T_{\rm CMB}}$, is directly related to sought after variable, y, which tells us about the total electron pressure along a line of sight.

1.2.2 Complementary Nature of X-rays and the SZ Effect

The SZ effect provides an independent probe of hot gas in ways that X-rays cannot. First, the SZ effect is notably independent of redshift. This is contrary to the X-ray surface brightness

$$b_X(\nu) = \frac{1}{4\pi(1+z)^3} \int n_e^2 \Lambda(\nu, T_e) dl \tag{1.14}$$

which quickly drops with increasing redshift (Birkinshaw 1999). This makes it very challenging to study the X-ray properties of hot halos beyond the local Universe. In turn, the SZ effect can be an effective probe of high-z gas.

Also, X-rays provide an emission-weighted measure in which the density and temperature are coupled. This degeneracy can be lifted using detectors that exists in modern-day X-ray observatories (Jansen et al. 2001, Weisskopf 2003). These measure the energies of the received photons, which can then be converted to an estimate of the gas temperature. Accurately determining the temperature, however, requires the capture of many photons. This demands

expensive observations which are oftentimes infeasible, especially for more distant and/or cooler objects. The density and temperature are also coupled for the SZ effect, however, tighter constraints can be placed on these quantities when using b_X and y in tandem. Or, vice versa, if one has constraints on the X-ray temperature, then it becomes much easier to determine the gas mass. Lastly, one can also exploit the redshift (in)dependence of both observables to get an estimate of the Hubble constant (Birkinshaw et al. 1991, Kozmanyan et al. 2019).

1.2.3 Noise Contamination in Observations

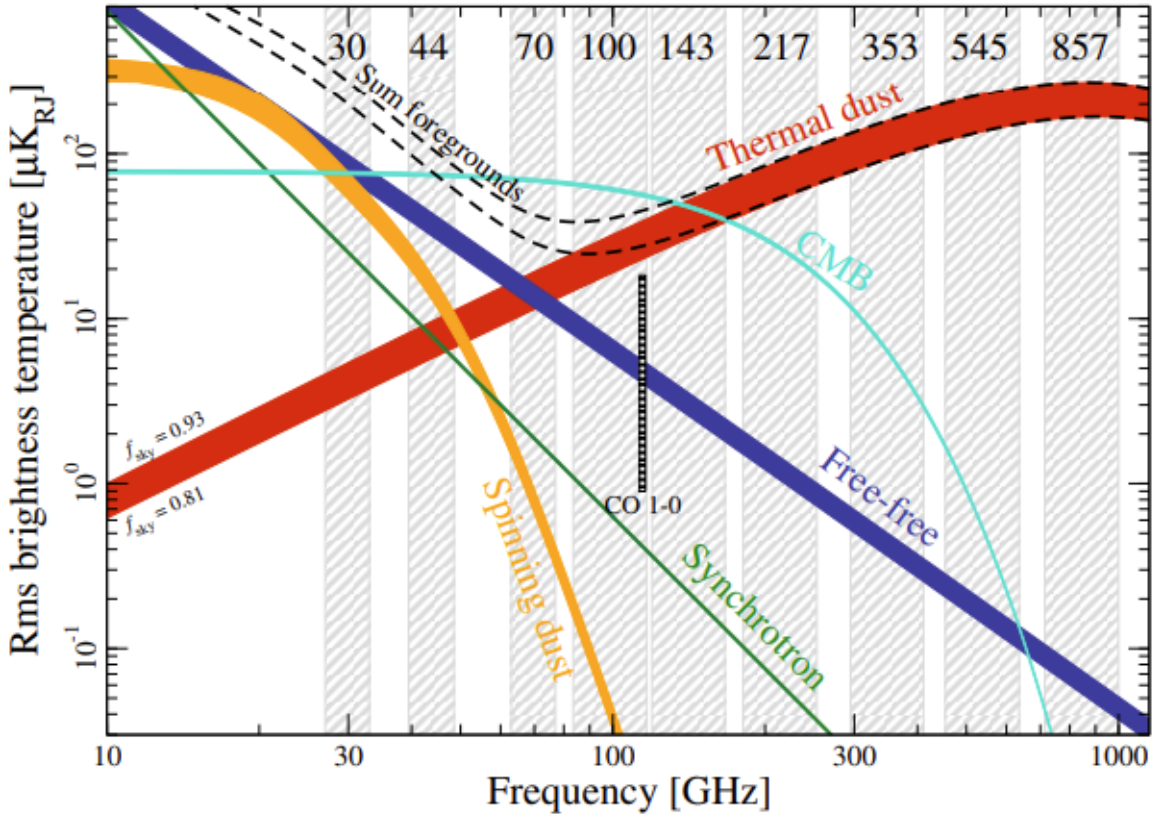


Figure 1.5 General contributions from different emissions near the CMB frequencies. Figure taken from Figure 4 in Planck Collaboration et al. (2020a).

The first observations of the SZ effect came from single-dish radio observatories yielding contentious results (Birkinshaw et al. 1991, Carlstrom et al. 2002). One of the main early complications was caused by instrumental temperature variations as well as other terrestrial noise (Carlstrom et al. 2002). With the advent of the *WMAP* and *Planck* observatories, such

issues have been mitigated. These space-based observatories also allowed for better spectral measurements by avoiding atmospheric absorption. Increasing the spectral coverage was revolutionary for SZ studies. While these data constitute the best data currently available for SZ studies, there are still systematic challenges that we must consider.

The SZ effect causes a differential signal in the CMB temperature that renders a decrement near radio frequencies ($\nu \lesssim 217$ GHz) and increments at higher frequencies. It is regarded as a weak distortion that causes relative temperature changes on the order of $\frac{\Delta T}{T} \lesssim 10^{-4}$ which is for the strongest signals coming from the most massive clusters of galaxies (Cavaliere et al. 1991). Detecting such a weak signal is especially challenging because it is embedded in a sea of other astrophysical emissions that are prominent at this part of the electromagnetic spectrum. These include sources within the Galaxy as well as beyond.

Shown in Figure 1.5 are the emission spectra, given in Rayleigh-Jeans temperature units of $\mu\mathrm{K_{RJ}}$, for some of the most notable foregrounds in the *Planck* bands. Thermal dust emission is the most significant contributor at frequencies $\nu > 143$ GHz. At lower frequencies, thermal dust emission takes a back seat to a number of other components including: free-free, spinning dust, synchrotron, and the CMB.

What is not shown in Figure 1.5 are the contributions from extragalactic sources. One example is the contribution from background AGNs. AGNs can produce strong radio signatures often seen as extended lobes carved out by biconical jets. Also, AGNs are typically fueled by galaxies with lots of dust and high star-formation rates. Stellar feedback heats the ambient dust in the disk and makes the galaxy a strong emitter in the IR. To make things even more complicated, galaxies exists over a range of redshifts, so there is a cosmological reddening of their spectra. This means that two galaxies with the same rest-frame emissions but at different redshifts will not look the same in our observations. All of these emissions must be taken into account when using *WMAP* and *Planck* data.

1.2.4 Component Separation

The SZ effect must be separated from the various astrophysical emissions described above. This is nearly impossible to do with single-band photometry since all of the components will be blended together. Therefore, it is crucial to have robust spectral coverage. The same is true for separating other components such as the CMB which was the main motivation for launching *WMAP* and *Planck*. Thanks to these missions, the extensive work on the CMB has paved the road for SZ studies.

Extracting the SZ (or CMB) signal has been attacked from many angles. One of the original, and most popular, approaches is the *internal linear combination* (ILC). It is a semi-

blind method that can be solved analytically using Lagrange multipliers (Delabrouille et al. 2009). This is an attractive solution because it is relatively straightforward to comprehend and makes very few assumptions. The two main assumptions are: (1) the spectral signature for the component of interest is known and (2) the signal is uncorrelated with all other components. The spectral functions are known for the SZ and CMB signals, however, the latter assumption is not always valid, and this can lead to systematic uncertainties.

Other methods have been proposed as well, but each of these come with their own assumptions and limitations. Another semi-blind extraction method, known as general morphological component analysis (GMCA; Bobin et al. 2008), was developed to extract the CMB and SZ signals. GMCA relies on the assumption of sparsity to separate signals using an iterative approach. In its simplest form, the assumption of sparsity is not enough to perform well in real-life scenarios, thus, adaptations to this algorithm have been made over time (e.g., Wagner-Carena et al. 2020, Bobin et al. 2015). Many other algorithms also exist, however, the search for improved component separation techniques is still in high demand.

1.3 This Thesis

The work presented in this dissertation is devoted to understanding the hot and diffuse gas around collapsed structures primarily through the SZ effect. The next two chapters (Chapter 2 and Chapter 3) investigate the observational signatures of galaxy groups and clusters using X-ray, optical, and SZ data. Then the last two chapters (Chapter 4 and Chapter 5) present experimental work on improving the quality of current SZ extractions by incorporating machine learning principles. The main ideas of the remaining chapters are as follows:

- Chapter 2 presents the scaling relations of X-ray detected galaxy groups and clusters near the North Ecliptic Pole. This includes the first time individual SZ measurements of galaxy groups were included in fitting scaling relations rather than stacking. This work is published in the Astrophysical Journal as Pratt & Bregman (2020, ApJ, 890, 156).

- Chapter 3 contains the work on measuring the first radial SZ profiles for nearby galaxy groups. This work is published in the Astrophysical Journal as Pratt, Qu, and Bregman (2021, ApJ, 920, 104).

- Chapter 4 shows our first attempt at improving the quality of SZ data by creating a hybrid between analytical and machine learning methods known as Deep-NILC. This

work is published in the Astrophysical Journal as Pratt, Qu, and Bregman (2024, ApJ, 964, 122).

- Chapter 5 presents a full machine learning approach for extracting the SZ signal. This work was submitted to the Astrophysical Journal shortly after this dissertation.
- Chapter 6 provides a summary and discusses the future work that could be done.

CHAPTER 2

SZ Scaling Relations of Galaxy Groups and Clusters Near the North Ecliptic Pole

2.1 Abstract

SZ scaling relations have been used to test the self-similar prediction for massive galaxy clusters, but little attention has been given to individual galaxy groups. We investigate the scaling relations of galaxy groups and clusters near the North Ecliptic Pole using X-ray and SZ observations. This region of the sky is where both the *ROSAT* and *Planck* satellites achieved their deepest observations, permitting the investigation of lower mass systems. Our sample consists of 62 X-ray detected groups and clusters, spanning a mass range of $10^{13.4} M_{\odot} < \ M_{500} < 10^{15} M_{\odot}$ and redshifts of $0.03 \lesssim z \lesssim 0.82$. We extract the total SZ flux from unresolved *Planck* data and estimate the fraction of the SZ flux within R_{500} assuming two different pressure profiles. The SZ scaling relations were derived using a Bayesian technique that accounts for censored data. We find a power law slope of $1.73^{+0.19}_{-0.18}$ for the $Y_{SZ} - M_{500}$ relation which is consistent with the self-similar prediction of 5/3. The slope of $0.89^{+0.09}_{-0.08}$ for the $Y_{SZ} - L_{X,500}$ relation is in agreement with other observational studies but not the self-similar prediction of 5/4, and the $Y_{SZ} - Y_X$ relation lies below the 1:1 relation when the slope is fixed to unity. The determined scaling relations are dependent on the selected pressure profile, so resolved data are needed to determine the effects of AGN feedback. In addition, we find a number of potential cluster candidates in the *Planck* Compton maps that were not identified in our X-ray sample.

2.2 Introduction

In the hierarchical growth model, low-mass galaxy groups agglomerate at high redshifts to form today's massive galaxy clusters with dark halo masses $\gtrsim 10^{14} M_{\odot}$ (for a review on

cluster formation see Kravtsov & Borgani 2012). Although galaxy clusters are comprised of galaxy groups, their properties are very different, including: gas fractions, star formation efficiencies, and X-ray morphologies (Mulchaey 2000, Dai et al. 2010, Behroozi et al. 2013, McCarthy et al. 2017). It is believed the total enclosed mass dictates these different qualities, meaning, there may be some characteristic mass where these systems become distinct (Paul et al. 2017). However, groups and clusters exhibit a spectrum of masses so the boundary is somewhat vague.

Groups and clusters host large reservoirs of hot baryons surrounding their member galaxies. These gaseous halos, known as the intracluster medium (ICM), account for the majority of baryons in these systems (Andreon 2010, Dai et al. 2010, Kravtsov & Borgani 2012). (The ICM is referred to as the hot gaseous halo, regardless if the system is a group or a cluster.) The ICM is formed through the gravitational collapse of the intergalactic medium, during which gas is compressed and heated until it reaches hydrostatic equilibrium. Gravitational heating is a scale-free mechanism that only depends on the total enclosed mass. If gravitational collapse were the dominant processes in forming the ICM then it should scale self-similarly (Kaiser 1986). In reality, the ICM is constantly being affected by non-gravitational mechanisms such as accretion shocks and AGN feedback (Bhattacharya et al. 2008, Fabian 2012, Lau et al. 2015).

The halos of galaxy groups are more susceptible to the effects of non-gravitational processes compared to their higher mass counterparts for a few reasons. First, groups reside in smaller potential wells, meaning non-gravitational processes may contribute a significant portion of the thermal energy compared to gravitational heating alone. Second, feedback from galactic winds and active galactic nuclei (AGNs) can create an entropy floor in groups by injecting high entropy gas and removing low entropy gas. This prevents ambient gas from accreting and, therefore, reduces the gas fraction (Pratt et al. 2009, McCarthy et al. 2011, Le Brun et al. 2017, Truong et al. 2018). Galaxy clusters, on the other hand, behave as "closed-box" systems and re-accrete any ejected material (Farahi et al. 2018). Third, galaxy groups are thought to exist in a wide range of virialization states (Mulchaey 2000, Balogh et al. 2011) while most clusters have had enough time to relax. Lastly, groups are much more likely to experience mergers that cause morphological disruption. In the case of a dynamically young system, the assumptions of hydrostatic equilibrium and spherical symmetry become invalid, making it a challenge to characterize the ICM. Mergers can also produce shocks that heat the ICM.

Many efforts have been made in the X-rays to search for the differences between the halos of groups and clusters (see Giodini et al. 2013 for a review on cluster scaling relations). Simulations indicate there should be a change in the scaling relations when moving from

groups to clusters. The predicted changes are those in the slopes and scatter at different mass scales, which are attributed to the differences in gas fractions and ranges of dynamical states (Davé et al. 2002, Le Brun et al. 2017, Paul et al. 2017, Farahi et al. 2018). Some observational studies claim to have found such evidence at low masses. For example, Eckmiller et al. (2011) reported increases in scatter and Lovisari et al. (2015) found changes in their slopes towards the group regime. On the other hand, massive clusters appear self-similar once their central cores ($R \lesssim 0.15\ R_{500}$) have been excised (Pratt et al. 2009, Mantz et al. 2016).

In addition to X-rays, recent studies have used the Sunyaev–Zel'dovich (SZ) effect to characterize the halos of groups and clusters. The SZ effect is the energy boost given to cosmic microwave background photons via inverse Compton scattering and is quantified via the Compton parameter

$$y = \frac{\sigma_T}{m_e c^2} \int_0^\infty P_e(r) dl \tag{2.1}$$

where σ_T is the Thompson cross section, m_e is the mass of an electron, c is the speed of light, $P_e(r)$ is the pressure of electrons as a function of radius where $P_e(r) = k_B n_e(r) T_e(r)$, k_B is the Boltzmann constant, and dl is integrated along a line-of-sight. Its linear dependence on density provides a mass-weighted measure, making it sensitive to the outskirts of the ICM. X-ray emission depends on the square of the electron density, yielding an emission-weighted measure, which is dominated by clumps and the central cores.

Recent SZ studies have confirmed that clusters are consistent with the self-similar prediction (Bonamente et al. 2008, Andersson et al. 2011, Marrone et al. 2012, Planck Collaboration et al. 2014a). Current sensitivities of the SZ signal, however, have permitted studies of only the most massive systems ($\gtrsim 10^{14} M_\odot$). This paper is among the first studies to investigate the SZ scaling relations using lower mass systems. We use a sample of groups and clusters detected near the north ecliptic pole (NEP) where the *ROSAT* and *Planck* satellites obtained their deepest observations. The rest of the paper is structured in the following way: section 2.3 describes the NEP sample, section 2.4 explains the methods used to extract the SZ signal, section 2.5 presents the results, section 2.6 provides an analysis of our results and a discussion of future work, and section 2.7 gives a brief summary and highlights the main conclusions of the study.

Throughout this paper we use the following cosmological parameters: $\mathrm{H_0} = 70\ \mathrm{km\ s^{-1}\ Mpc^{-1}}$, $\Omega_\mathrm{M} = 0.3$, $\Omega_\Lambda = 0.7$, and $\mathrm{E(z)} = \sqrt{\Omega_\Lambda + \Omega_\mathrm{M}(1+\mathrm{z})^3}$. We discuss regions where the enclosed mass density within a sphere is some factor, Δ, above the critical density, ρ_c, such that $M_\Delta = \frac{4\pi}{3} \Delta \rho_c R_\Delta^3$.

2.3 NEP Sample

The NEP has been a very popular region of the sky to perform deep, contiguous surveys. In particular, the scanning pattern of the *ROSAT* satellite yielded its longest exposures near the ecliptic poles. The region $17^{\rm h}15^{\rm m} < \alpha_{2000} < 18^{\rm h}45^{\rm m}$ and $62^\circ < \delta_{2000} < 71^\circ$ was investigated by Henry et al. (2006) and these authors provided a flux-limited sample of sources above $\sim$ 2 x 10^{-14} erg cm^{-2} s^{-1} in the 0.5–2.0 keV band. Of the 442 sources in their catalog, 63 galaxy clusters were identified, however, two of the clusters appear to be part of a single system (RX J1724.2+6956 and RX J1724.1+7000) and has been noted by these authors. (Their redshifts and temperatures are identical, and they are only separated by $\sim 4'$ or [0.18 Mpc]. In this study, the properties of the brighter detection were used.) For galaxy groups and clusters, they provided useful quantities including: unabsorbed flux measurements in the 0.5–2.0 keV band, the X-ray luminosities within R_{200} also measured in the 0.5–2.0 keV band, X-ray temperatures estimated from the low-redshift luminosity-temperature relation (White et al. 1997), and redshifts from their optical identification program (Gioia et al. 2003). The sources in this catalog stem from high-quality X-ray data. Henry et al. (2006) required the detect count rate SNR>4 for each source such that they contained a sufficient collection of photons; the median number of counts was 91 and the minimum was 28.

The *Planck* satellite also rendered its deepest observations near the ecliptic poles (Planck Collaboration et al. 2011a; 2014b; 2016b). The four year mission scanned the sky using seven frequency channels, spanning 30-857 GHz. These data were then used to construct Compton maps (y-maps) by Planck Collaboration et al. (2016b). The various frequency maps were combined using two linear combination methods: the Needlet Independent Linear Combination (NILC) and the Modified Internal Linear Combination Algorithm (MILCA). These algorithms aimed to minimize the variance of the reconstructed maps while preserving the SZ signal.

The NILC maps used combined data both from the high and low frequency instruments (HFI and LFI) to capture contamination at various scales, but the MILCA maps only uses data from the HFI. In both cases, the HFI maps were smoothed to a common resolution of $10'$. We believe the maps produced by the NILC do a better job at removing contaminating radio sources (described below) and exhibit lower residuals compared to the MILCA maps. We extracted the SZ flux from both maps and found that their values agreed within the statistical uncertainties. In this study, we used the NILC maps to determine the scaling relations.

2.4 Extraction of the SZ Signal

2.4.1 Sources of Contamination

The y-maps suffer from various sources of galactic and extragalactic contamination. Galactic thermal dust emission is the main source of contamination at large angular scales while the Cosmic Infrared Background (CIB), radio sources, and infrared sources dominate at small angular scales (Planck Collaboration et al. 2016b). Radio sources appear as negative peaks while infrared sources are positive. Many of these point sources were identified and cataloged by Planck Collaboration et al. (2014c). These can be accounted for in the y-maps by applying the point source mask provided by Planck Collaboration et al. (2016b). The point source mask removed most the contamination, but some of the polluting signal still leaked into the background. In addition, it was confirmed that many strong radio sources were not removed by the mask after searching the 20-cm catalog (White & Becker 1992). In order to better account for contamination, we decided to identify and remove radio sources manually.

The manual removal of radio sources was an effective method for the most conspicuous sources, but a population of more modest radio sources still remained unaccounted for. To understand the impact of these weaker sources, we searched the 20-cm radio catalog in a 12° x 12° field centered around the NEP (we call this the NEP grid herein). The catalog indicated that 50 sources were not identified by our manual inspection. We then tested to see if these objects produced a non-trivial amount of contamination. Their signals were extracted by taking the average value inside a circle centered on the source with a $20'$ radius. The signal from each source was then compared to its immediate background which was defined as an annulus with a radius $60'$ after excluding the inner circle.

The differences between the radio sources and their backgrounds in units of standard error (see subsection 2.4.2) are shown in Figure 2.1. Radio sources should appear negative relative to their backgrounds in the y-maps i.e., on the left side of Figure 2.1. Half of the sources yielded a positive signal relative to their backgrounds, and the mean of the distribution was -0.18σ. We did not find strong enough statistical evidence, according to the two-sided t-test and the Wilcoxon signed-rank test, to reject the null hypothesis that the mean was consistent with zero. It was concluded that these modest radio sources did not have a significant effect in our ability to extract the SZ flux. The same result was obtained after combining the point source mask with our manual exclusion mask. Overall, there was no substantial improvement when implementing the point source mask, so it has not been included in this study.

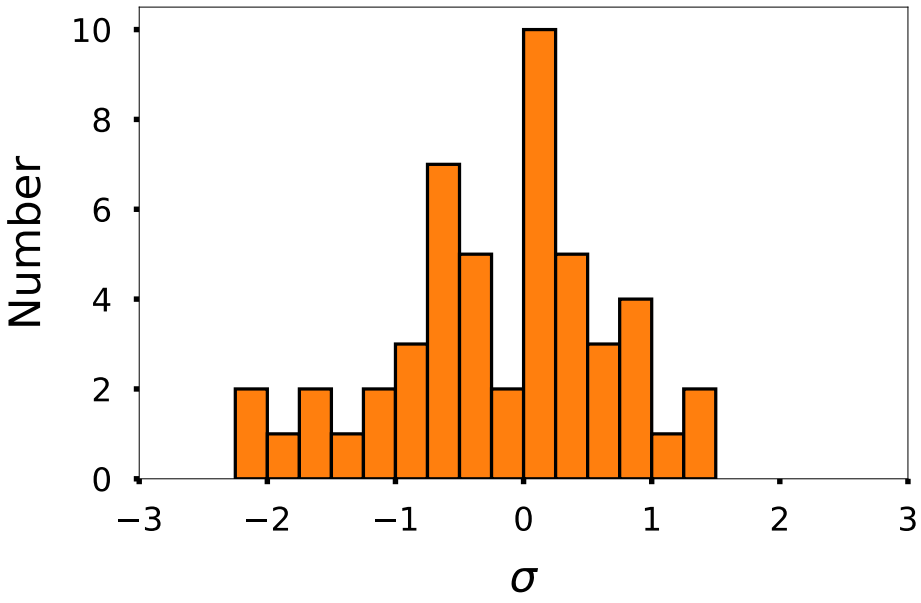


Figure 2.1 Histogram displaying the amount of contamination stemming from radio sources that were not identified in our manual removal program (see text). The p-values from the two-sided Student's t-test and the Wilcoxon signed-rank test were 0.13 and 0.10 respectively. These are the probabilities of measuring a mean of zero purely by chance.

2.4.2 Uncertainties

There were two sources of error considered in this study: instrumental noise and the stochastic background. The stochastic background was determined empirically, and the instrumental noise was characterized using the half difference maps released by Planck Collaboration et al. (2016b).

The stochastic background was quantified by the standard deviation in the Compton parameter, σ_y, as function of area. We created 360 sets of random annuli across the NEP grid where each annulus consisted of 18 bins separated by $10'$. The five outermost bins determined the average local background which were then subtracted from the inner bins. The inner bins were used to quantify the background fluctuations by taking the average values from alike bins to estimate σ as a function of area. For example, the uncertainty in a $10'$ circle was estimated by using the average values of the innermost bins across all sets of annuli.

We point out that not all annuli were used in the analysis because many regions were obstructed by contaminating sources. There were many cases where most or all of the pixels within an annulus were unavailable due to nearby contaminants. In order to obtain robust estimates of the uncertainty, bins were required to retain $\geq 50\%$ of their pixels. We modeled

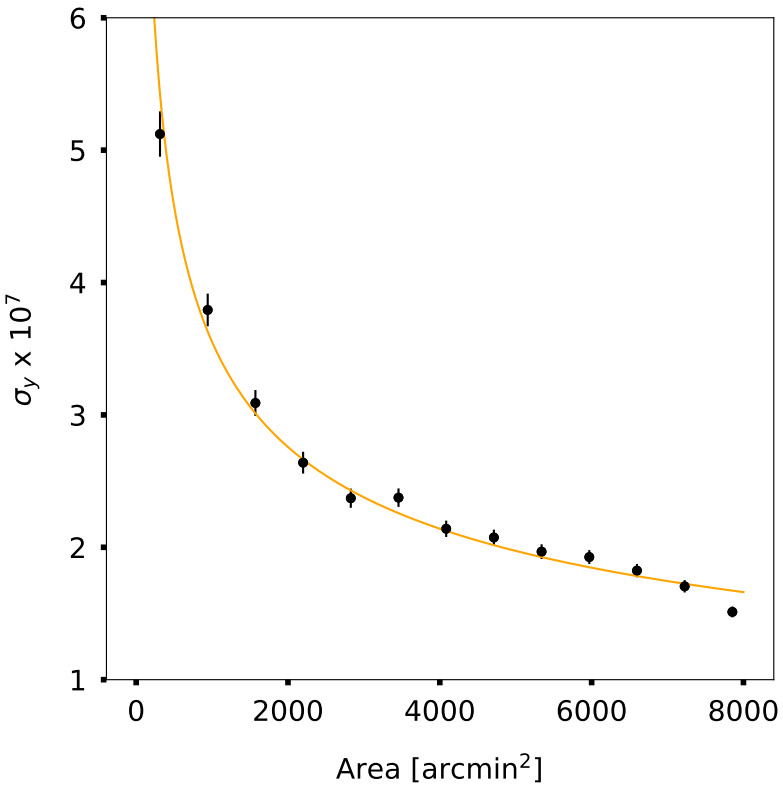


Figure 2.2 Best fit power law used to estimate the standard deviation in the Compton parameter as a function of area.

σ_y with a power law. We expected σ_y to scale as the inverse square root of the area, however, our results yielded a shallower slope of -0.372 (-0.382) for the NILC (MILCA) maps. We show the power law fit for the NILC maps in Figure 2.2. This flattened profile suggests there are large-scale secular variations in the y-maps.

Instrumental noise was characterized using the half difference maps provided by Planck Collaboration et al. (2016b). In these maps, the astrophysical emission has been eliminated, leaving only the instrumental component. The mean instrumental error was determined following a similar procedure for the stochastic background. The stochastic component was found to be $\sim 30\times$ larger than the instrumental component.

2.4.3 Unresolved Sources

For a typical cluster, most of the pressure of the ICM is found within R_{500} (Arnaud et al. 2010). We estimated R_{500} for all of our systems using the $M_{500} - T_X$ relation for low mass clusters of galaxies from Kettula et al. (2015). On the y-maps, the projected radius is given by $\theta_{500} = \frac{R_{500}}{D_A}$ where D_A is the angular distance. An object will be mostly unresolved if θ_{500}

is less than the resolution of the y-maps ($10'$). In our sample, only 13% (8/62) of our objects have $\theta_{500} \geq 10^{'}$ while all of them have $\theta_{500} < 21'$.

Since we could not completely resolve the SZ signals of our objects, we needed to understand the behavior of a point source and characterize the point spread function (PSF) of the y-maps. A sample of 27 bright point sources in the y-maps were used to determine the profile of the PSF. These were selected using the second Planck catalog of SZ sources (Planck Collaboration et al. 2016a) in conjunction with the meta-catalog of X-ray detected clusters of galaxies (Piffaretti et al. 2011). The clusters were selected using the following criteria: (1) $\theta_{500} < 5'$ to ensure they were unresolved (2) they were detected with high SNRs (> 10) as quoted by Planck Collaboration et al. (2016a) (2) the centroids of the X-ray emission and SZ signal agreed within $5'$ (4) the clusters did not appear to be involved in any obvious mergers.

The PSF was modeled using a power law with a projected core radius of $\theta_c = 10'$. The profile takes the form

$$y_{psf}(\theta) = S_0\Big[1 + \Big(\frac{\theta}{\theta_c}\Big)^2\Big]^{\frac{-3\beta}{2}+\frac{1}{2}} + S_1 \tag{2.2}$$

where S_0 is the normalization, S_1 corrects for the local background, and β characterizes the slope of the decay. β was estimated using the profiles given the sample of known point sources. The point sources were sampled using 18 annuli in $10'$ bins. Most of the signal was captured within the first 2–3 bins while the remaining bins determined the local background offset. We then determined the values of β that minimized χ^2 for each object. Our results yielded a mean slope of 2.39 ± 0.15 and a median of 2.29 using the NILC map; the mean β was 2.48 ± 0.15 and the median equal to 2.38 for the MILCA maps. The mean β values were consistent between the two maps and also consistent with their medians. Using the median β to characterize the PSF, we then calculated the FWHM. Our PSF model yielded in a FWHM of $10.3'$ ($10.1'$) for the NILC (MILCA) maps. This is similar to the FWHM of $10'$ used to smooth y-maps.

Some of sources were semi-resolved (i.e., $\theta_{500} > 10^{'}$), so we modelled our data by convolving the PSF with the universal pressure profile (UPP) from Arnaud et al. (2010) giving the functional form of the measured Compton parameter

$$\tilde{y}(\theta) = y_{psf}(\theta) \circledast y_{upp}(\theta) \tag{2.3}$$

Assuming spherical symmetry, the total SZ flux, Y_{SZ}, in arcmin^2 is

$$Y_{SZ} = \int_0^\infty 2\pi\tilde{y}(\theta)\theta d\theta \tag{2.4}$$

The total flux can then be converted into the portion within a spherical region of radius

R_{500}, but the unresolved nature of our objects required making assumptions about the pressure profiles. We considered two different pressure profiles to compute the fraction of the total SZ flux within R_{500}. The first method was to apply the UPP to all objects, which yields a constant fraction of ≈ 0.535, which was found by integrating the UPP to R_{500} and to infinity. The second method was to apply the mass- and redshift-dependent pressure profiles provided by Battaglia et al. (2010) (BPP herein), which takes into account the effects of AGN feedback. We denote the SZ flux within R_{500} as $Y_{sph,500}$ and the SZ luminosity as $Y_{sph,500}D_A^2$.

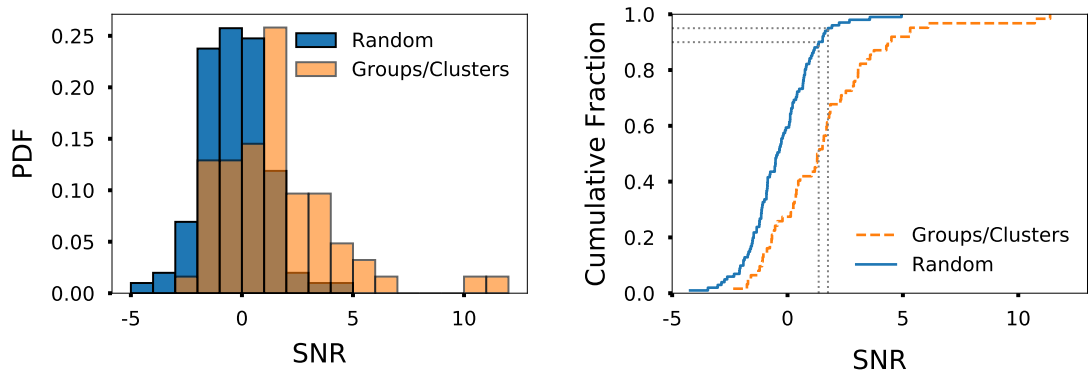
2.4.4 Detections vs. Nondetections

The sensitivity limit of the y-maps precluded us from extracting an acceptable SZ flux for every object. Interloping radio sources can wash out an SZ signal, and the background noise imposes an effective flux limit, rendering some of our sources as nondetections. In order to separate detections from nondetections, we investigated the set of random annuli in the NEP grid after removing sources of contamination. The annular bins were required to retain $\geq 50\%$ of their area in order to work with a robust sample. This was especially important for the innermost annuli ($\leq 30'$) as they captured most of the flux from a point source. These data were then fit with the PSF model which we used to calculate signal-to-noise ratios (SNRs) for each random region. We calculated the SNR as

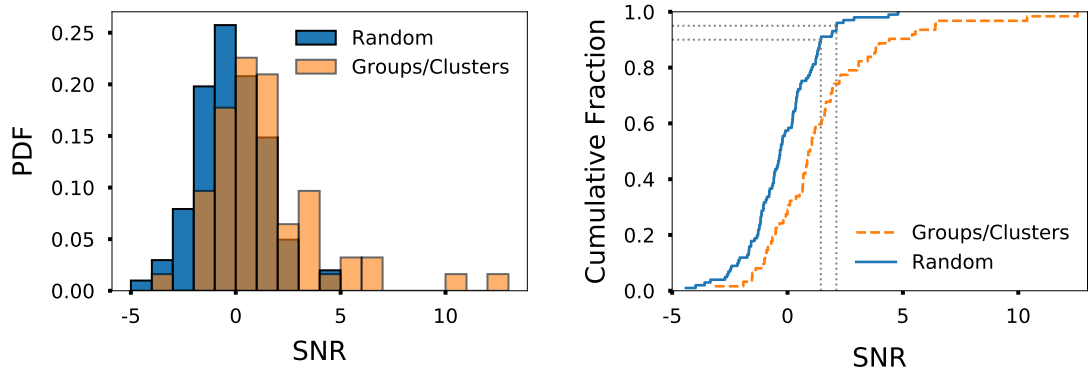
$$SNR = S_0/\sigma_{S_0} \tag{2.5}$$

where S_0 is the normalization from Equation 2.2 and σ_{S_0} is the uncertainty on its estimated value. The same procedure was done for all of the known groups and clusters but with no restrictions placed upon the number of available pixels. Histograms and cumulative fractions of the SNR distributions are provided in Figure 2.3.

There are a few important points one can draw from Figure 2.3. First, the SNR distributions did not stem from the same parent population and were statistically distinct according to the Anderson-Darling test (p-value $< 10^{-5}$). It also indicates where the background cumulative fractions reached 90% and 95%. The 90% and 95% limits occurred at SNR values of 1.35 (1.44) and 1.75 (2.12) respectively in the NILC (MILCA) maps. These SNR values were considered as arbitrary thresholds where one could confidently detect a real SZ signal instead of a random fluctuation. We adopted the 90% threshold (SNR = 1.35) for this study, yielding 32 detections and 30 nondetections.



(a) NILC



(b) MILCA

Figure 2.3 SNR distributions for 62 groups/clusters and 101 random regions near the NEP. Included are normalized histograms (probability distribution functions [PDFs]) and cumulative fractions. The top figures are the distributions in the NILC maps and the bottom are those from the MILCA maps. The vertical and horizontal dashed lines in the right panels indicate where the cumulative fractions of SNRs for the random regions reach 90% and 95%.

2.5 Scaling Relations

2.5.1 X-ray Properties

The X-ray data used in this study came from the NEP catalog constructed by Henry et al. (2006). These authors measured photons count rates which were then converted into unabsorbed fluxes and luminosities within R_{200}. In order to stay consistent with our choice of R_{500} , we transformed the luminosity values to that inside R_{500} , denoted as $L_{X,500}$. This was

done by taking the fraction of the emission measure inside R_{500} compared to that inside R_{200} using an isothermal β model for the electron density distribution

$$n_e(r) = n_{e,0}\Big[1 + \Big(\frac{r}{r_c}\Big)^2\Big]^{\frac{-3\beta}{2}} \tag{2.6}$$

assuming $\beta = 2/3$, $r_c = 0.15\ R_{500}$, and $R_{500} = 0.7\ R_{200}$. This is simply a ratio of integrating n_e^2 over the two volumes, yielding a fraction ≈ 0.938 for all objects.

We also computed the X-ray analog of the SZ luminosity within R_{500} , denoted as $Y_{X,500}$, which is defined as the product of the gas mass and the temperature (Kravtsov et al. 2006). We estimated the gas mass using the APEC model simulation of a ROSAT PSPC spectrum. The model was provided a temperature, abundance (assumed to be 0.3 Solar), redshift, and exposure time. In return, the model predicts an energy flux, F_{APEC}, which was then compared to the observed fluxes of our objects, F_{obs}. The ratio of these two fluxes were set equal to the normalization of the APEC model such that

$$\frac{F_{obs}}{F_{APEC}} = \frac{10^{-14}}{4\pi[D_A(1+z)]^2}\int n_e n_H dV \tag{2.7}$$

where D_A is measured in cm and $n_{e,H}$ is in cm^{-3}. We again assumed an isothermal β model for the density distribution. We adopted the values used by Andersson et al. (2011) for the mass density $\rho_{gas} = m_p n_p \mathrm{A}$ where the average nuclear mass was A = 1.397 and $n_e = 1.199 n_H$. In order to compare $Y_{X,500}$ with $Y_{sph,500}$ there was a factor $\sigma_T/m_e c^2 \mu_e m_p = 1.395 \times 10^{-19} \frac{\mathrm{Mpc}^2}{\mathrm{M}_\odot \mathrm{keV}}$ to convert $Y_{X,500}$ into units of Mpc^2. Values of $Y_{X,500}$ are provided in Table 2.1.

2.5.2 Regression Methods

Scaling relations are best modeled using linear regression in log-log space since the distributions are skewed in linear space. We fit our data using the functional form $\log_{10}(Y/Y_0) = \alpha + \beta \log_{10}(X/X_0)$ where Y_0 and X_0 are pivot points. The pivot points for M_{500}, $Y_{sph,500}D_A^2$, $Y_{X,500}$, and L_X, were $10^{14}\ M_\odot$, 10^{-5} Mpc^2, 10^{-5} Mpc^2, and $10^{43}\mathrm{erg\ s}^{-1}$ respectively.

The uncertainty in some variable X was approximated in log space as $\sigma_{log,X_i} = log_{10}(e)\sigma_{X_i}/X_i$ where σ_{X_i} is the measured uncertainty on X_i in linear space; this is a common practice in the literature (e.g., Bonamente et al. 2008, Eckmiller et al. 2011, Lovisari et al. 2015). The error bars were slightly asymmetric in M_{500} given the uncertainty and scatter in the $\mathrm{M}_{500} - T_X$ relation from Kettula et al. (2015). These errors were approximated as symmetric using the mean error. The error bars on $\mathrm{L}_{X,500}$ were scaled from the photon count

rate provided by Henry et al. (2006). The uncertainties on $Y_{X,500}$ were dominated by the 64% intrinsic scatter adopted from the results of the $Y_X - L_X$ relation determined by Lovisari et al. (2015).

ID	α (J2000)	δ (J2000)	z	$L_{X,500}$ [10^{42} erg s^{-1}]	T [keV]	M_{500} [10^{14} $M_\odot$]	$Y_{X,500}$ [10^{-6} Mpc^2]	SNR	Y_{SZ} [10^{-4} arcmin^2]
RX J1716.6+6410	17:16:39.7	64:10:35	0.2507	43.1 ± 6.6	3.7	3.13	10.02 ± 2.43	4.63	11.21 ± 2.42
RX J1721.4+6733	17:21:24.6	67:33:14	0.0861	1.87 ± 0.38	1.3	0.70	0.36 ± 0.09	-0.59	-0.67 ± 1.15
RX J1724.2+6956	17:24:16.0	69:56:44	0.0386	0.861 ± 0.2	0.9	0.41	0.11 ± 0.03	0.39	0.47 ± 1.20
RX J1724.7+6716	17:24:47.3	67:16:09	0.2540	15 ± 3.4	2.6	1.83	3.14 ± 0.81	1.82	2.39 ± 1.31
RX J1727.4+7035	17:27:25.8	70:35:37	0.3059	110 ± 14	5.5	5.54	31.39 ± 7.52	3.17	7.44 ± 2.34
RX J1728.6+7041	17:28:39.5	70:41:05	0.5509	227 ± 41	7.3	7.39	60.72 ± 15.03	3.24	9.68 ± 2.99
RX J1735.0+6405	17:35:04.9	64:05:57	0.1411	44 ± 3.6	3.7	3.32	11.08 ± 2.59	1.19	2.99 ± 2.52
RX J1736.3+6802	17:36:23.4	68:02:06	0.0258	2.81 ± 0.21	1.4	0.80	0.50 ± 0.12	3.60	12.10 ± 3.36
RX J1742.7+6735	17:42:46.8	67:35:53	0.0420	2.81 ± 0.28	1.3	0.71	0.39 ± 0.09	3.57	10.35 ± 2.90
RX J1743.3+6440	17:43:23.3	64:40:18	0.1790	27.1 ± 3.1	3.2	2.61	6.48 ± 1.54	3.02	5.75 ± 1.91
RX J1743.4+6341	17:43:28.1	63:41:39	0.3270	125 ± 11	5.7	5.78	34.98 ± 8.22	4.30	9.21 ± 2.14
RX J1745.2+6556	17:45:16.2	65:56:17	0.6080	74.9 ± 16	4.5	3.43	13.79 ± 3.51	-2.36	-3.60 ± 1.53
RX J1746.7+6639	17:46:45.0	66:39:20	0.3864	33.7 ± 7	3.4	2.55	6.82 ± 1.72	0.23	0.33 ± 1.40
RX J1747.5+6343	17:47:33.6	63:43:55	0.3280	40.3 ± 7.9	3.6	2.88	8.67 ± 2.17	3.72	7.75 ± 2.08
RX J1748.6+7020	17:48:41.6	70:20:31	0.3450	40.3 ± 7.7	3.6	2.85	8.60 ± 2.14	-1.24	-5.11 ± 4.11
RX J1749.0+7014	17:49:03.5	70:14:42	0.5790	215 ± 29	7.1	6.97	54.88 ± 13.19	-0.82	-6.15 ± 7.50
RX J1749.8+6823	17:49:49.8	68:23:15	0.0508	0.955 ± 0.16	1.0	0.47	0.14 ± 0.03	1.93	4.24 ± 2.20
RX J1751.2+6533	17:51:15.5	65:33:33	0.0424	0.674 ± 0.11	0.9	0.41	0.09 ± 0.02	1.45	3.27 ± 2.26
RX J1751.5+7013	17:51:30.7	70:13:32	0.4925	83.3 ± 16	4.9	4.18	18.82 ± 4.70	-1.13	-3.76 ± 3.33
RX J1751.5+6719	17:51:30.9	67:19:20	0.0933	3.74 ± 0.4	1.6	0.95	0.73 ± 0.17	5.59	7.95 ± 1.42
RX J1752.2+6522	17:52:12.0	65:22:22	0.3923	26.2 ± 5.2	3.0	2.10	4.78 ± 1.20	0.55	0.71 ± 1.30
RX J1754.5+6904	17:54:35.0	69:04:58	0.5113	53.4 ± 11	4.0	3.03	10.28 ± 2.61	2.33	7.41 ± 3.18
RX J1754.6+6803	17:54:41.9	68:03:33	0.0770	34.6 ± 0.98	3.4	3.01	8.86 ± 2.04	15.44	40.92 ± 2.65

RX J1754.7+6623	17:54:45.7	66:23:53	0.0879	2.81 ± 0.19	1.5	0.86	0.60 ± 0.14	-1.68	-4.01 ± 2.38
RX J1754.0+6452	17:54:05.3	64:52:01	0.2460	11.2 ± 2.3	2.4	1.62	2.43 ± 0.61	1.71	4.03 ± 2.35
RX J1755.3+6504	17:55:19.9	65:04:55	0.0846	1.87 ± 0.27	1.2	0.62	0.28 ± 0.07	0.38	0.92 ± 2.41
RX J1755.7+6752	17:55:45.5	67:52:42	0.0833	13.1 ± 0.7	2.5	1.88	3.17 ± 0.73	6.33	17.92 ± 2.83
RX J1755.8+6236	17:55:48.3	62:36:41	0.0270	3.74 ± 0.24	1.5	0.89	0.64 ± 0.15	1.94	8.71 ± 4.48
RX J1755.9+6314	17:55:56.5	63:14:03	0.3850	63.7 ± 9.5	4.2	3.52	13.67 ± 3.31	1.54	3.62 ± 2.36
RX J1756.5+6513	17:56:31.0	65:13:01	0.0284	0.571 ± 0.068	0.8	0.34	0.07 ± 0.02	-1.02	-2.23 ± 2.18
RX J1757.3+6631	17:57:19.8	66:31:39	0.6909	56.2 ± 7.2	4.1	2.83	9.38 ± 2.24	-0.44	-1.20 ± 2.72
RX J1758.9+6520	17:58:57.6	65:20:58	0.3652	15.9 ± 3.2	2.6	1.72	2.93 ± 0.73	-0.59	-1.14 ± 1.92
RX J1759.2+6902	17:59:17.5	69:02:20	0.0994	2.81 ± 0.47	1.5	0.86	0.57 ± 0.14	3.71	8.80 ± 2.37
RX J1800.4+6913	18:00:28.2	69:13:22	0.0821	14 ± 0.85	2.6	2.00	3.51 ± 0.82	0.40	1.06 ± 2.63
RX J1811.3+6447	18:11:19.1	64:47:36	0.4510	71.1 ± 12	4.4	3.63	14.88 ± 3.63	-1.06	-3.10 ± 2.94
RX J1812.1+6353	18:12:08.4	63:53:35	0.5408	132 ± 21	5.9	5.38	31.94 ± 7.79	0.25	0.57 ± 2.26
RX J1813.1+6230	18:13:11.5	62:30:33	0.1829	12.2 ± 2.8	2.5	1.79	2.83 ± 0.73	1.42	2.16 ± 1.53
RX J1814.2+6939	18:14:14.4	69:39:33	0.0874	13.1 ± 1.1	2.5	1.88	3.17 ± 0.74	2.44	3.99 ± 1.63
RX J1816.5+6911	18:16:32.4	69:11:34	0.2097	13.1 ± 2.7	2.5	1.76	2.89 ± 0.73	1.22	2.18 ± 1.78
RX J1817.7+6824	18:17:46.1	68:24:24	0.2820	137 ± 9	5.9	6.25	40.68 ± 9.46	1.46	3.17 ± 2.17
RX J1817.1+7024	18:17:08.4	70:24:13	0.0859	3.74 ± 0.73	1.5	0.86	0.61 ± 0.15	0.26	0.55 ± 2.13
RX J1819.0+6909	18:19:04.1	69:09:24	0.0880	3.74 ± 0.73	1.6	0.95	0.72 ± 0.18	1.32	3.45 ± 2.62
RX J1819.8+6748	18:19:48.8	67:48:48	0.2153	14 ± 2.9	2.6	1.87	3.17 ± 0.80	0.98	1.10 ± 1.13
RX J1802.9+6339	18:02:54.0	63:39:10	0.0907	1.22 ± 0.29	1.1	0.54	0.19 ± 0.05	-0.73	-1.75 ± 2.37
RX J1820.2+6857	18:20:13.0	68:57:22	0.0890	25.3 ± 1.5	3.0	2.47	5.99 ± 1.39	1.64	4.03 ± 2.45
RX J1821.6+6827	18:21:38.1	68:27:52	0.8156	198 ± 43	6.9	5.79	40.36 ± 10.29	1.57	3.48 ± 2.22
RX J1822.6+6641	18:22:37.4	66:41:29	0.0888	2.81 ± 0.46	1.4	0.78	0.45 ± 0.11	-1.91	-3.56 ± 1.86
RX J1829.0+6913	18:29:03.7	69:13:50	0.2057	88.9 ± 7.7	5.0	5.07	25.74 ± 6.03	1.76	3.87 ± 2.20
RX J1832.2+6832	18:32:13.3	68:32:26	0.1981	18.7 ± 3.9	2.8	2.11	4.17 ± 1.05	1.74	3.12 ± 1.79

RX J1832.5+6449	18:32:31.5	64:49:49	0.1610	73 ± 4.1	4.6	4.57	20.71 ± 4.81	12.45	20.15 ± 1.62
RX J1832.5+6848	18:32:35.0	68:48:05	0.2050	241 ± 11	7.4	9.20	86.38 ± 20.00	2.80	4.14 ± 1.48
RX J1833.7+6521	18:33:44.6	65:21:37	0.1621	19.7 ± 2.3	3.0	2.39	5.07 ± 1.20	-1.77	-2.50 ± 1.41
RX J1834.1+7057	18:34:08.2	70:57:23	0.0803	9.36 ± 1	2.3	1.66	2.30 ± 0.55	3.85	12.77 ± 3.31
RX J1836.5+6344	18:36:31.0	63:44:30	0.0846	34.6 ± 1.8	3.4	3.00	8.80 ± 2.04	7.07	11.70 ± 1.66
RX J1838.2+6321	18:38:12.6	63:21:02	0.2167	43.1 ± 5.1	3.7	3.19	10.32 ± 2.45	-1.30	-1.94 ± 1.49
RX J1839.2+7018	18:39:17.4	70:18:20	0.2297	18.7 ± 4.5	2.8	2.07	4.12 ± 1.07	-1.04	-2.87 ± 2.77
RX J1804.2+6729	18:04:15.6	67:29:21	0.0617	0.431 ± 0.091	0.7	0.27	0.05 ± 0.01	0.48	0.75 ± 1.57
RX J1806.4+7028	18:06:24.9	70:28:40	0.0971	7.49 ± 0.93	2.1	1.43	1.75 ± 0.42	0.29	0.60 ± 2.09
RX J1806.8+6537	18:06:51.6	65:37:46	0.2626	49.6 ± 3.5	3.9	3.37	11.77 ± 2.74	4.33	11.22 ± 2.59
RX J1806.1+6813	18:06:06.6	68:13:08	0.3030	43.1 ± 4.9	3.7	3.04	9.66 ± 2.29	3.10	2.37 ± 0.77
RX J1807.5+6429	18:07:32.3	64:29:17	0.2391	11.2 ± 2.4	2.4	1.63	2.39 ± 0.61	-0.24	-0.58 ± 2.41
RX J1808.7+6557	18:08:43.6	65:57:05	0.2460	9.36 ± 1.4	2.3	1.52	2.07 ± 0.50	-0.88	-2.17 ± 2.45

Table 2.1: The first four columns and column 6 are directly from Henry et al. (2006). Column 5 is the X-ray luminosity in 0.5-2.0 keV band within R_{500} (see text). Column 7 is the halo mass within R_{500} estimated from the $M_{500} - T_X$ relation from Kettula et al. (2015) given the temperature in column 6. Column 8 is the X-ray analog of the SZ luminosity within R_{500} . Column 9 is the SZ signal-to-noise ratio calculated using Equation 2.5. Column 10 is the total SZ flux computed from Equation 2.4.

Relation (Y - X)	Method	α	β	$\sigma_{log,int}$	Bias Corrected α	Bias Corrected β	Bias Corrected $\sigma_{log,int}$
$Y_{sph,500}D_A^2E(z)^{-2/3}$ - M_{500}	Bayesian	$-0.61^{+0.10}_{-0.10}$	$1.37^{+0.20}_{-0.20}$	$0.30^{+0.06}_{-0.05}$ (70%)	$-0.65^{+0.11}_{-0.11}$	$1.32^{+0.21}_{-0.21}$	$0.35^{+0.07}_{-0.06}$ (81%)
	Orthogonal	$-0.78^{+0.09}_{-0.09}$	$1.77^{+0.20}_{-0.20}$	$0.20^{+0.03}_{-0.03}$ (46%)	$-0.86^{+0.09}_{-0.09}$	$1.85^{+0.21}_{-0.21}$	$0.32^{+0.03}_{-0.03}$ (73%)
$Y_{sph,500}D_A^2E(z)^{-2/3}$ - $L_{X,500}E(z)^{-7/3}$	Bayesian	$-0.30^{+0.07}_{-0.07}$	$0.74^{+0.11}_{-0.11}$	$0.34^{+0.06}_{-0.05}$ (77%)	$-0.33^{+0.08}_{-0.08}$	$0.73^{+0.12}_{-0.12}$	$0.37^{+0.07}_{-0.05}$ (85%)
	Orthogonal	$-0.35^{+0.07}_{-0.07}$	$0.89^{+0.11}_{-0.11}$	$0.24^{+0.06}_{-0.06}$ (56%)	$-0.40^{+0.07}_{-0.07}$	$0.91^{+0.12}_{-0.12}$	$0.35^{+0.01}_{-0.01}$ (81%)
$Y_{sph,500}D_A^2$ - $Y_{X,500}$	Bayesian	$0.06^{+0.07}_{-0.08}$	1 (fixed)	$0.39^{+0.06}_{-0.05}$ (90%)	$-0.01^{+0.08}_{-0.08}$	1 (fixed)	$0.44^{+0.07}_{-0.06}$ (102%)
	Orthogonal	$0.19^{+0.08}_{-0.08}$	1 (fixed)	$0.28^{+0.03}_{-0.03}$ (65%)	$0.15^{+0.09}_{-0.09}$	1 (fixed)	$0.33^{+0.02}_{-0.02}$ (77%)

Table 2.2: Estimated parameters for various scaling relations under the assumption that all systems follow the "universal pressure profile" from Arnaud et al. (2010).

Relation (Y - X)	Method	α	β	$\sigma_{log,int}$	Bias Corrected α	Bias Corrected β	Bias Corrected $\sigma_{log,int}$
$Y_{sph,500}D_A^2E(z)^{-2/3}$ - M_{500}	Bayesian	$-0.89^{+0.08}_{-0.09}$	$1.75^{+0.17}_{-0.17}$	$0.30^{+0.06}_{-0.05}$ (70%)	$-0.95^{+0.09}_{-0.10}$	$1.73^{+0.19}_{-0.18}$	$0.33^{+0.06}_{-0.06}$ (77%)
	Orthogonal	$-0.91^{+0.09}_{-0.09}$	$2.03^{+0.20}_{-0.20}$	$0.16^{+0.03}_{-0.03}$ (37%)	$-0.98^{+0.09}_{-0.09}$	$2.09^{+0.20}_{-0.20}$	$0.27^{+0.02}_{-0.02}$ (62%)
$Y_{sph,500}D_A^2E(z)^{-2/3}$ - $L_{X,500}E(z)^{-7/3}$	Bayesian	$-0.56^{+0.06}_{-0.07}$	$0.90^{+0.08}_{-0.08}$	$0.31^{+0.05}_{-0.04}$ (72%)	$-0.62^{+0.07}_{-0.07}$	$0.89^{+0.09}_{-0.08}$	$0.34^{+0.06}_{-0.05}$ (78%)
	Orthogonal	$-0.42^{+0.07}_{-0.07}$	$1.05^{+0.12}_{-0.12}$	$0.24^{+0.07}_{-0.07}$ (56%)	$-0.48^{+0.07}_{-0.07}$	$1.07^{+0.12}_{-0.12}$	$0.34^{+0.02}_{-0.02}$ (79%)
$Y_{sph,500}D_A^2$ - $Y_{X,500}$	Bayesian	$0.04^{+0.06}_{-0.07}$	1 (fixed)	$0.35^{+0.06}_{-0.05}$ (81%)	$-0.02^{+0.07}_{-0.08}$	1 (fixed)	$0.39^{+0.06}_{-0.05}$ (90%)
	Orthogonal	$0.15^{+0.07}_{-0.07}$	1 (fixed)	$0.17^{+0.04}_{-0.04}$ (40%)	$0.13^{+0.08}_{-0.08}$	1 (fixed)	$0.23^{+0.04}_{-0.04}$ (54%)

Table 2.3: Same as Table 2.2 but assuming each system follows the mass dependent pressure profile from Battaglia et al. (2010).

There are a few ways to investigate the trends between X-ray and SZ properties. In the presence of considerable amounts scatter, regressing one variable on the other does not necessarily provide the best estimate of the true relation. In such cases, orthogonal regression is commonly used to better model the data. We note that orthogonal regression always yields a steeper slope compared to regressing one variable on another when there is significant scatter. Orthogonal fits were performed using the *bivariate correlated errors and intrinsic scatter* (BCES) method following the formalism presented by Akritas & Bershady (1996).

Aside from the statistical scatter, $\sigma_{x,y}$, it is useful to quantify the additional spread in the data known as intrinsic scatter, σ_{int}. The total scatter, σ_{tot}, includes both of these such that

$$\sigma_{tot} = \sqrt{\sigma_{int}^2 + \langle\sigma_y\rangle^2 + (\beta\langle\sigma_x\rangle)^2} \tag{2.8}$$

We estimated σ_{tot} from the distribution of residuals about the mean relation bounded by the 25^{th} and 75^{th} percentiles. We then matched this 50% probability to that in a normal distribution where 50% is bounded by $\pm 0.67\sigma$. We then estimated the uncertainties on the intrinsic scatter by bootstrap re-sampling.

We also performed linear regression using a Bayesian method, following a similar approach to Isobe et al. (1986) in order to account for censored data. We maximized the likelihood function of our data, $\psi = \{x, y, \sigma_x, \sigma_y\}$, given the model parameters $\theta = \{\alpha, \beta, \sigma_{int}\}$. The likelihood function can be expressed as

$$L(\theta|\psi) \propto \prod_{i\in D}^{m} P_D(\psi_i|\theta) \prod_{j\in C}^{n} P_C(\psi_j|\theta) \tag{2.9}$$

$$P_D \propto f(\psi_i) = \frac{\exp\left(\frac{(y_i-\alpha-\beta x_i)^2}{-2\left(\sigma_{int}^2+\sigma_{y,i}^2+(\beta\sigma_{x,i})^2\right)}\right)}{\sqrt{2\pi\left(\sigma_{int}^2 + \sigma_{y,i}^2 + (\beta\sigma_{x,i})^2\right)}} \tag{2.10}$$

$$P_C \approx \int_{-\infty}^{\psi_j} f(z)dz \tag{2.11}$$

where $\prod_D^m P_D$ represents the product of conditional probabilities over m detections and $\prod_C^n P_C$ is the same for censored data over n nondetections. For censored data, y_i becomes an upper limit on the SZ flux which was calculated at the 3σ level using the median flux uncertainty of all objects within $-1.35 < SNR < 1.35$. In the Bayesian approach, σ_{int} is estimated as a free parameter.

We also corrected our data for Malmquist bias. This bias arises in any flux-limited

sample; it is the tendency to detect brighter objects near the flux limit as they can be seen at larger distances. Corrections for this bias has be done by Vikhlinin et al. (2009) and Planck Collaboration et al. (2014d) and we adopt their same method. The mean bias, b, is denoted by

$$\ln\, b = \langle \ln\, L - \ln\, L_0 \rangle = \frac{\exp(-\mathrm{x}_{\mathrm{min}}^2/2\sigma^2)}{\sqrt{\pi/2}\ \mathrm{erfc}(\mathrm{x}_{\mathrm{min}}/(\sigma\sqrt{2}))}\ \sigma \tag{2.12}$$

where L is the "true luminosity", L_0 is the measured luminosity, $x_{min} = \ln\, f_{min} - \ln\, f_0$ with f_{min} being the minimum detected flux, σ is the log-normal scatter in the relation. Since we do not know the scatter a priori, we estimated it empirically using σ_{tot} as described above.

Malmquist bias corrections required quantifying the survey limitations. The two limits used in this study were the selection of SZ sources based on SNRs, and the cutoff in the X-ray photon count rate which was 0.002 counts s^{-1} from Henry et al. (2006). The SZ flux limit was estimated by fitting a line to predict the SZ flux as a function of SNR. This line was extrapolated to the SNR cutoff (1.35), yielding a flux limit of 0.0019 arcmin^2. The survey limit in mass can be scaled from the X-ray photon count rate which is proportional to the X-ray flux and luminosity. We then used the $L_X - T_X$ relation from White et al. (1997) and the $M_{500} - T_X$ relation from Kettula et al. (2015) to scale the count rate limit to a mass limit. A similar procedure was done for the corrections on Y_X.

2.6 Analysis and Discussion

2.6.1 Comparisons of Scaling Relations

Here we discuss the values of the best fit parameters for the scaling relations and their implications. In particular, we investigate the differences in our adoption of pressure profiles i.e., UPP vs. BPP. We specifically focus on the estimated parameters using our Bayesian technique and bias corrected data. We also simplify the expression $Y_{sph,500} D_A^2 E(z)^\gamma \rightarrow Y_{SZ,500}$ where γ is specified in Table 2.2 and Table 2.3 for each relation.

The slope of the $Y_{SZ,500} - M_{500}$ relation using the BPP is slightly steeper than the self-similar prediction (5/3), but it is consistent within the uncertainties. It is also somewhat in agreement with recent observational works (e.g., Jimeno et al. 2018) and theoretical studies (e.g., Planelles et al. 2017) as shown by the different lines in Figure 2.4. On the other hand, the relation found using the UPP suggests a much flatter slope that is less consistent with the self-similar scaling, however, it is still within 2σ. The intrinsic scatter is quite large ($\sim 80\%$) compared to other studies. Simulations predict a much smaller scatter of $\sim 5-15\%$ (Nagai 2006, Planelles et al. 2017). We attribute this large intrinsic scatter to the lack of

independent measurements of T_X which were used to estimate the masses. We discuss this further in the next section.

Our results of the $Y_{SZ,500} - L_{X,500}$ relation suggest a slope of 0.89 using the BPP and 0.73 using the UPP. These results suggest $\sim 4\sigma$ differences from the self-similar slope of 5/4 and about $\sim 3\sigma$ differences from the slope of 1.07 reported by Arnaud et al. (2010) (albeit their results are reported in the 0.1–2.4 keV band while ours are in the 0.5–2.0 keV band). The bias corrected slope of 1.12 found by Planck Collaboration et al. (2011b) within the 0.5–2.0 keV band is within $\sim 3\sigma$ of our values. Our data seem to systematically lie above the relation of Planck Collaboration et al. (2011b) with a scatter of $\sim 80\%$ which is nearly twice their value.

The $Y_{SZ,500} - Y_{X,500}$ relation gives insight into the amount of inhomogeneity or clumpiness in the ICM as well as the concentration of the gas toward the inner regions. Since Y_X is the analog to the SZ luminosity, one might expect the $Y_{SZ,500}/Y_{X,500}$ ratio to be unity, however, $Y_{SZ,500}/Y_{X,500}$ has been found to be slightly smaller than unity from other observational work (e.g., Arnaud et al. 2010, Planck Collaboration et al. 2011b, Rozo et al. 2012). This ratio is really a comparison of the mass weighted temperature to the spectroscopic temperature and is expected to be smaller than unity for a decreasing temperature profiles (Arnaud et al. 2010). Our results suggest a ratio of 0.98 and 0.95 using the UPP and BPP respectively, which is in agreement with previous studies. We also point out that objects with low $Y_{X,500}$ values tend to systematically lie above the line of unity for both pressure profiles. This is an interesting result that may be an artifact from the assumed pressure profiles. We discuss this further in the next section.

2.6.2 Caveats

Here we analyze the limitations of our data and the validity of the necessary assumptions made. We also discuss what must be done in the future to improve future joint X-ray–SZ studies.

One limitation in this study was that the only raw X-ray measurements available were the count rates within an aperture of R_{200}. The count rates were converted into luminosities which were then used to estimate the temperatures using the $L_X - T_X$ relation from White et al. (1997). We then used those temperatures to estimate M_{500} using the $M_{500} - T_X$ relation from Kettula et al. (2015). Ultimately, the values of T_X and M_{500} were derived from the count rates.

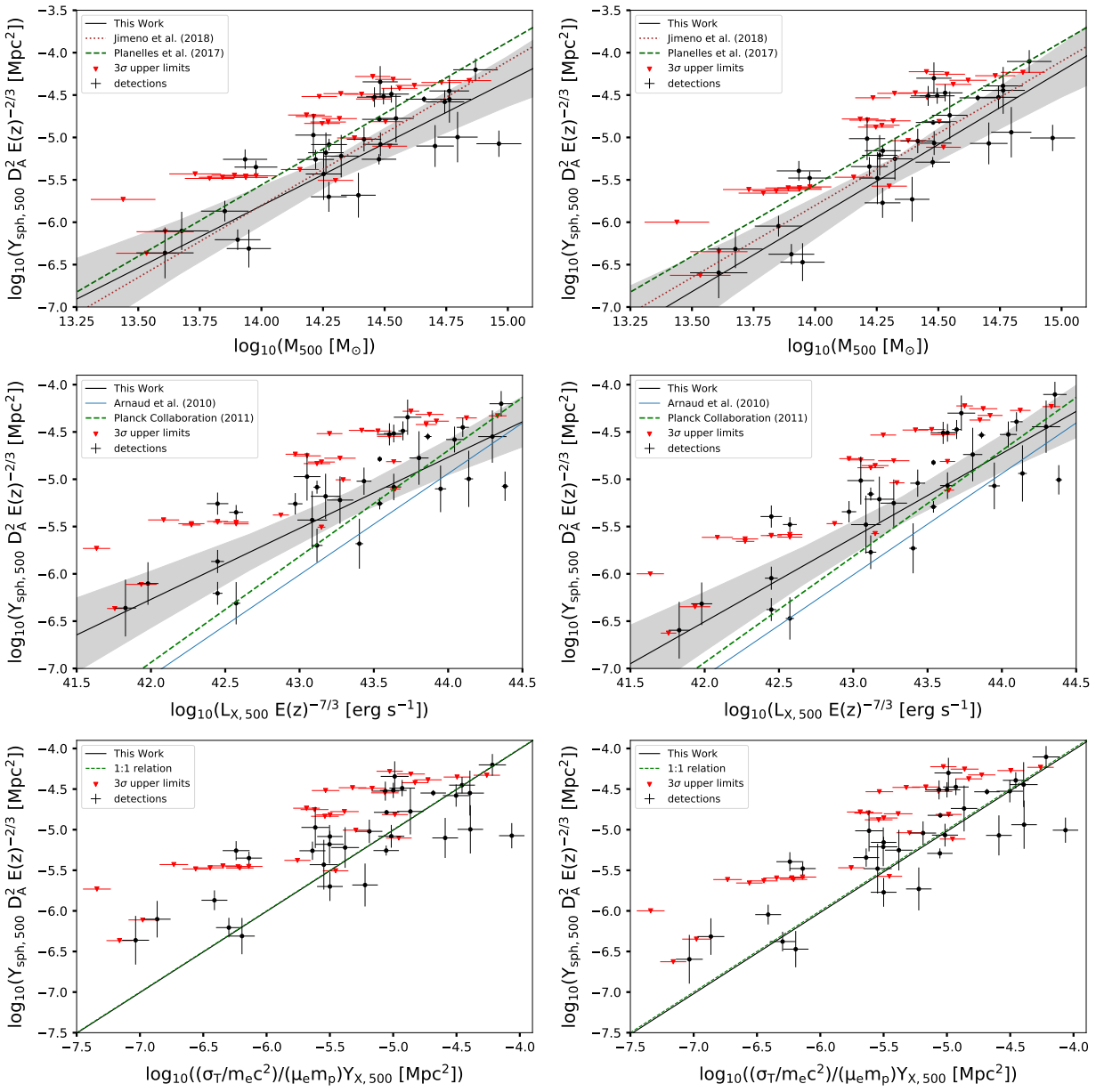


Figure 2.4 The left column shows the SZ data using the UPP and the right column is from the BPP. The solid black lines in each plot represents the best fit using our Bayesian method on bias corrected data described in subsection 2.5.2. The black data with error bars represent the SZ detections with SNR > 1.35 while the red triangles are the nondetections placed at 3σ. The shaded regions in the top two rows denote the 95% confidence bands around the best fit relation. Results from previous studies are also shown for comparison. In the bottom row, the black line and dashed green line appear to lie on top of each other, but the black line is slightly below the dashed green line (1:1 relation).

RA	Dec	SNR	Y_{SZ} $[10^{-4}$ arcmin$^2]$	ID	α(J2000)	δ(J2000)	z
18:35:40.8	66:47:05.9	4.07	6.2 ± 1.5	...	...	...	...
17:46:36.9	68:44:59.9	4.09	6.9 ± 1.7	WARP J1746.3+6849W	17:46:19.0	+68:49:50.0	0.203
				400d J1746+6848	17:46:29.1	+68:48:54.0	0.217
				WARP J1746.3+6849E	17:46:33.0	+68:48:50.0	0.307
17:48:26.4	64:59:07.1	4.22	6.2 ± 1.5	WHL J174744.2+645225 [a]	17:47:44.2	+64:52:25.0	0.3758
17:47:45.6	64:52:14.0	4.67	6.6 ± 1.4	WHL J174744.2+645225 [a]	17:47:44.2	+64:52:25.0	0.3758
17:16:41.6	67:10:41.1	4.83	6.9 ± 1.4	RX J1716.4+6708	17:16:49.6	+67:08:30.0	0.813
18:44:21.9	64:17:34.2	5.23	6.6 ± 1.3	WHL J184505.8+642618	18:45:05.8	+64:26:18.1	0.3002
				WHL J184502.2+641754	18:45:02.2	+64:17:54.3	0.4353
17:55:00.7	64:21:15.7	5.50	6.4 ± 1.2	WHL J175517.4+641630 [b]	17:55:17.4	+64:16:29.0	0.2837
18:24:33.4	69:20:02.9	6.77	8.8 ± 1.3	...	...	...	...
18:21:24.0	64:21:35.3	9.45	20.0 ± 2.1	WHL J182203.5+642301	18:22:03.5	+64:23:01.1	0.3315
18:31:27.7	62:18:57.0	13.38	15.9 ± 1.2	PSZ1 G091.82+26.11	18:31:08.2	+62:14:51.7	0.24

Table 2.4: Presented are the coordinates of the regions which have high SNR values (SNR ≥ 4) and the number of groups/clusters within a $10'$ radius according NED.
a - These are overlapping regions that contain the same cluster within $10'$.
b - This region contains a confirmed cluster detected by Gioia et al. (2003) which was the optical identification program used to construct the X-ray NEP catalog. Henry et al. (2006) did not include this in their catalog as it did not meet all requisites for their final catalog.

The measurements of total X-ray luminosities are probably a strong source for the large amounts of intrinsic scatter in our scaling relations. X-ray scaling relations involving the total luminosity show the largest amounts of scatter, especially when the cores have not been excised. Virialized systems may eventually develop cores with very short cooling times that boost their X-ray luminosities. Due to this excess luminosity, the cores ($R \lesssim 0.15\ R_{500}$) are typically ignored in scaling relation studies (e.g., Mantz et al. 2016). The X-ray luminosities used in this study were calculated without excising the central regions, so we expect at least a few cool cores to be present in our sample. An example of a potential cool core system is the object containing the highest mass, luminosity, and $Y_{X,500}$ in Figure 2.4. This datum seems to lie significantly below the predicted line for all three scaling relations. The presence of a strong cool core would cause us to overestimate its mass and shift the datum to the right.

Systems may also be morphologically disturbed which tend to down scatter the luminosity from the mean relation (Pratt et al. 2009). The fact that different systems exhibit a variety of morphologies can contribute to large observed scatter (Marrone et al. 2012). It has been shown that the scatter in X-ray scaling relations is reduced once the cores have been excised and when morphologically disturbed systems have been accounted for (Pratt et al. 2009, Arnaud et al. 2010).

The unresolved nature of our SZ measurements required making assumptions about the pressure profiles for each system. We first assumed each system followed the UPP from Arnaud et al. (2010). While this may be applicable to massive clusters, it is probably a poor assumption to make for groups if there is significant AGN feedback. Simulations and observations have shown that the UPP can overestimate $Y_{SZ,500}$ by almost an order of magnitude down toward masses $M_{500} \sim 10^{13} M_{\odot}$ (Le Brun et al. 2015, Lim et al. 2018). This may be causing our objects with low $Y_{X,500}$ values to systematically lie above the 1:1 line in the bottom-left panel of Figure 2.4. To account for this, we also considered the mass- and redshift-dependent pressure profiles derived by Battaglia et al. (2010). The BPP can lower $Y_{SZ,500}$ by $\lesssim 30\%$ relative to the UPP for systems $M_{500} \lesssim 10^{14.5} M_{\odot}$. While the BPP may be a more realistic for groups compared to the UPP, it does not evade the inevitable problem of assuming a pressure profile. One would expect each system to experience different amounts of AGN feedback while also existing in a variety of virialization states. Again, these differences are expected to be more pronounced in groups than clusters.

Our last noteworthy assumption was made in calculating $M_{gas,500}$. After solving for the emission measure using Equation 2.7, we adopted an isothermal β model for the density distribution, assuming all systems follow a density distribution with $\beta = 2/3$. The β model is a good first order approximation, however, others have argued for better models of the density

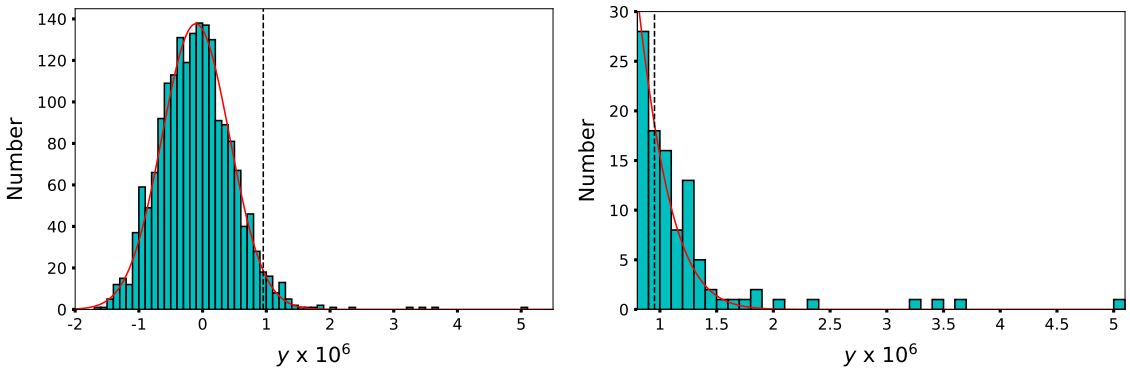


Figure 2.5 In both panels, the red line represents the best fit Gaussian curve and the dashed gray line indicates 2σ above the mean. The left panel shows the full distribution of the average values of circles for the entire random array. The right panel is zoomed in to clearly show the outliers.

distribution (e.g., Vikhlinin et al. 2006, Hallman et al. 2007). Even with the assumption of the isothermal β model, it has been shown that groups typically exhibit smaller values of beta (i.e., flatter profiles) which would increase our estimates of the total gas mass in lower mass systems. In order to acquire more accurate measurements of $Y_{X,500}$, it would be ideal to use systems that are resolved in X-rays.

2.6.3 Future Work

In this study, we quantified the effects of assuming different pressure profiles to calculate $Y_{SZ,500}$. The large amounts of intrinsic scatter compared to other studies suggests that scaling relations can be improved with resolved data. In order to avoid making strong assumptions, resolved SZ or X-ray surface brightness profiles are needed to construct accurate pressure profiles for individual halos. X-rays can provide temperature and density profiles near the central regions, which is useful for constraining the amount of the SZ flux stemming from the outer regions ($\gtrsim R_{500}$). We can then extrapolate the profiles out to large radii to get a sense of how effective AGN are at driving gas outward. Moreover, one could directly measure the pressure profiles at large radii using resolved SZ data. This has been done using nearby, massive clusters (e.g., Planck Collaboration et al. 2016c), however, little attention has been given to groups since they produce weaker signals. Resolved observations for these low-mass systems would provide the best evidence for the effects of AGN feedback in groups. In addition to the X-ray detected groups/clusters near the NEP, we searched the y-maps for any objects that may have been missed by the NEP X-ray survey. Due to the redshift independent nature of the SZ effect and the flattening of the angular distance from $0.5 \lesssim z \lesssim 2$, it is possible to detect groups/clusters in the y-maps but not in X-rays.

We started a search for these objects using an array of $10'$ circles across the NEP. There were a total of 1874 circles inside the limits of the NEP study while containing $\geq 75\%$ of uncontaminated area. The distribution of the average values of these circles is presented in Figure 2.5.

We further investigated the 59 circles with average values lying 2σ above the mean. These circles were reduced to 31 group/cluster candidates. Since we did not have X-ray data for these objects —meaning we did not have estimates of M_{500} —we fit PSF profiles to them in order to get a SNR. We found 30 candidates with $SNR > 1.35$ and 10 with $SNR > 4$. Using the 10 highest SNR regions, we searched the NASA Extragalactic Database for archival data on these candidates within a $10'$ radius. We found that 8/10 of the candidates were confirmed clusters that went undetected in the NEP X-ray catalog. There was one exception of a cluster that was excluded from the NEP X-ray catalog that was previously detected by the NEP optical program (Gioia et al. 2003). The results are presented in Table 2.4. While the NEP X-ray catalog is one of the deepest X-ray catalogs to exist, these results show that there are many groups/clusters in this region that need follow-up X-ray observations.

2.7 Summary and Conclusions

The main goal of this work was to measure the SZ–X-ray scaling relations of galaxy groups and clusters near the NEP. The NEP is perhaps the best region of the sky with both deep X-ray and SZ data, allowing one to investigate a considerable sample of individual galaxy groups and low-mass clusters. We highlight the main aspects and conclusions of this work below.

1. This study investigated a sample of 62 galaxy groups and clusters detected in X-rays by Henry et al. (2006) and optically by Gioia et al. (2003). We were able to extract the SZ signal from 32 unresolved systems with SNRs > 1.35. The remaining nondetections were placed as upper limits at the 3σ level when performing linear regression.

2. The unresolved nature of the X-ray and SZ data required making assumptions about the pressure profile of each system in order to convert the total SZ flux into the fraction inside R_{500}. We considered two pressure profiles: the UPP, which is the observational "universal pressure profile" of galaxy clusters from Arnaud et al. (2010), and the BPP, which is the mass-dependent pressure profile derived from the simulations of Battaglia et al. (2010).

3. The scaling relations were derived using a Bayesian linear regression technique that takes into account nondetections. We estimated a slope of $1.73^{+0.19}_{-0.18}$ for the $Y_{SZ,500} -$

M_{500} relation using the BPP, which is consistent with the self-similar prediction as well as other observational and theoretical studies of massive clusters. The derived $Y_{SZ,500} - L_{X,500}$ scaling relation using the BPP yielded a slope of $0.89^{+0.09}_{-0.08}$, which is much flatter than the self-similar slope as well as those reported by other observational works; we note, however, that our orthogonal regression produces a steeper slope of 1.07 ± 0.12 that is consistent with previous studies. The $Y_{SZ,500} - Y_{X,500}$ relation using the BPP data yields an intercept value of $-0.02^{+0.07}-0.08$ when the slope was fixed to unity; this is slightly smaller than zero which is consistent with previous findings.

4. The choice between the UPP and the BPP has significant effects on the scaling relations. The derived scaling relations using the UPP yields larger intercepts and flatter slopes compared to the BPP. We considered the BPP to be a more realistic description of the pressure profiles across our mass spectrum, however, they need to be confirmed with resolved X-ray and/or SZ observations toward the low-mass regime.

5. We conducted a blind search for strong SZ signals near the NEP aside from the groups and clusters cataloged by Henry et al. (2006). The search yielded 10 regions with strong SZ signals above the background, and 8/10 candidates have known galaxy clusters in the vicinity after searching NED. These are excellent targets for follow-up X-ray observations that would help build more complete sample of galaxy groups and clusters near the NEP.

This study demonstrates one can conduct a sizable study of galaxy groups and low-mass clusters with current X-ray and SZ data. Given the low sensitivity of the *Planck* y-maps, having available X-ray data allows one to exploit low-SNR SZ signals. In addition, we stress the importance of using resolved X-ray data if one wants to conduct an accurate study of the SZ scaling relations using the current y-maps from Planck Collaboration et al. (2016b).

We thank the many individuals who offered guidance and insight, including Zhijie Qu, Chris Miller, Yanson Yun, and the anonymous referee, whose comments and suggestions helped improve this work. We are grateful for support from NASA through the Astrophysics Data Analysis Program, awards NNX15AM93G and 80NSSC19K1013. The work is based on observations obtained with *Planck*, http://www.esa.int/Planck, an ESA science mission with instruments and contributions directly funded by ESA Member States, NASA, and Canada. This research made use of the High Energy Astrophysics Science Archive Research Center (HEASARC) and the NASA/IPAC Extragalactic Database (NED), which are supported by NASA.

CHAPTER 3

The Resolved Sunyaev–Zel'dovich Profiles of Nearby Galaxy Groups

3.1 Abstract

Much of the baryons in galaxy groups are thought to have been driven out to large distances ($\gtrsim R_{500}$) by feedback, but there are few constraining observations of this extended gas. This work presents the resolved Sunyaev–Zel'dovich (SZ) profiles for a stacked sample of 10 nearby galaxy groups within the mass range $\log_{10}(M_{500}[M_{\odot}]) = 13.6 - 13.9$. We measured the SZ profiles using the publicly available y-map from the Planck Collaboration as well as our own y-maps constructed from more recent versions of *Planck* data. The y-map extracted from the latest data release yielded a significant SZ detection out to 3 R_{500}. In addition, the stacked profile from these data was consistent with simulations that included AGN feedback. Our best-fit model using the latest *Planck* data suggested a baryon fraction $\approx 5.6\%$ within R_{500}. This is significantly lower than the cosmic value of $\approx 16\%$, supporting the idea that baryons have been driven to large radii by AGN feedback. Lastly, we discovered a significant ($\sim 3\sigma$) "bump" feature near ~ 2 R_{500} that is most likely the signature of internal accretion shocks.

3.2 Introduction

In the present epoch, most of the baryons in the Universe have fallen into deep potential wells carved out by galaxies, galaxy groups, and galaxy clusters. Strong gravitational forces from the most massive dark matter systems, namely galaxy groups and clusters, have condensed much of the accreted material into hot, gaseous halos known as the intragroup medium (IGrM) and intracluster medium (ICM). One might expect these halos to heat in a self-similar manner since gravity is a scale-free force (Kaiser 1986). In reality, this self-similarity scaling is perturbed by non-gravitational processes such as stellar feedback, active galactic

nucleus (AGN) feedback, radiative cooling, and accretion shocks.

Observational and theoretical work has provided strong evidence that AGN feedback is likely the main culprit in disrupting the atmospheres of galaxy groups and clusters (see Gitti et al. 2012; for a review). AGN jets blast energy into the ICM/IGrM, expanding to tens of kpc, and carve out large cavities in the X-ray emitting gas (Gaspari et al. 2013, Liu et al. 2019, Lacy et al. 2019, Pasini et al. 2020). These outflows heat the surrounding medium and drive low entropy gas away from the central regions. This idea gained attention when trying to explain the observed lack of star formation in the center of galaxy clusters, known as the "cooling flow problem" (McNamara & Nulsen 2007b).

Even in the presence of AGN feedback, gas is still able to cool and condense inside the halo, especially near the edges of the X-ray bubbles. The cold gas then rains back down onto the galaxies, refuels the central engine, and induces a self-regulated cycle (Gaspari et al. 2011; 2013, Li et al. 2015, Gaspari et al. 2017, McDonald et al. 2018, Tremblay et al. 2018, McDonald et al. 2019, Russell et al. 2019). Nevertheless, there is still debate regarding which physical mechanisms are most responsible for regulating these outflows (Gaspari et al. 2020). Many parameters still need to be tuned by theorists in order to match observations such as: the accretion zone size, the amount of kinetic and thermal feedback, the opening jet angle, ambient gas density, and the angular momentum of the accreting gas (Meece et al. 2017, Prasad et al. 2020).

To further complicate this picture, the effects of feedback are predicted to depend on the halo mass. Given the fact groups exist in shallower potential wells than clusters, outflows from galaxy groups do not have to fight as hard to propagate outward. Therefore, AGN outflows may be capable of driving gas from the central regions of galaxy groups out to large distances ($\gtrsim R_{500}$ [1]; Roychowdhury et al. 2005, Mukherjee et al. 2019, Ishibashi & Fabian 2016). In turn, one would expect to see a deficit of gas within R_{500} relative to the self-similar prediction for low-mass systems, and this prompted the search for the predicted "breaking" of scaling relations (Eckmiller et al. 2011, Gaspari et al. 2014, Lovisari et al. 2015, Paul et al. 2017, Farahi et al. 2018, Pratt & Bregman 2020, Sereno et al. 2020). Much of the observational work to-date has focused on the gas properties within R_{500}, but very few measurements have been made of the extended gas.

X-ray observations have given excellent insight on the thermal profiles of the inner parts of the IGrM and ICM due to the squared dependence of the density in the emission measure. On the other hand, the Sunyaev–Zel'dovich (SZ) effect is linearly dependent on the gas density which makes it a more sensitive tracer of diffuse gas at large radii. Both X-ray and SZ observations have been used to study massive galaxy clusters ($M_{500} \gtrsim 10^{14} M_{\odot}$),

[1] R_{500} is the radius at which the density is 500$\times$ the critical density of the Universe.

revealing that cluster thermal profiles appear remarkably self-similar outside their cores (Pratt et al. 2009, Arnaud et al. 2010, Sayers et al. 2013, Mantz et al. 2016). Galaxy groups ($M_{500} \lesssim 10^{14} M_{\odot}$), however, are not expected to show the same degree of self-similarity as rich clusters. In particular, galaxy groups are expected to exhibit flatter pressure profiles caused by AGN feedback (Le Brun et al. 2015; hereafter L15).

The impact of AGN feedback on the pressure profiles of galaxy groups can be tested with resolved SZ signals. Currently, the best publicly available all-sky SZ maps (y-maps) were constructed from *Planck* data using two modified *Internal Linear Combination* (ILC) algorithms (Planck Collaboration et al. 2016b). They were generated using the second version of *Planck* data (PR2) and were labeled as the *NILC* and *MILCA* y-maps. These y-maps have led to substantial studies of unresolved, massive galaxy clusters. Herein, we refer to the *NILC* map as the "public y-map" and eventually call it "PR2NILC"; we do not report on *MILCA*.

Only nearby objects are resolved by the coarse resolution of the public y-map (full width at half maximum [FWHM] = 10'). Resolved SZ profiles have been measured for nearby clusters (Planck Collaboration et al. 2013a;b; 2016c), but little attention has been given to nearby galaxy groups. In this work, we investigate the resolved SZ profiles of 10 galaxy groups within 3500 km s^{-1} from the catalog produced by (Kourkchi & Tully 2017; hereafter KT17).

The rest of the paper is structured in the following way: section 3.3 describes the sample selection of galaxy groups from the KT17 catalog; section 3.4 presents the *Needlet Internal Linear Combination* (NILC) method used to construct our own y-maps from newer and improved versions of *Planck* data; section 3.5 presents the methodology used to extract the radial SZ profiles, remove sources of contamination, calculate uncertainties, and estimate bias corrections from Monte Carlo simulations; section 3.6 presents the results of the stacked SZ profile; section 3.7 discusses the differences between y-maps, presents estimates of the baryon fraction, and addresses the extended part of the SZ profile; and section 3.8 provides a brief summary of our work. Throughout this work we assume a cosmology with a Hubble constant of $H_0 = 70$ km s^{-1} Mpc^{-1}, and density parameters of $\Omega_m = 0.3$ and $\Omega_\Lambda = 0.7$.

3.3 Sample of Galaxy Groups

The sample of galaxy groups were drawn from the catalog constructed by KT17. It was assembled mainly using the 2MASS Redshift Survey, although it included archival data of low surface brightness systems to supplement their grouping algorithm. They limited their group sample to systems with recessional velocities <3500 km s^{-1} (Hubble distance $\approx$ 50

Mpc). At this distance, the survey was complete to L^* in the K_s band.

All galaxies had measured radial velocities, and an additional 19% also had independent distance estimates from *Cosmicflows-3* (Tully et al. 2016). *Cosmicflows-3* is a compilation of galaxy distances that has been built over the last decade (Tully et al. 2008; 2013) and is the latest version available. It is particularly useful to have independent distance measurements for galaxies in the nearby Universe since the magnitude of their peculiar motions may be comparable to their recessional velocities. All 10 objects in our final sample had reliable distance estimates ($\leq 15\%$ error), although this was not true for every system in the KT17 catalog.

The distance estimates were then combined with the apparent magnitudes in the K_s band to estimate luminosities. The K_s-band luminosity was then used as a proxy for the stellar mass. Stellar masses were converted into halo virial masses, M_v, using scaling relations from Tully (2015a). It is more customary, however, to work in units of M_Δ, where M_Δ is the mass enclosed by the radius defined by the overdensity parameter, Δ, relative to the critical density. Throughout this work we use $\Delta = 500$. In order to compare these masses with other works, we converted M_v to M_{500} using the relation $r_{200} = 0.198(\frac{M_v}{10^{12}M_\odot})^{1/3}h_{75}^{-2/3}$ from Tully (2015b) and assuming $r_{500} \approx 0.7r_{200}$.

For the purposes of this study, the KT17 catalog was filtered to select resolved systems that were fairly isolated on the sky. The criteria for our selection included:

1. $10^{13.6}M_\odot < M_{500} < 10^{14}M_\odot$.

2. The angular size of R_{500} was $> 40'$ to ensure the gas profiles were resolved in the y-maps, i.e., 0.25 $R_{500} \geq 10$'.

3. Galactic latitudes were $|b| > 15^\circ$ to avoid the most extreme contamination from the Galactic plane. We also masked regions where the SZ signal was highly correlated with the dust emission for each localized field (see subsection 3.5.1).

4. The number of member galaxies was ≥ 3.

5. Systems were required to possess a redshift-independent distance measurement.

6. Center positions of the objects were not within R_{500} or $20'$ (whichever was larger) of another known galaxy group/cluster from the *meta-catalogue of X-ray detected clusters of galaxies* (MCXC; Piffaretti et al. 2011), the *second Planck catalogue of Sunyaev–Zel'dovich sources* (PSZ2; Planck Collaboration et al. 2014d), or the KT17 catalog. For this procedure, we used objects with $M_{500} > 10^{12}M_\odot$ from the KT17 catalog. This ensured the objects of interest were isolated on the sky from other known groups/clusters.

The upper mass limit was selected because lower mass objects have not received a lot of attention in the literature, and all of the more massive objects in the catalog were well-known clusters (e.g., Virgo and Centaurus). We also imposed a lower mass limit for stacking purposes. One could consider halos within a mass range ~ 0.5 dex to be similar and stack them together. However, Figure 3.1 shows the predicted signal-to-noise ratio (S/N) eventually stopped increasing at a certain mass. This was determined by calculating the predicted signal for each object with $M_{500} < 10^{14}$ $M_\odot$ and assessing the noise levels in the PR2NILC y-map. The signal was estimated by finding the average SZ value within 0.25 R_{500} after convolving the AGN 8.0 pressure profile from L15 with the point spread function (PSF), assumed to be a 2D Gaussian beam of FWHM = 10' (Planck Collaboration et al. 2016b). The associated noise was estimated using the method described in subsection 3.5.2. Starting with the most massive object, we subsequently included lower mass systems and stacked their signals. The S/N of the stack stopped increasing once objects below $M_{500} < 10^{13.6}$ $M_\odot$ were included, therefore, we did not consider systems below this mass.

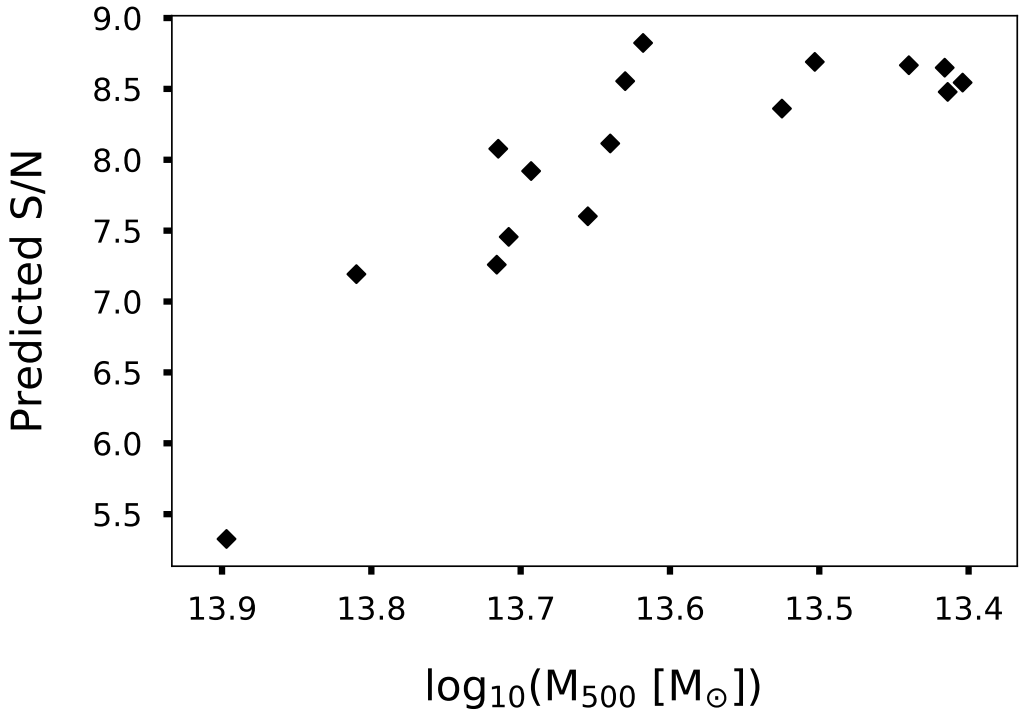


Figure 3.1 The predicted S/N of stacked groups by subsequently adding lower mass objects to the sample (note the backwards mass scale). For clarity, the second leftmost datum is the S/N one would expect when stacking the two most massive objects in the sample. The stacked S/N appears to stop increasing around $M_{500} \sim 10^{13.6}$ $M_\odot$ and we used this as a threshold for the lower mass limit.

PCG	l [°]	b [°]	MCXC Name	$\log_{10}(M_{500})$ $[\log_{10}([M_\odot])]$	R_{500} [arcmin]	Velocity [km s^{-1}]	Distance [Mpc]	Distance % Error [%]	BCG Name
39659	281.80280	67.37240		13.90	71.9	2224	31.4	4	NGC4261
13418	236.71250	-53.63970	MCXC J0338.4-3526	13.81	116.4	1502	18.1	3	NGC1399
64192	350.90020	-32.63890	MCXC J2009.9-4823	13.72	58.0	2916	33.9	4	NGC6868
49356	82.61060	71.63340		13.71	61.2	2408	32.0	6	NGC5353
45174	306.20280	32.27490	MCXC J1304.2-3030	13.71	44.4	3292	44.0	8	NGC4936
46247	311.23340	46.09540	MCXC J1315.3-1623	13.69	69.2	2488	27.9	5	NGC5054
40498	297.48480	22.83550		13.65	65.8	3258	28.5	6	NGC4373
33871	281.57860	21.08900		13.64	60.0	2864	30.9	6	NGC3557
53932	0.42740	48.79460	MCXC J1506.4+0136	13.63	68.7	1819	26.7	4	NGC5846
62870	339.69610	-25.13320		13.62	60.6	3443	30.0	15	NGC6753

Table 3.1: The first column (1) is the "PCG" identification number used to distinguish galaxy groups in KT17; (2) and (3) are the galactic coordinates in degrees; (4) is the identification of the system in the MCXC catalog if it existed; (5) is the logarithm of the estimated mass (in solar units) within R_{500} ; (6) is the angular size of R_{500} for each system in arcminutes; (7) is the recessional velocity of each galaxy group; (8) is the measured distance and (9) is its fractional uncertainty; (10) is the NGC identification for the BCG.

In the KT17 catalog, the luminosity-weighted positions of the galaxies were denoted as the center of each system. This position, however, was not the ideal center to extract the SZ signal. It is known that the center of the halo gas typically shares the same position of the brightest cluster galaxy (BCG; George et al. 2012). We defined the BCG as the most luminous galaxy within 0.15 R_{500} of the luminosity-weighted center if it existed, otherwise, we considered the most luminous galaxy within R_{500} to be the BCG. We searched within 0.15 R_{500} first in case there was a brighter galaxy a little further away from the luminosity-weighted center; in other words, preference was given to bright galaxies close to the luminosity-weighted center. Indeed, we found that 4/5 (80%) of the systems with X-ray information from the MCXC catalog were located closer to the BCG than the luminosity-weighted center. In cases where groups had center positions from MCXC, we adopted the X-ray position to be the center of the SZ extraction, otherwise, we used the position of the BCG. All of the relevant information on these systems is presented in table Table 3.1.

3.4 SZ Map Making

Here we present the data and methods used to create all-sky SZ maps (y-maps). In particular, we describe our use of data from the *Planck* mission and the *Wilkonson Microwave Anisotropy Probe* (*WMAP*). Then we present our NILC method to create y-maps.

3.4.1 Frequency Maps

The public y-map from Planck Collaboration et al. (2016b) was created using the second version of *Planck* data (Planck Collaboration et al. 2016d; "PR2"), however, there have been significant improvements to the *Planck* data processing in more recent years. For example, the third release of *Planck* data (Planck Collaboration et al. 2020a; "PR3") improved the *Low Frequency Instrument* pipeline by including Galactic emission and the CMB dipole in their calibration. Also, the *High Frequency Instrument* processing omitted 22 days of data taken during periods of increased Solar activity. Finally, PR3 implemented a different map-making algorithm that used foreground templates from PR2 to reduce systematic effects.

Further advancements were made in the fourth release of *Planck* data (Planck Collaboration et al. 2020c; "PR4"). For instance, PR4 increased the total integration time by about 8% relative to PR3 by including data taken during the repointing periods of the satellite. In addition, the data processing of PR4 identified and removed the artificial ringing patterns in the 353 GHz map from PR3 called "zebra stripes". PR4 also made improvements in suppressing another type of striping feature from turning time-ordered data of the sky into a

single image. These stripes occur along the scanning pattern of the satellite and can produce significant amplitudes if not dealt with properly (Ashdown et al. 2007). Various "destriping" algorithms have been applied throughout the *Planck* data releases, but PR4 implemented an extremely short baseline step of 167 ms. This short baseline reduced the noise levels on scales $\lesssim 5^\circ$ relative to the larger baselines used in PR3 and PR2. Finally, PR4 yielded less systematic noise, on all angular scales, compared to previous releases.

The public y-map was made exclusively with *Planck* data. This y-map exhibited strong residuals from radio sources due to the limited information at low frequencies. Radio sources with a power law emission will create negative "holes" in the y-map. This is because they cause an excess of power at low frequencies whereas the SZ effect causes a decrement. For our SZ extraction, we included more low frequency coverage with all-sky data from *WMAP* to better handle radio source contamination. Specifically, we used the 9-year *WMAP* data which provided an additional five bands that covered the 23 - 94 GHz range (Bennett et al. 2013).

Working with heterogeneous data sets (*Planck* and *WMAP*) came with notable caveats. PR4 data retained the Solar dipole in all frequency maps, but this component was deprojected in PR2, PR3 and *WMAP* data. Moreover, the CMB calibrations were all different among these data sets. For these reasons, we performed the SZ extraction using internal difference maps—that is the difference between subsequent frequency maps for a given data set. Taking the difference maps effectively nullified the CMB and solar dipole components, allowing us to work with PR4/PR3 and *WMAP* data together. In the next section we describe our extraction of the SZ signal using these internal difference maps. Moving forward, our y-maps created with the difference maps from PR4/PR3 and *WMAP* data will be labeled as "PR4NILC" and "PR3NILC" respectively, while the *NILC* y-map from Planck Collaboration et al. (2016b) will be referred to as "PR2NILC".

3.4.2 Internal Linear Combination

The SZ effect measures the energy boost gained by *Cosmic Microwave Background* (CMB) photons after they interact with hot electrons in the ICM or IGrM. It causes a decrease in the flux relative to the CMB at frequencies < 217 GHz and an increase at higher energies. The SZ surface brightness is measured as a dimensionless quantity, y, which is given by

$$\frac{\Delta T}{T_{\rm CMB}} = f(\nu) y \tag{3.1}$$

where $f(\nu)$ is the SZ spectral dependence, $\frac{\Delta T}{T_{\rm CMB}}$ is the change in temperature relative to the CMB. The formal analytical expression for $f(\nu)$ is

$$f(x) = \left(x\frac{e^x+1}{e^x-1} - 4 \right)(1+\delta(x, T_{\rm e})) \tag{3.2}$$

where $x = \frac{h\nu}{k_{\rm B}T_{\rm CMB}}$ ($k_{\rm B}$ is the Boltzmann constant, h is Planck's constant, and $T_{\rm CMB}$ is the temperature of the CMB), $T_{\rm e}$ is the temperature of the electrons, and δ is a relativistic correction (Itoh et al. 1998, Carlstrom et al. 2002). Relativistic corrections must be applied to extremely high-mass systems ($M_{500} \sim 10^{15}$ $\rm M_\odot$) but are negligible for galaxy groups. Also, one must calculate the effective $f(\nu)$ for wide-band observations by integrating over the instrumental transmission window.

The SZ signal is just one of many astrophysical components that contributes to the observed intensity. As mentioned above, using difference maps (in thermodynamic units [$K_{\rm CMB}$]) effectively cancels the contributions from the CMB and the Solar dipole. An internal difference map between two frequency channels, X_Δ, can be expressed with a single component model

$$X_\Delta(p) = f_\Delta S_{SZ}(p) + N_\Delta(p) \tag{3.3}$$

where f_Δ is the SZ spectral dependence of the difference map, S_{SZ} is the SZ signal, and N_Δ is the noise term which is usually dominated by foreground Galactic emission. For this single component model, the ILC estimator of the SZ signal (Delabrouille et al. 2009) is given by

$$\widehat{S_{SZ}}(p) = \frac{\mathbf{f}_\Delta^t\ (\widehat{\mathbf{R}}_\Delta(p))^{-1}}{\mathbf{f}_\Delta^t\ (\widehat{\mathbf{R}}_\Delta(p))^{-1}\ \mathbf{f}_\Delta}\ \mathbf{x}_\Delta(p) \tag{3.4}$$

where $\mathbf{f}_\Delta$ is the vector of the differences in the SZ frequency dependence, $\mathbf{x}_\Delta$ is the vector of difference maps, and $\widehat{\mathbf{R}}$ is the empirical covariance matrix of the difference maps (Eriksen et al. 2004). In the standard ILC method, the covariance matrix is calculated using the entire sky.

In practice, it is difficult to model all of the different foreground noise components. Without adequate models for all components, there will be inevitable contamination, and this is one of the shortcomings of the standard ILC method. This motivated the work to construct new ILC methods that could help reduce the effects of contamination, most commonly by localizing the algorithms in harmonic space, pixel space, or both. In this work, we focus on using both harmonic and spatial localizations through the application of spherical needlets.

3.4.3 Needlet Analysis

A popular technique used to reduce the effects of contamination is the NILC method. Historically, NILC algorithms have been used to extract the CMB as well as the SZ effect (Delabrouille et al. 2009, Remazeilles et al. 2011, Hurier et al. 2013, Remazeilles et al. 2013, Planck Collaboration et al. 2016b). The basic idea of the NILC algorithms is to first filter the all-sky maps in harmonic space and then perform the SZ extraction using spatially localized regions. The key advantages of the NILC method are: (1) allowing one to combine intensity maps of different resolutions and from different instruments (2) reducing the noise properties over various angular scales. Below we describe the properties of the needlets used in this work and also lay out the steps for the NILC algorithm.

For the NILC method, one must define the shapes for a set of multipole filters along with a local extraction region to calculate the covariance in Equation 3.4. The covariance between 2 difference maps (a and b) is given by

$$\widehat{\mathbf{R}}_{ab}^{(j)}(p) = \frac{1}{N_p} \sum_{p' \in \mathcal{D}_p} x_a^{(j)}(p') x_b^{(j)}(p') w^{(j)}(d) \tag{3.5}$$

where N_p is the number of needlet modes for a given harmonic scale, j, $\mathcal{D}_p$ is the pixel domain used to compute the covariance, and w is Gaussian weighting that depends on the angular separation between pixels, d. Notably, the covariance was calculated on the data themselves. This is important as there exists random correlations between the SZ signal and the local contamination. Minimizing the local variance with Equation 3.4 inevitably suppresses the SZ signal—an effect known as the ILC bias (Delabrouille et al. 2009, Remazeilles et al. 2013).

The ILC bias is regulated by N_p as a result of the multipole window function and pixel domain, where a smaller value of N_p produces a larger bias. Moreover, N_p also determines the residual variance, yielding less uncertainty in the y-map for a smaller N_p. Thus, there is a trade-off between lowering the bias and raising the variance (or vice versa) that is specific to each set of needlets. This quantity, however, was not stated explicitly by Planck Collaboration et al. (2016b), and this prevented us from investigating the amount of bias in PR2NILC. In subsection 3.5.4 we estimate the bias for our set of needlets and show the correction is small ($\lesssim 5\%$) for the sample of galaxy groups.

Here we explicitly state the shapes and sizes of the needlets used in our algorithm. The shapes of the needlets consisted of 7 Gaussian beam window functions (indexed by j) in harmonic space, $h^{(j)}$. Each window was characterized by the Gaussian FWHMs: 10, 15, 30, 60, 90, 180, 300, and 600 arcminutes. We subtracted the subsequent Gaussian functions to obtain the windows: $10'$-$15'$, $15'$-$30'$, $30'$-$60'$ etc... They are presented as a function of the

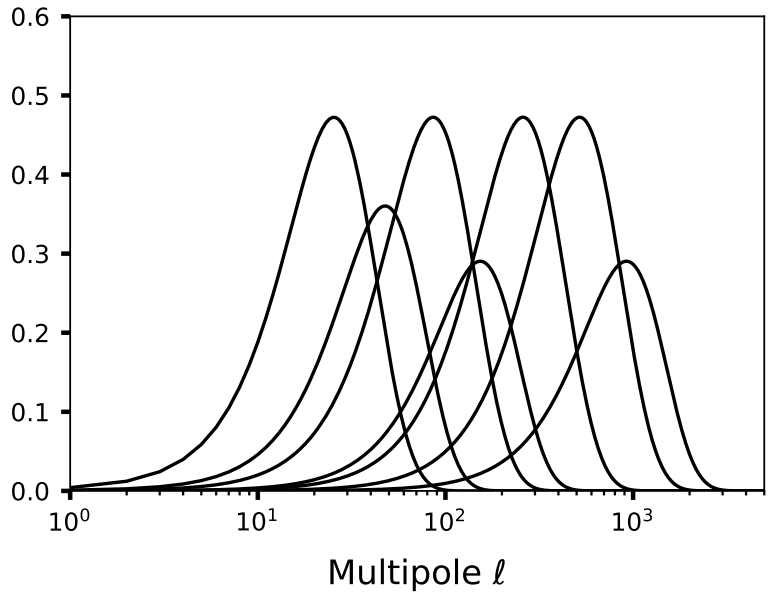


Figure 3.2 Needlet window functions used to filter the difference maps in multipole space. These filters captured features on scales $\gtrsim 10^{'}$ and $\lesssim 10^{o}$

.

multipole moment, ℓ, in Figure 3.2.

We spatially localized the SZ extraction for a single pixel using the information from surrounding pixels. This included setting the σ of the Gaussian weights in Equation 3.5 to be $10\times$ the upper bound of each window function called $\mathrm{FWHM_{up}}$. The surrounding pixel domain was defined out to a radius of $30 \times \mathrm{FWHM_{up}}$. Using the $10^{'}$-$15^{'}$ window as an example, $\mathrm{FWHM_{up}} = 15^{'}$ and the width of the Gaussian used for the weights was $\sigma = 10 \times \mathrm{FWHM_{up}} = 150^{'}$.

Now we describe the NILC procedure which closely followed the discussions in Delabrouille et al. (2009) and Remazeilles et al. (2013) to which we refer the reader to for more detailed information. Specifically, this follows the *analysis* and *synthesis* steps laid out by Delabrouille et al. (2009; and references therein).

- First, we performed the spherical harmonic transformation on each of the internal difference maps. Then we applied the first half of the window function ($\sqrt{h^{(j)}}$) to filter the Fourier coefficients in multipole space. Due to the different instrumental resolutions between the frequency maps, only some of the difference maps were considered for each window function. It was required that the instrumental resolution of the lowest frequency used in the difference map was less (better) than $\mathrm{FWHM_{up}}$. As an example, consider the $15^{'}$-$30^{'}$ window function. For this window, the lowest frequency used in

the difference maps had a resolution that was better than $30'$ in order to be included in the extraction. The lowest frequency difference map used for *Planck* data was the 44-70 GHz difference map (FWHM = $28.09'$ and $13.08'$ respectively; Planck Collaboration et al. 2014b). Moreover, the 30-44 GHz difference map was not included since the resolution of the 30 GHz map (FWHM = $33.16'$; Planck Collaboration et al. 2014b) was worse than $30'$.

- Next we performed the ILC component separation using Equation 3.4 on the filtered maps. An intermediate SZ map was obtained after adding all maps of different scales together.

- The last step was to perform the spherical harmonic transformation on the intermediate SZ map and apply the second half of the window functions in harmonic space. Applying the inverse transform of these filtered Fourier coefficients yielding the final y-map.

3.5 SZ Extraction of Galaxy Groups

In this section, we describe our procedure to extract the SZ signal from different y-maps. First, we explain how we identified and excluded strong sources of contamination. Second, we describe our estimations of the uncertainty in localized fields. Third, we present two methods for stacking the galaxy groups together. Finally, we estimate and correct for the bias with Monte Carlo simulations.

3.5.1 Contamination

3.5.1.1 Small-Scale

Background fluctuations in the y-maps occurred both in the positive and negative directions. The power spectrum at large multipole moments (small angular scales) was dominated by galaxy clusters (positive), infrared (IR) sources (positive), and radio sources (negative). We investigated the effects of radio and IR sources using those identified in the second Planck Catalogue of Compact Sources (PCCS; Planck Collaboration et al. 2016e).

The analysis of radio and IR sources started by generating $20' \times 20'$ pixel images of PR2NILC data. Each image contained a field-of-view $15^\circ \times 15^\circ$ and was centered around the objects in Table 3.1. Next, we smoothed the maps using a 2D Gaussian filter with a FWHM = 5° and subtracted them from the raw maps in attempt to remove large-scale fluctuations. Passing the maps through this high-pass filter allowed us to analyze the amount of small-scale contamination. Specifically, we focused on the pixels within the upper/lower 1% in each

field. Throughout this analysis, we excluded pixels associated with known galaxy clusters identified in the MCXC (Piffaretti et al. 2011) and PSZ2 (Planck Collaboration et al. 2016a) catalogs since they produced strong positive signals.

The extreme negative pixels (lower 1%) were most associated with PCCS sources in the 143 GHz channel. About 25% of the extreme negative pixels were near a radio source detected in the 143 GHz band, with fluxes typically above 460 mJy. The extreme positive pixels (upper 1%), however, were not as strongly correlated with the IR sources; only $\approx$ 5% of the extreme positive pixels shared positions with 857 GHz PCCS sources with fluxes above 1130 mJy. This was not surprising given the weak SZ spectral dependence at high frequencies, hence, IR sources did not severely propagate into the y-maps.

While radio and IR sources account for some of the extreme positive and negative residuals, they did not account for the majority of the extreme valued pixels. The y-map pixel distributions possessed long-tailed wings, especially in the negative direction, and most of them were not identified as radio sources. Instead, these extreme regions were likely artificial features introduced by the NILC method. We considered these regions to be a source of contamination, so we excluded such regions out to a radius of $20^{'}$ as an effort to produce a flatter background. The same exclusion procedure was applied to the radio/IR sources above the 460/1130 mJy threshold described above.

3.5.1.2 Large-Scale

As previously mentioned, the variance in the final y-maps depended on the chosen set of needlets. They controlled how much large-scale contamination, which was mainly dominated by Galactic dust emission, propagated into the final y-maps. We analyzed the large-scale variations in the y-maps using the two-point angular correlation function

$$\xi(\theta) = \langle \rho(\theta + \delta\theta) \rangle \tag{3.6}$$

which is the mean correlation within angular bins of size $\theta + \delta\theta$. The correlation between coordinates i and j is given by

$$\rho(X_i, Y_j) = \frac{(X_i - \mu_X)(Y_j - \mu_Y)}{\sigma_X \sigma_Y} \tag{3.7}$$

where X and Y are two maps of the sky, μ and σ represents their means and standard deviations respectively. The two-point correlation function was measured for each all-sky y-map after applying a set of masks, including the 40% sky coverage galactic mask and the point source mask from Planck Collaboration et al. (2016b). We also excluded known

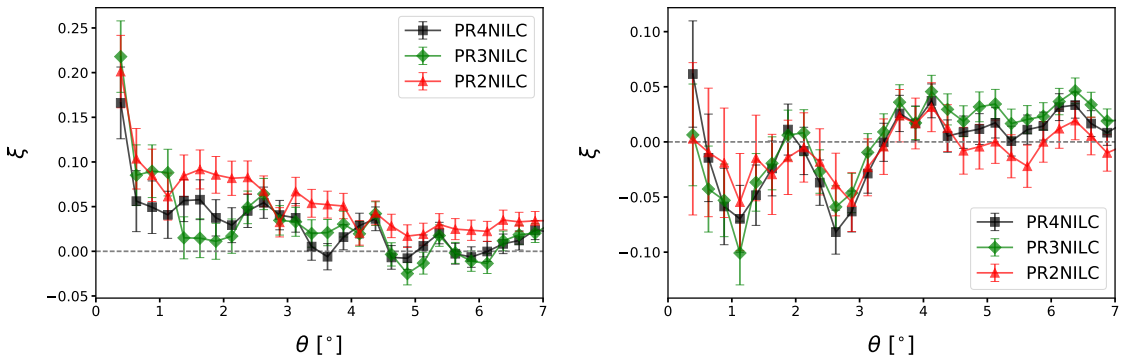


Figure 3.3 (*left panel*) SZ two-point angular autocorrelation profiles for different y-maps binned by $\frac{1}{4}^\circ$ increments with the first bin omitted. Sources of contamination such as the galactic plane, galaxy clusters, and point sources, were masked for this calculation. Uncertainties were determined in a Monte Carlo manner. PR2NILC showed the strongest background correlations on most angular scales while PR3NILC and PR4NILC appeared similar beyond 2°. (*right panel*) Same as the top but represents the angular cross-correlation between the y-maps and the 857 GHz map which was used as a proxy for the dust emission. Once can see strong anti-correlations on scales $\sim 1^\circ$ and 3°.

clusters from the MCXC and PSZ2 catalogs. The reason for applying these masks was to help isolate the general background from small-scale contamination.

The two-point angular autocorrelations of the different y-maps are shown in the top panel of Figure 3.3 where one can see significant correlations on various angular scales for all y-maps. Most of the correlation power was suppressed beyond $30'$ (coinciding with the PSF), but significant correlations still existed on larger scales. The apparent peaks and valleys in the correlation functions were likely attributed to the differences in the *Planck* data reduction as well as the different NILC methods employed. Furthermore, the PR2NILC profile showed stronger correlations compared to PR3NILC and PR4NILC on nearly all angular scales. Since PR2NILC used different data and window functions compared to PR3NILC and PR4NILC, it was not clear which factor was most responsible for producing the larger correlations. On the other hand, PR3NILC and PR4NILC used identical window functions so the differences in their correlations were purely attributed to the differences in the *Planck* data processing.

On scales $\lesssim 1^\circ$, the correlations in PR3NILC were slightly larger than PR4NILC, but the two profiles became consistent $\gtrsim 2^\circ$. The observed differences on small scales could be attributed to the different destriping baselines used in cleaning the PR4 and PR3 time-ordered data (see section 3.7).

The bottom panel of Figure 3.3 shows the cross-correlation between the y-maps and the 857 GHz map, which was used as a proxy for the dust emission. One can see strong anti-

correlations between the y-maps and the dust near 1° and 3° for all y-maps considered. These correlations induced background fluctuations that could affect the extraction of SZ signals. In order to account for strong effects from the dust in our SZ extraction, we excluded regions where the y-maps were highly correlated with the 857 GHz map. These regions were identified by first calculating correlation maps i.e., multiplying the scaled versions (unit variance and zero mean) of the y-maps and 857 GHz maps. Next, we smoothed the correlation maps by a 2D Gaussian kernel with FWHM $= 1/2^\circ$ as a low-pass filter. Finally, regions bounded by 2σ contours were identified as strong dust contamination and excluded in the profile extraction.

We conclude our discussion of contamination by noting that the stacked SZ profile (see section 3.6) remained remarkably unchanged even when these sources of contamination were not excluded. This was reassurance that our final stacked profile was not at the mercy of unidentified contaminants.

3.5.2 Uncertainty

The noise levels in the y-maps varied across the sky. Here we describe the procedure for evaluating the local background fluctuations around individual objects.

First, we created square images centered on each object in Table 3.1 and made them 20 $R_{500} \times 20$ R_{500} in size. Then a grid of 36 annuli was placed onto each field, each spaced by 0.25 R_{500} and extending out to 5 R_{500}. They were arranged into a square grid such that the bins inside R_{500} from one annulus did not intersect with the same bins of adjacent annuli. Second, we removed sources of contamination and calculated the mean value of each bin. Third, the mean value of the combined outer 4-5 R_{500} bins was subtracted from the inner annuli as a correction for the local background; this was based on the assumption that the SZ flux beyond 4 R_{500} was negligible. Fourth, we compared alike bins (i.e., those covering the same radial range) only if $> 80\%$ of their areas were unaffected by the contamination removal. Finally, the uncertainty was characterized for each field by plotting the relation between the standard deviation of alike bins as a function of annulus area. These data were modeled as a power law, allowing the slope and normalization to vary as free parameters. One would expect the uncertainty for a Gaussian-like background to scale as $A^{-0.5}$ with, A, being the uncontaminated area in an annulus; instead, we found slopes closer to ~ 0.4.

3.5.3 Stacking Methods

The SZ radial surface brightness profiles were extracted using circular annuli centered on the positions labeled in Table 3.1. The annuli were scaled to R_{500} and separated by a bin

width of 0.25 R_{500}, extending out to 5 R_{500} (similar to the uncertainty analysis). Again, the bins from 4-5 R_{500} were used to determine the local background. Their mean value was subtracted from the rest of the inner bins as a local offset correction. The uncertainty on the local offset was propagated through the stack using the error on this mean value. In addition, the innermost regions were masked by a circle with a $20^{'}$ radius to avoid expected contamination coming from the member galaxies in each group.

The surface brightness profiles were stacked by: (1) calculating the weighted average (2) taking the median and bootstrapping to estimate uncertainties. In the first method, bins were weighted by the amount of available area. Since all of the annuli were scaled to R_{500}, the most massive and nearby (i.e., most resolved) objects possessed the lowest error bars. This allowed some objects to carry more weight in the stack. For example, if the area of a bin for one object was twice as large as that of another object, then the uncertainty for the first object would be smaller by roughly a factor of $\sqrt{2}$. On the other hand, the bootstrapping method assigned equal weights to all objects. In subsubsection 3.5.4.2, we show with Monte Carlo simulations that weighted averaging and bootstrapping yielded similar results. Moving forward, however, most of the discussion will consider the results from the bootstrap method. The uncertainties in bootstrapping were $\sim 30\%$ larger than those in the weighted average estimate, so we adopted the larger uncertainties as a conservative measure. We provide the results of the weighted average stacked profile in subsection 3.9.2. In addition, we tested two sub-samples to reveal any differences/similarities between the 2 most massive and 8 least massive systems.

3.5.4 Bias

The NILC method should suppress the SZ signal due to the well-known ILC bias (Delabrouille et al. 2009). Here we describe how we corrected for biases in our sample through Monte Carlo simulations.

3.5.4.1 Model Profiles

The SZ surface brightness (y) at some projected radius, r, is proportional to the pressure integral along a line-of-sight such that

$$y(r) = \frac{\sigma_{\rm T}}{m_{\rm e}c^2} \int_r^{R_{\rm max}} \frac{2P(r')r'}{\sqrt{r'^2 - r^2}} dr' \tag{3.8}$$

where r' is the physical radius, $P(r')$ is the pressure at r' assuming spherical symmetry, $\sigma_{\rm T}$ is the Thomson cross section, $m_{\rm e}c^2$ is the rest-mass energy of an electron, and $R_{\rm max}$ is the

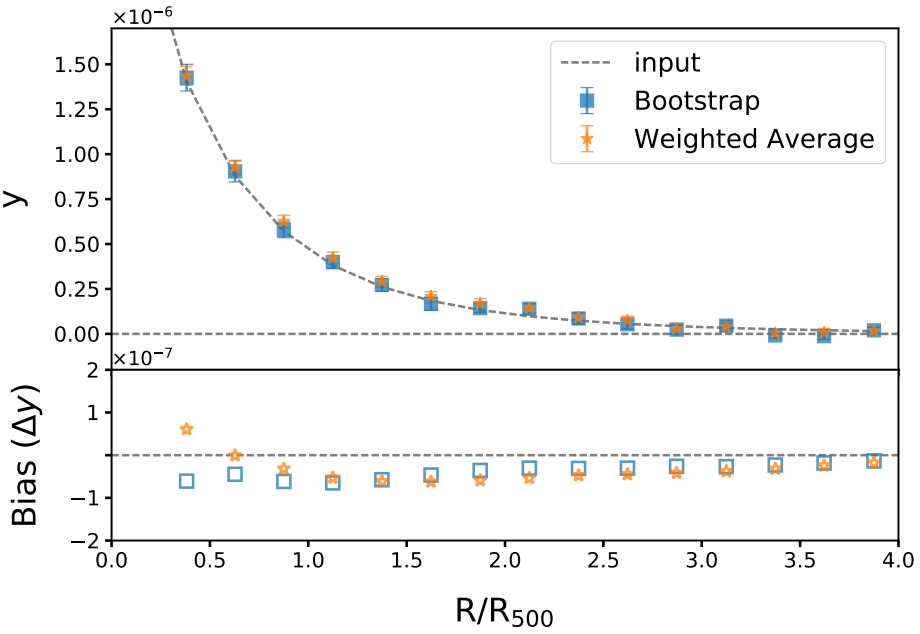


Figure 3.4 Results of stacking 100 simulated galaxy group profiles that were injected into the *Planck* and *WMAP* frequency maps, and recovered in the PR4NILC maps. (*top panel*) The blue squares represent the recovered stacked profile using the bootstrap method, and the orange stars were calculated with a weighted average. Strong sources of contamination were removed before each extraction, and bias corrections were applied from the bottom panel. The dotted line denoted the input signal defined to be the median of all AGN 8.0 profiles from L15, each convolved with the PSF. (*bottom panel*) The open markers are the estimated bias values calculated from "refined" SZ profiles. They represent the simulated profiles after subtracting off the real SZ portion covering the same region, leaving behind a contamination-free signal. Refined profiles quantified the amount of bias introduced by our NILC algorithm and stacking procedures, which was $\lesssim 5\%$.

maximum radius of a halo which we set to 4 R_{500} .

A common way to model the radial pressure profiles of groups and clusters is with a generalized Navarro Frenk and White (GNFW) model (Nagai et al. 2007)

$$\frac{P(r)}{P_{500}} = \frac{P_0}{x^{\gamma}(1+x^{\alpha})^{\frac{\beta-\gamma}{\alpha}}} \tag{3.9}$$

where $x = \frac{c_{500}r}{R_{500}}$. The model is characterized by five parameters: P_0 is the normalization; c_{500} is a concentration parameter; γ, α, and β describe the slopes near the central, middle, and outer regions ($r << \frac{R_{500}}{c_{500}}$, $r \sim \frac{R_{500}}{c_{500}}$, and $r >> \frac{R_{500}}{c_{500}}$) respectively. Many of these parameters have been constrained through observations of massive clusters provided by the seminal works of Arnaud et al. (2010; hereafter A10) and Planck Collaboration et al. (2013a).

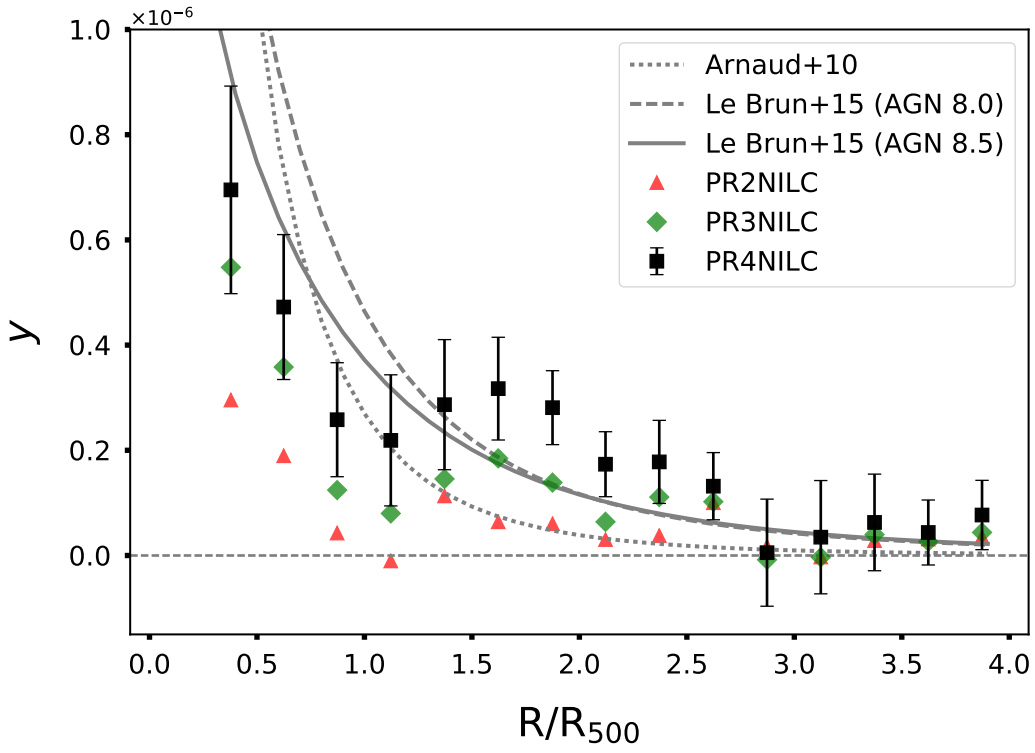


Figure 3.5 The stacked sample of galaxy groups using three different y-maps. PR2NILC (red triangles) represents on of the public y-maps while PR3NILC (green diamonds) and PR4NILC (black squares) represent the extractions from our own NILC extraction using later versions of *Planck* data with the addition of *WMAP* data. The stacked values and their uncertainties were calculated using the bootstrap method. Uncertainties are shown only for PR4NILC for clarity, but the errors for the other profiles are similar. Bias corrections were applied to PR3NILC and PR4NILC data, but this was not possible for PR2NILC data. The dotted gray line is the predicted profiles from A10, while the dashed and solid lines are two different AGN feedback models from L15.

Observational data near the cluster outskirts, however, are generally too poor to fit for the outer slope; thus β is oftentimes fixed using results from numerical simulations.

We considered three different GNFW models to describe the stacked SZ profile. First was the predicted profile from A10. This profile was derived from an X-ray sample of galaxy clusters out to R_{500}. One might expect galaxy groups to exhibit this shape if they were simply scaled-down versions of galaxy clusters. The other two models were derived from the simulations of L15 with different AGN feedback prescriptions, i.e., AGN 8.0 and AGN 8.5. These feedback prescriptions allowed the central black hole to accrete gas and build energy until it could heat the ambient gas by a pre-defined quantity, $\Delta T_{\rm heat}$. This value was set to 10^8 K and $10^{8.5}$ K for the AGN 8.0 and AGN 8.5 models respectively. Once the appropriate amount of energy was gained by the black hole, then 1.5% of the rest-mass energy of the

accreted gas was released as feedback. Since the AGN 8.5 prescription required more gas to be accreted before feedback could take place, it resulted in more bursty outflows relative to the AGN 8.0 model.

3.5.4.2 Monte Carlo Simulations

In order to understand the biases in our sample, we injected 100 simulated objects into the PR4, and *WMAP* frequency maps. The simulated sample was drawn from the mass and redshift properties from Table 3.1. Each object in the sample was simulated 10 times and injected into 10 random locations on the sky (100 total) at galactic latitudes $|b| > 15°$. We adopted the AGN 8.0 model from L15 as the fiducial model for the simulated SZ profiles (we refer to this as the "fiducial model" herein). The fiducial model for each object was added into the frequency maps using Equation 3.1 after convolving the signals with the PSF (assumed to be a 2D Gaussian with a FWHM equal to the instrumental resolution).

The bias was calculated by subtracting the real y-map (i.e., PR4NILC with no injected sources) from the simulated y-map. This resulted in a "refined" y-map that was free of contamination. The refined profiles were recovered in the same way as the real groups, i.e., annuli bins were separated by 0.25 R_{500} , the outer annuli from 4-5 R_{500} were subtracted from each field to correct for local background offsets, and the central $20^{'}$ regions were excluded. One can then measure the bias by comparing the refined profile with the true input. The true input was considered to be the median of all fiducial profiles generated for each object convolved by the PSF. The difference between the refined signal and the input values are shown in the bottom panel of Figure 3.4.

The bias profiles were slightly different among extraction methods. Most notably, the inner bins contained positive bias in the weighted average method while it was entirely negative for the bootstrap technique. While one would expect the ILC bias to always be negative, the positive bias in the weighted average was attributed to the unequal contributions from the most resolved objects. Indeed, the two most massive objects in the sample happened to be the most extended on the sky. Therefore, their estimated errors were lower and more weight was given to them in the stack (see subsection 3.5.2). Conversely, the bootstrap method assumed equal weighting for each object.

In the top panels of Figure 3.4 we show the recovered simulated profiles using our extraction method. These were different than the refined profiles because they were corrected for the bias and also susceptible to residual contamination. This experiment demonstrated our ability to recover the stack of SZ profiles. Specifically, we measured the reduced χ^2 ($\chi^2_{\rm red}$) = 0.78 (1.03) for the bootstrap (weighted average) stack for 15 degrees of freedom (DOF).

3.6 Results

This section compares different model predictions with the stacked surface brightness and cumulative profiles. First we compare the data and models at face-value, and then we perform a least-squares fit.

3.6.1 Surface Brightness Profile

The stacked (bootstrapped) signal of galaxy groups from different y-maps is shown in Figure 3.5 along with three different GNFW model predictions for our sample. (The individual profiles are provided in Figure 3.9 in the appendix.) At face value, none of the model predictions appeared consistent with the stacked profiles from PR2NILC and PR3NILC. The profile from PR4NILC, however, was measured using better data, and this was in agreement with the the AGN 8.5 model prediction; the $\chi^2_{\rm red}$ value using the bootstrap (weighted average) method was 1.23 (1.15) for 15 DOF.

Next, we fit each data set using the three model profiles described above, specifically fixing their shapes and allowing the normalizations to vary as free parameters. The best-fit normalizations using PR2NILC yielded values 18%-25% of the original models; those for PR3NILC data (bias corrected) were 41%-57%; and PR4NILC (bias corrected) returned 60%-92%. The AGN 8.5 profile fit (the flattest of the three models) to PR4NILC data yielded the largest normalization of 92% with respect to the original prediction. It also gave the lowest $\chi^2_{\rm red}$ value of 1.28 (14 DOF) compared to the other model fits.

Out of curiosity, we also extracted the stacked signal from the public MILCA y-map (Planck Collaboration et al. 2016b) and found it was nearly identical to that from PR2NILC. This result suggests the PR2 data processing could be suppressing the SZ signal and, in some cases, this may be even more important than the chosen ILC method. (See subsection 3.7.1 for the discussion on different data release versions.) We do not further report on the MILCA y-map and focus on only the NILC method.

3.6.2 Extended SZ Profile

The stacked SZ profile exhibited a "bump" feature around 1-3 R_{500} as seen in Figure 3.5. This feature appeared both in the weighted average and the bootstrap stacks, so the feature was not due to the stacking procedure. In addition, the feature was not dominated by a few objects as the median and mean stacking yielded similar results. The significance of the bump was determined by fitting the fiducial model to the data but excluding those within the arbitrary region of 1.25-3 R_{500}. This was done both for the simulated and real data sets.

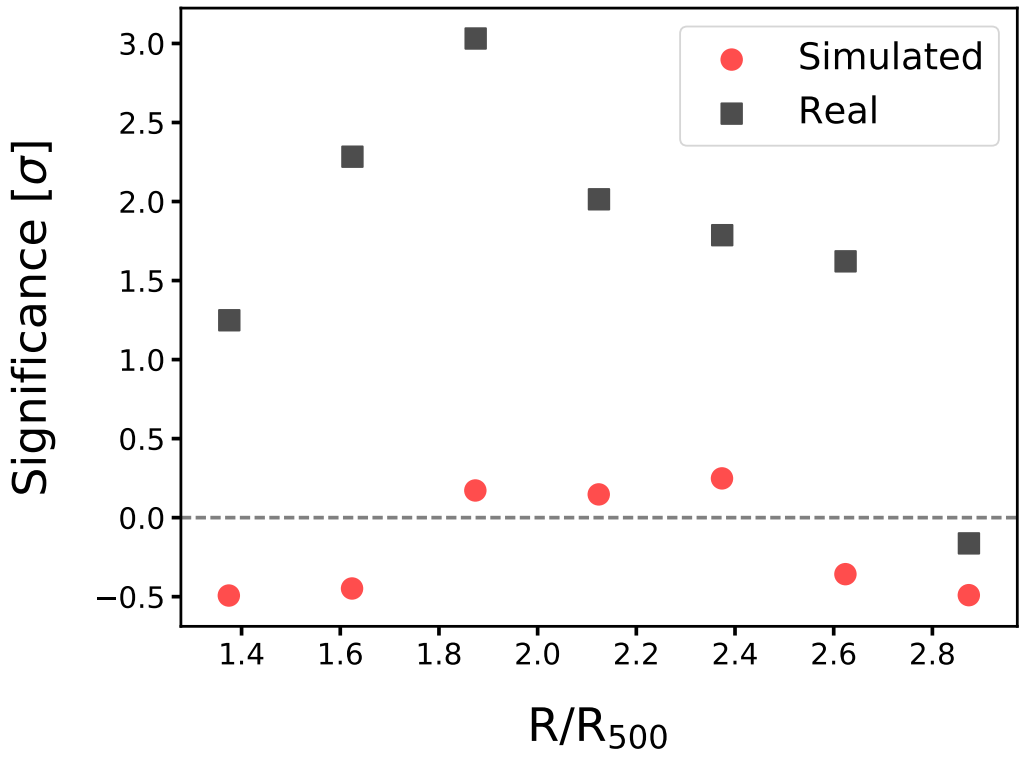


Figure 3.6 Significance profiles when trying to measure a bump feature both in the simulated and real data sets. First, AGN 8.0 profiles were fit to the data outside of the bump region (1.3 - 2.9 R_{500}). Then residuals were calculated between the best-fit model and the data over the bump region. The significance was calculated by simply dividing each residual by the uncertainty of the measurements.

The residuals between the best-fit model and the data in the bump region are shown in Figure 3.6. There were $> 2\sigma$ deviations between the model and real data around 1.6-2.2 R_{500} , with a peak significance of 3.0σ near 2 R_{500} . We note these calculations were mildly model dependent. Specifically, the maximum significance around 2 R_{500} was 3.0, 3.0, and 2.6 σ when fitting the A10, AGN 8.0, and AGN 8.5 models respectively. On the other hand, the results from the simulated data did not yield significant deviations over the bump region. These results suggested the bump was unlikely an artificial feature from the NILC method.

3.6.3 Cumulative Signal

The cylindrical integrated SZ quantity within a projected radius, r, is given by

$$Y_{\rm cyl}(r) = \sum_{i;r_i<r} 2\pi r_i y(r_i) \Delta r \tag{3.10}$$

where i is the index of each radial bin, y is the SZ signal, and $\Delta r = 0.14$ Mpc (equal to 0.25 $\times$ the median R_{500} of the sample). It measures the product of the gas mass and mass-weighted temperature enclosed within a cylinder along the line-of-sight. At large enough radii $Y_{\rm cyl}$ captures the total SZ flux of the system which is a proxy for the total thermal energy of the halo plasma.

The cumulative $Y_{\rm cyl}$ is shown in Figure 3.7 along with the three different model predictions. None of the models were consistent with the inner parts of the data, however, the cumulative signal converged with the AGN 8.0 prediction from L15 near $\sim 2.5\ R_{500}$. This places a crucial constraint on the amount of thermal energy bound inside galaxy groups that must be matched by numerical simulations.

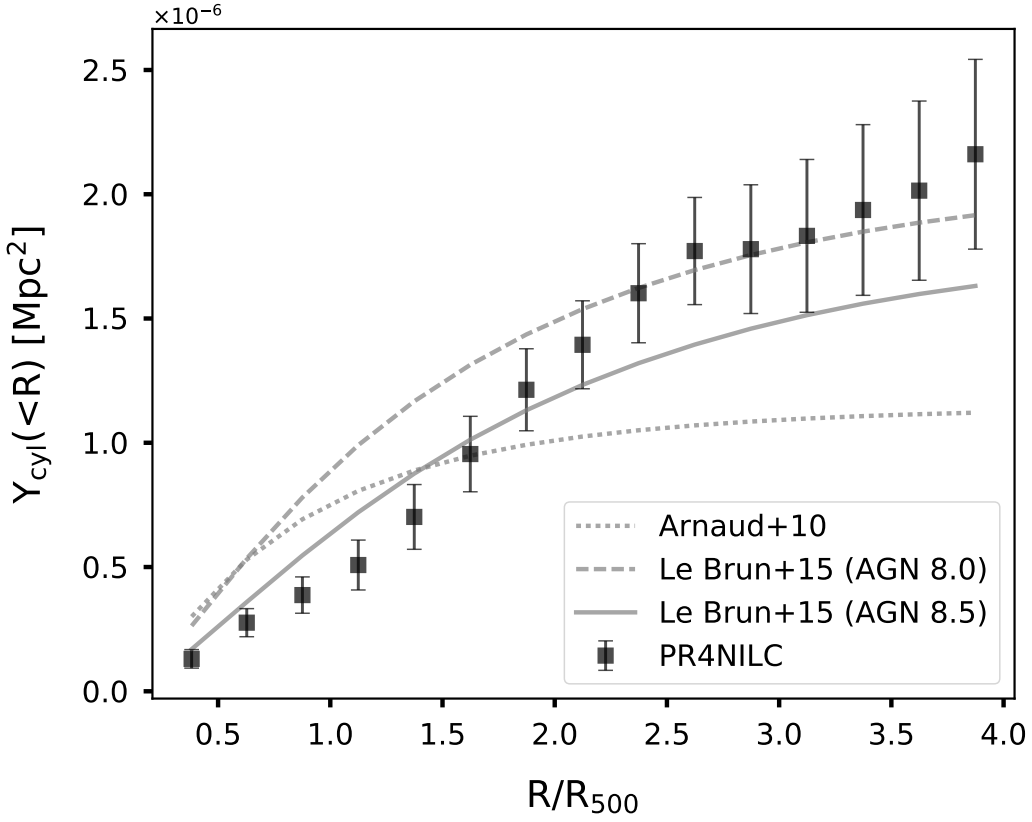


Figure 3.7 Cumulative cylindrically integrated profiles. The black data represent the cumulative $Y_{\rm cyl}$ for the PR4NILC data while the different lines denote the three model predictions considered in this study.

3.7 Discussion

This section presents our interpretation of the results. We start by discussing the discrepancies among different y-maps. Then we estimate the baryon fraction and compare our value with previous studies. Finally, we discuss the nature of the extended SZ profile.

3.7.1 Data Release Versions

In Figure 3.5 one can see the signal from PR3NILC appeared larger than PR2NILC for radii $\lesssim 2.5\ R_{500}$. At the same time, the signal from PR4NILC superseded that of PR3NILC. This last statement points to the differences in the data processing between PR3 and PR4 data.

While there were many improvements from PR3 to PR4, the best explanation for the observed differences was due to the effects of "striping". Turning time-ordered data from multiple scans of the sky can introduce residuals along the scanning pattern of the satellite. Thermal instabilities, far sidelobes, and elliptical beam shapes are known to produce stripes in the all-sky frequency maps. Multiple algorithms have been developed to reduce these features (Poutanen et al. 2004, Keihänen et al. 2004) and have made major improvements in recent years.

The PR4 destriping technique used a baseline of 167 ms which was much shorter than the baselines used on PR3 data (Planck Collaboration et al. 2020c). The PR4 baseline corresponded to roughly 1° on the sky, which may be why the PR4NILC correlation function was smaller on sub-degree scales relative to PR3NILC. It may also be why the SZ profile from PR3NILC appeared suppressed relative to PR4NILC in Figure 3.5. The difference map between PR4NILC and PR3NILC is shown in Figure 3.8, serving as a visualization of the striping features.

3.7.2 Baryon Fraction

We calculated the amount of hot gas in the halo using the best-fit pressure profiles to all of SZ data (bump region included). The SZ effect measures the pressure of the electrons $P_{\rm e}(r) = n_{\rm e}(r) k_{\rm B} T_{\rm e}(r)$ where $n_{\rm e}$ is the number density of electrons. We solved for $n_{\rm e}(r)$ using our best-fit pressure profile (AGN 8.5 model) to the SZ data and assuming an exponentially decaying temperature profile from Sun et al. (2009). Furthermore, we used their $M_{500} - T_{500}$ relation and result of $\frac{T_{500}}{T_{2500}} = 0.89$ and adopted a metallicity of $Z = 0.3\ Z_{\odot}$ to derive the gas mass density $\rho_{\rm gas}(r)$. Integrating this quantity out to R_{500} yielded $f_{\rm gas,500} = 0.038 \pm 0.007$, that is the gas mass fraction relative to the total mass within R_{500}.

The baryon fraction within R_{500}, $f_{\rm b,500}$, was calculated by adding the stellar mass to the

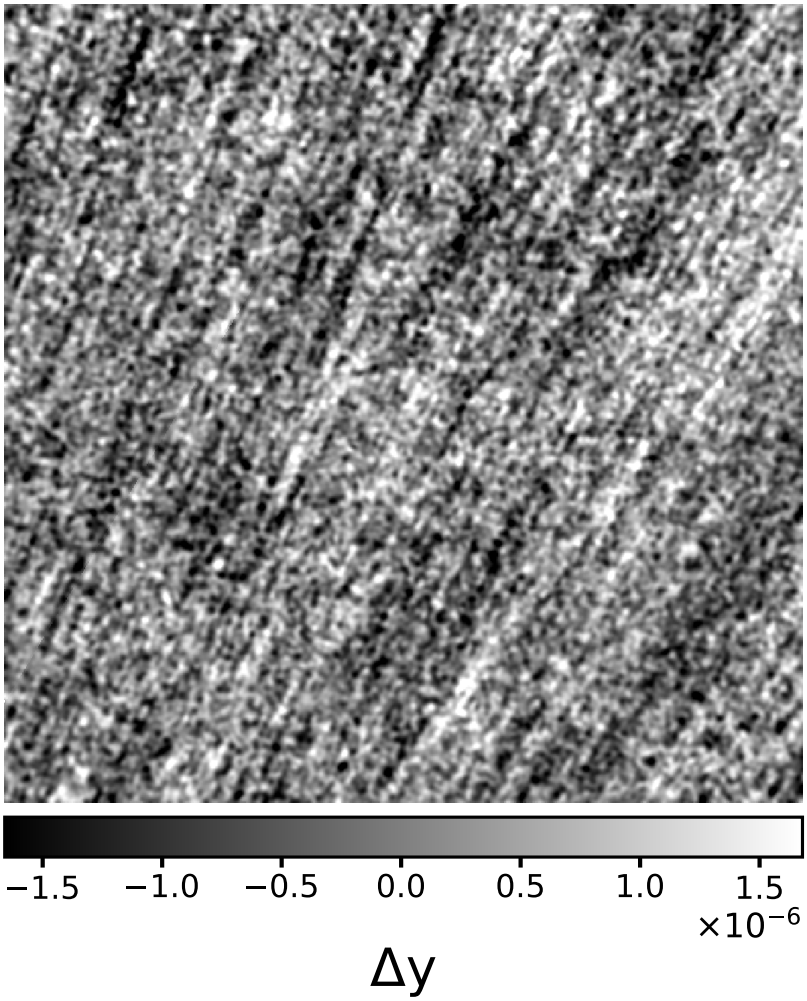


Figure 3.8 A randomly selected patch showing the difference between PR4NILC and PR3NILC. The region is centered at the coordinates ($l = 161.431°$, $b = 84.516°$) with a field-of-view $22° \times 22°$. There are clear striping features that coincide with the *Planck* scanning pattern. Since the NILC method was the same for PR3NILC and PR4NILC, the difference in the y-maps is purely due to data processing.

gas mass. The stellar mass was estimated using the K_s luminosity presented in the KT17 catalog and assuming a mass-to-light ratio ~ 0.8 in solar units (Bell et al. 2003). The stellar mass fraction within R_{500} was $f_{*,500} \approx 0.018$, yielding a baryon fraction of $f_{\rm b,500} \approx 0.056$, which is much smaller than the cosmic value of 0.16 (Planck Collaboration et al. 2020b).

Additional systematic uncertainties are expected when assuming a pressure profile. In fact, all of the stacked data within R_{500} appeared to lie systematically below the best-fit profiles, while those in the bump region resided above the fit. Thus, it is possible the baryon fraction within R_{500} was overestimated by the best-fit models.

Observational studies have showed $f_{\rm gas,500}$ tends to decrease with decreasing halo mass (Dai et al. 2010, Laganá et al. 2013). For galaxy groups, there is a general consensus that $f_{\rm gas,500}$ is $\lesssim 10\%$. For example, Thölken et al. (2016) measured $f_{\rm gas,500} \approx 9\%$ for the galaxy group UGC 03957 using mosaic images from Suzaku. Similarly, Sarkar et al. (2021) measured $f_{\rm gas,500} \approx 7\%$ using joint Suzaku and Chandra observations of the galaxy group MKW4. These results, along with those presented in this study, suggest galaxy groups possess $f_{\rm b,500} \sim 1/2$ the cosmic value.

Our value of the gas fraction was roughly half compared those reported in the literature. One possible explanation for this discrepancy could be because our sample of galaxy groups was not X-ray selected. X-ray detected groups and clusters tend to be biased toward more virialized systems. While massive galaxy clusters almost always appear relaxed, galaxy groups likely exist in a wide range of dynamical states. Furthermore, it is possible that not all of the gas in galaxy groups has been heated to the virial temperature. If the true temperature of the gas was lower than what was assumed in our models then the inferred gas density would be closer to the estimated baryon fractions determined by X-ray observations.

3.7.3 Bump Feature

Here we consider the possible explanations for an increase in the SZ signal beyond the virial radius. One might argue there should be projection effects from neighboring halos known as the two-halo contribution (Vikram et al. 2017, Hill et al. 2018). This term was calculated as described in Pandey et al. (2019) assuming the L15 pressure profiles. The two-halo contribution was found to be negligible ($y \sim 10^{-8}$ within 4 R_{500}), which was mainly because of the low-redshift nature of the sample. A bump feature may also arise from miscentering during the SZ extraction. We tested this by purposefully misaligning the extraction annuli on the simulated data set, but the results did not show significant increases near the bump region. Another possibility is the bump could be attributed to the anit-correlations between the dust and y-maps near 1°. Rather than describing the feature as an excess of SZ signal near

2.5 R_{500} , one could argue for the presence of a "valley" near 1 R_{500} instead. It is possible the anti-correlations between the y-maps and the dust may have caused a suppressed SZ signal. Nevertheless, we did not see strong evidence for systematic bumps or valleys in the Monte Carlo simulations (subsubsection 3.5.4.2).

One might also wonder if AGN outbursts could sweep gas out to very large radii. In other words, the bump feature seen in these results could be a giant pile-up of material that was expelled by the AGN. Below we give an order-of-magnitude argument as to why this is energetically possible.

In this experiment, we applied a model that could capture the bump feature in the SZ data. This was done by over-fitting the data with a fifth-degree polynomial pressure model. Specifically, we assumed an extrapolated temperature profile from Sun et al. (2009) to get an estimate of $n_{\rm e}$, which was then converted into a gas mass density, $\rho_{\rm gas}$. We then calculated a gas mass reservoir of $\log_{10}(M_{\rm gas}[M_{\odot}]) \approx 13.2$ over the volume covered by the bump region (1.25 - 3 R_{500}). For comparison, the fiducial AGN 8.0 model predicted a gas mass of $\log_{10}(M_{\rm gas}[M_{\odot}]) \approx 13.0$.

Driving a significant amount of gas to large radii changes its binding energy. The binding energy of gas within some physical radius, r, is given by

$$E_{\rm bind} = 4\pi G \int_0^r M(<r')\rho_{gas}(r')r'dr' \tag{3.11}$$

where G is the gravitational constant, $M(<r)$ is the enclosed mass assumed to be dominated by the dark matter. The dark matter density profile was estimated using an NFW profile with a concentration parameter $c_{500} = 3.2$ (e.g., Holland et al. 2015). The two models of the gas densities (fiducial vs. polynomial) returned similar binding energies of the gas $\sim 10^{62}$ ergs at 3 R_{500} . This was not surprising given the results in Figure 3.7. At most, the binding energies differed by a few 10^{61} ergs which is on the order of the mechanical feedback energy from radio galaxies in galaxy groups (Giodini et al. 2010). Thus, it is energetically possible for AGN feedback to cause the bump seen in our data.

In addition, this density profile (polynomial fit) would require galaxy groups to be out of hydrostatic equilibrium near the outskirts. Our order-of-magnitude calculation suggested the gravitational pressure would be $\sim 2\times$ larger compared the thermal gas pressure around 1.5 R_{500} . In fact, this is in agreement with the simulation results from Burns et al. (2010) that showed galaxy clusters are likely not in hydrostatic equilibrium near the outskirts. These authors demonstrated that turbulence and bulk radial motions could contribute half of the total pressure support needed to balance gravity at large distances.

Instead of piling gas at large distances, it is also possible the extended gas was heated

through accretion shocks. Accretion shocks occur when infalling gas encounters extreme changes in density and/or temperature in the gaseous halo. There are two types of accretion shocks: external and internal. External shocks are caused by pristine gas falling onto the halo for the very first time. In general, these are strong shocks with high mach numbers (Ryu et al. 2003) and are believed to occur at distances of several R_{500} in galaxy clusters (Hurier et al. 2019, Zhang et al. 2020, Baxter et al. 2021). On the other hand, internal shocks consist of gas that has already passed through the external shock. They are caused by gas falling onto substructure within the halo, subclump mergers, and supersonic flows inside substructures; they also dissipate more thermal energy than external mergers (Ryu et al. 2003, Pfrommer et al. 2006, Vazza et al. 2009).

Here we present tentative observational evidence of internal shocks in galaxy clusters. At least one SZ study by Adam et al. (2018) has reported evidence of substructure in individual clusters. These authors applied structure filters to their data and were able to detect pressure ridges in some systems out to hundreds of kpc. We also noticed plateau-like features in the SZ profiles reported by the Planck Collaboration. Specifically, there was large residuals from the GNFW model fit around 1-3 R_{500} for a stacked sample of galaxy clusters (Planck Collaboration et al. 2013a). A similar feature was also apparent in the Virgo cluster where the SZ profile flattened outside the virial radius (Planck Collaboration et al. 2016c). The Coma cluster (Planck Collaboration et al. 2013b) also appeared to have an elevated SZ signal beyond R_{500} compared to the A10 prediction. One can also see bump-like deviations in the azimuthal profiles of Abell 2319 by Hurier et al. (2019). It is possible the bump feature seen around 1-3 R_{500} in our stacked sample of galaxy groups is similar to those seen in galaxy clusters. In many of these studies, however, internal accretion shocks were not considered.

Internal shocks are expected to be seen starting near ~ 0.7 Mpc (≈ 1.3 R_{500} for this sample; Ryu et al. 2003) and extending out to the external shock boundary at $\sim$ 5-6 R_{500} (Baxter et al. 2021). It was unlikely for us to detect an external shock since we subtracted off the 4-5 R_{500} regions as local background corrections. The most probable explanation for the bump feature in our stacked data are the manifestations of internal accretion shocks at various radii along a line-of-sight.

3.8 Summary

This work presented the resolved SZ profile for a stacked sample of 10 galaxy groups with a median mass of $\log_{10}(M_{500}[M_{\odot}]) = 13.7$. The stacked signal was extracted using the publicly available y-map as well as our own y-maps constructed from newer versions of *Planck* data with the inclusion of *WMAP* data. For each field, we excluded the strongest sources of

contamination to obtain the most accurate measurements. These signals were stacked using a weighted average and bootstrap method, both of which produced consistent results. Finally, we demonstrated our ability to accurately recover a stacked sample of galaxy groups in our own y-maps through Monte Carlo simulations. The main conclusions from our study are:

- There have been significant improvements to the *Planck* channel maps in recent years. We utilized the latest and best version of *Planck* data to construct a superior y-map, PR4NILC, compared to the public y-map, P2NILC. The PR4NILC data yielded a significant SZ detection out to $\sim 3\ R_{500}$ and was in agreement with the AGN 8.5 model prediction from L15. Conversely, the PR2NILC data did not show a convincing signal beyond R_{500} and did not agree with any of the model predictions considered.

- We estimated a gas fraction of $f_{gas,500} = 0.038 \pm 0.007$ and a baryon fraction $f_{b,500} \approx 0.056$ using our best-fit pressure model and assuming a temperature profile for galaxy groups (Sun et al. 2009). This was slightly smaller than the values reported by X-ray studies of individual galaxy groups. Since our sample was not X-ray selected, these groups may not have yet heated their baryons to the virial temperature. Our estimated baryon fraction was $\lesssim 1/2$ of the predicted cosmic value (0.16) suggesting AGN feedback could be effective at removing gas from galaxy groups.

- We detected a 3σ bump feature near 2 R_{500} in our stacked SZ profile. This feature was most likely a detection of internal accretion shocks at different radii. We found similar features throughout the literature of galaxy clusters, which further supported this claim.

This work has unveiled key discrepancies in extracting weak SZ signals from different versions of *Planck* data, and this must be addressed in similar future studies. Future SZ experiments, such as CMB-S4, will have the ability to study individual galaxy groups with high resolution and sensitivity and can use our results as a baseline.

We thank Shivam Pandey at the University of Pennsylvania for calculations of the two-halo contribution specific to our sample. We are grateful for support from NASA through the Astrophysics Data Analysis Program, awards AWD012791 and NNX15AM93G. The work is based on observations obtained with *Planck*, http://www.esa.int/Planck, an ESA science mission with instruments and contributions directly funded by ESA Member States, NASA, and Canada. This research made use of the High Energy Astrophysics Science Archive Research Center (HEASARC) and the NASA/IPAC Extragalactic Database (NED), which are supported by NASA.

3.9 Appendix

3.9.1 Individual Surface Brightness Profiles

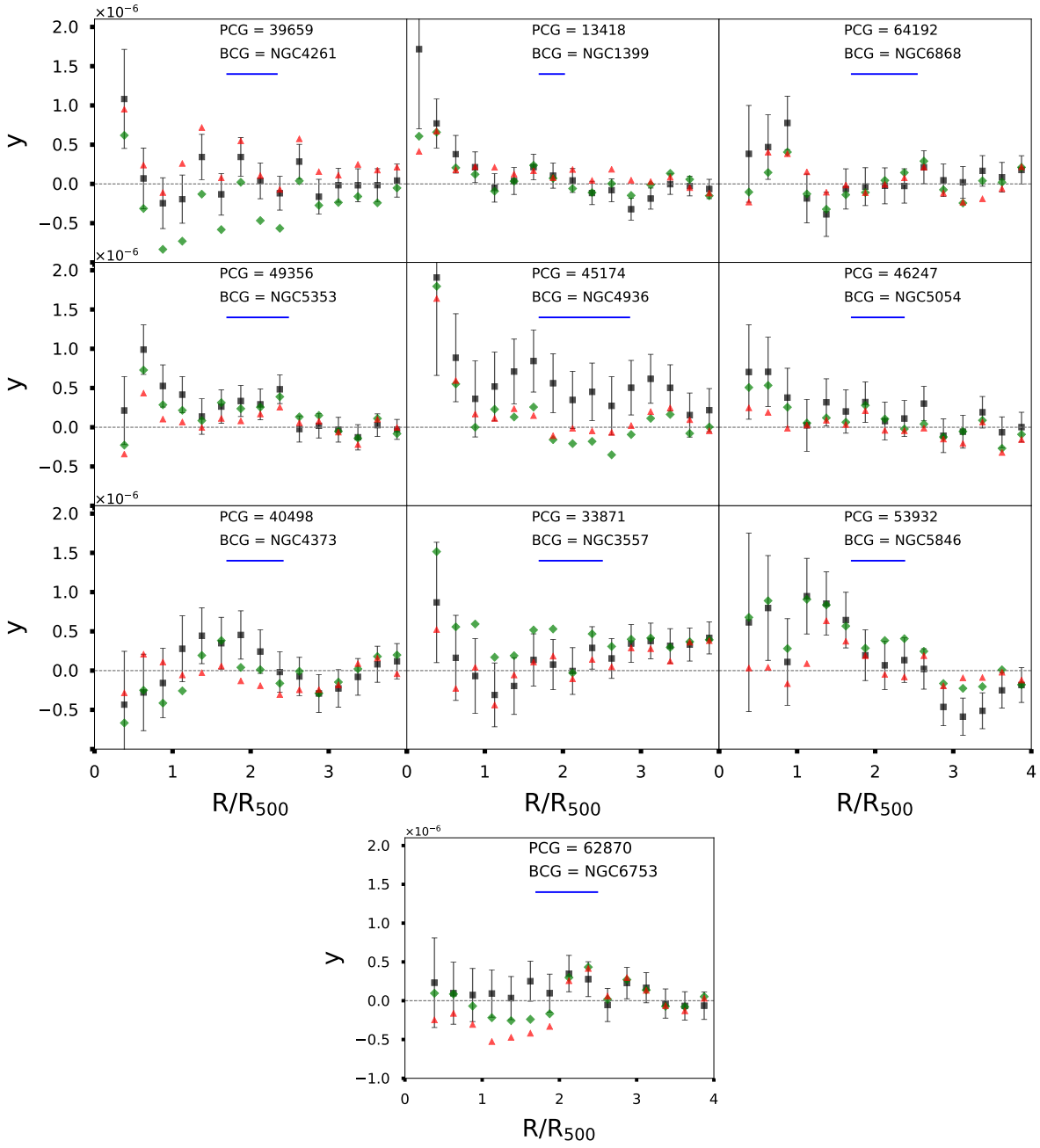


Figure 3.9 Individual SZ surface brightness profiles. Red triangles, green diamonds, and black squares represent the profiles from PR2NILC, PR3NILC, and PR4NILC respectively. Uncertainties are shown only for PR4NILC and were estimated locally depending on the size and location of the extraction annulus (see subsection 3.5.2). The PCG identification represents the objects in Table 3.1; the corresponding BCG IDs are provided as well. Blue lines indicate the 1° scale for each object.

3.9.2 Weighted Average Stacked Profile

Stacking signals together is only acceptable when the spread about the mean is modest, and so one must search for possible for outliers that may be skewing the resulting stack. For the sample in this work, the two most massive systems were the closest in distance. One might expect the combination of their high masses and close distances to yield high S/N values, which could potentially bias the weighted stack. We tested this possibility by splitting our galaxy group sample into low-mass (8 least massive) and high-mass (2 most massive) sub-samples. (We did not consider the bootstrapping method for the sub-samples due to insufficient sample size of the high-mass objects.)

The stacked profile from the full, low-mass, and high-mass samples are shown in Figure 3.10. Tenuous evidence points to a steeper profile for the high-mass sample compared to the low-mass sample within R$<R_{500}$; however, the data were mostly consistent within the uncertainties. In addition, both sub-samples exhibited a bump feature near 1.75 R_{500}, meaning the bump was not dominated by only low- or high-mass systems.

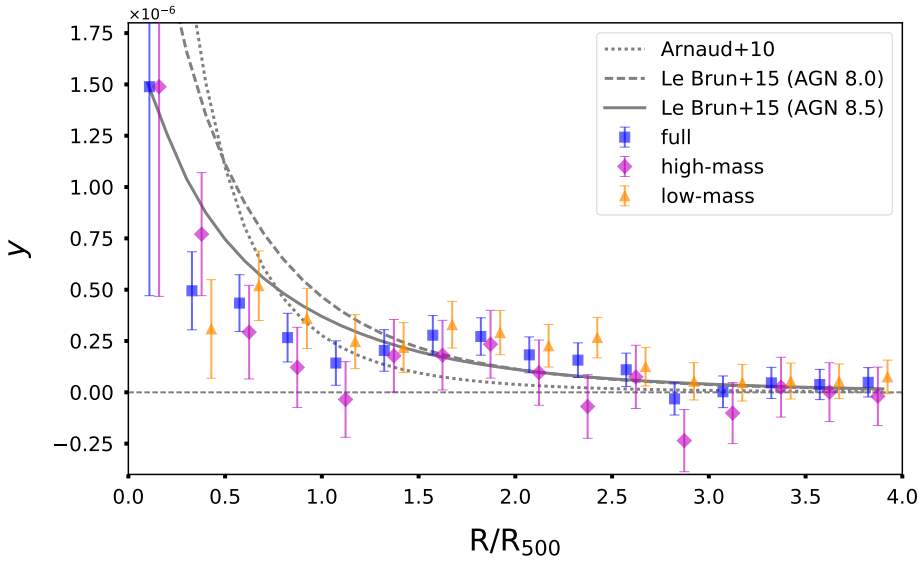


Figure 3.10 Weighted average stacked profiles using the full (blue squares), low-mass (orange triangles), and high-mass (purple diamonds) samples. The data are slightly offset on the horizontal axis for clarity; the blue and orange data are shifted to the left and the right of each purple diamond respectively. The weighted stack was calculated using the empirical variance estimated for each local field. The low-mass sample does not show a value for the innermost bin because it was smaller than the 20' exclusion radius (i.e., 0.25 $R_{500} < 20'$).

CHAPTER 4

Optimizing NILC Extractions of the Thermal Sunyaev–Zel'dovich Effect with Deep Learning

4.1 Abstract

All-sky maps of the thermal Sunyaev–Zel'dovich effect (SZ) tend to suffer from systematic features arising from the component separation techniques used to extract the signal. In this work, we investigate one of these methods known as *needlet internal linear combination* (NILC) and test its performance on simulated data. We show that NILC estimates are strongly affected by the choice of the spatial localization parameter (Γ), which controls a bias-variance trade-off. Typically, NILC extractions assume a fixed value of Γ over the entire sky, but we show there exists an optimal Γ that depends on the SZ signal strength and local contamination properties. Then we calculate the NILC solutions for multiple values of Γ and feed the results into a neural network to predict the SZ signal. This extraction method, which we call *Deep-NILC*, is tested against a set of validation data, including recovered radial profiles of resolved systems. Our main result is that Deep-NILC offers significant improvements over choosing fixed values of Γ.

4.2 Introduction

The hot and diffuse gas that pervades the Universe is most easily observed either from X-ray emission or the thermal Sunyaev–Zel'dovich (SZ) effect. The SZ effect is caused by hot electrons giving an energy boost to cosmic microwave background (CMB) photons through inverse Compton scattering. It has a weaker dependence on the gas density (linear vs. quadratic) compared to X-rays, making it an excellent probe of more diffuse gas.

The *Planck* mission has provided the best data to create all-sky maps of the SZ effect (known as y-maps). In 2016, Planck Collaboration et al. (2016b) released the first publicly available y-maps, nearly a half of a century after it was first theorized (Sunyaev & Zeldovich 1970; 1972). Extracting the SZ signal is no easy feat as the microwave sky is dominated by non-SZ components. Over the past few decades, various component separation techniques have been developed to separate these from the SZ signal.

These public y-maps were constructed using *internal linear combination* (ILC) methods (Delabrouille & Cardoso 2007, Leach et al. 2008). An ILC method is a semi-blind extraction that relies on the spectral dependence of the SZ signal and uses second-order statistics to minimize the reconstruction error (Delabrouille et al. 2009). ILCs also rely on a strong assumption that all non-SZ components are uncorrelated with the SZ effect. Such assumptions are not always valid and, in turn, could lead one to obtain unreliable results. If the non-SZ components are poorly separated, they manifest as systematic residuals that contaminate the reconstructed SZ signal.

In light of this, modified ILC algorithms were developed. Modified ILC methods help improve SZ extractions by using data localization. Data localization introduces additional assumptions about the non-SZ signals before applying ILC. Among the most popular is the algorithm known as *needlet internal linear comibination* (NILC). NILC uses harmonic and spatial localization. It assumes non-SZ components are more similar when grouped by their angular size and location on the sky.

There also exists many other component separation techniques that rely on their own assumptions (many are listed at this website[1]). For example, Bobin et al. (2008) used the assumption of sparsity to perform a semi-blind extraction, known as general morpholocial component analysis (GMCA), of the CMB and SZ signals. While GMCA could outperform a few other extraction techniques, it yielded similar results to NILC. Over the years, refinements have been made to improve its performance (Bobin et al. 2015, Wagner-Carena et al. 2020). One could also do parametric modeling of the components, which has largely been done with the *Commander* algorithm (Eriksen et al. 2008, Galloway et al. 2023). While many more component separation techniques exist, most have only been applied to the CMB. Only recently have there been efforts to improve the quality of all-sky SZ data (e.g., McCarthy & Hill 2024), so there is still plenty of room for investigations.

One modern approach to improving SZ extractions is with deep learning (DL). DL is a subset of machine learning techniques that uses neural networks to build non-linear models. They excel at capturing complex relations between variables in a way that simple, traditional models cannot describe. Over the last decade, DL has been used to tackle challenging tasks,

[1]https://lambda.gsfc.nasa.gov/toolbox/comp_separation.html

and has proven to perform well in various facets of astrophysics including: galaxy morphology classification (Zhu et al. 2019), detection of exoplanets (Shallue & Vanderburg 2018), painting baryons onto dark matter halos in cosmological simulations (Tröster et al. 2019), separating the CMB from foreground contamination (Casas et al. 2022), and building catalogs of SZ clusters (Voskresenskaia et al. 2023). To our knowledge, DL has not been used to extract the SZ effect, and this is one of the chief goals of this paper.

In this work, we present the NILC method and specifically focus on its spatial localization parameter, Γ. Traditional implementations of NILC fix the value of Γ, however, we demonstrate that yields a sub-optimal solution in certain scenarios. Then we present a novel method for extracting the SZ signal which we call *Deep-NILC*. Deep-NILC combines NILC results from different values of Γ, then feeds these values into a neural network to predict the true SZ signal. Our results show that we can achieve better estimations of the SZ signal compared to using fixed values of Γ.

The paper is structured in the following way: in section 4.3 we present the methodology for this study; the main results are presented in section 4.4; the results are discussed in section 4.5; a summary is provided in section 4.6.

4.3 Methods

4.3.1 Simulations

The main data used in this study consisted of simulated observations of the microwave sky. First we describe the set of simulated y-maps obtained from Han et al. (2021) used for training and validation. Then we inject additional SZ sources to better represent the nearby "anomalies" that exist in the real Universe. Finally, we generate realistic mock observations as seen by *Planck* and *WMAP*.

4.3.1.1 SZ Data from Han et al. (2021)

This work required a sizable set of simulated y-maps that resembled the statistical properties of our observed Universe. Usually, a simulated y-map would be acquired from full 3-D cosmological simulations by projecting the electron pressure along a line-of-sight. Unfortunately, running a single simulation can be very computationally expensive, so there are only a few available for public use.

We were able to overcome this obstacle using the work of Han et al. (2021). These authors generated a large set of mock extragalactic signals at millimeter wavelengths based off the cosmological simulations of Sehgal et al. (2010). The simulations from Sehgal et al. (2010)

were designed to match the best observational data available at the time, using cosmological parameters inferred from *WMAP* and gas prescriptions that matched X-ray observations. Han et al. (2021) developed an algorithm, known as *MillimeterDL* (mmDL), to generate many synthetic y-maps using a single simulation from Sehgal et al. (2010).

The mmDL algorithm used a DL method known as Generative Adversarial Networks (GANs). GANs consists of two components: a generator and a discriminator. The generator generates synthetic data while the discriminator's role is to distinguish between real and fake data. Through an iterative process, the generator improves its ability to produce realistic data by fooling the discriminator until the mock data are nearly indistinguishable from the input training data. mmDL was designed to match the power spectra from the Sehgal et al. (2010) simulations, but it was also able to capture important non-Gaussian features. More generally, mmDL was built to take any cosmological simulation as input and generate a large set of corresponding realizations. By feeding a simulation into mmDL as input, Han et al. (2021) created 500 realizations that are publicly available[2].

Their SZ effect was provided at different frequencies which we converted into y-maps using the known frequency dependence of the SZ signal (see Equation 4.2 and Equation 4.3). Furthermore, only ten realizations of the SZ effect were used for our experiments. Seven of these were used for supervised training while three were set aside for validation. In the next section, we augment these data with more examples of resolved signals.

4.3.1.2 Resolved SZ Signals

Most of the strong SZ signals in the Universe are unresolved by *Planck* and *WMAP*. Although, there exists a few extended objects, and these are amongst the most interesting SZ signals to study. For example, the Virgo cluster is somewhat of a statistical anomaly as it produces a strong SZ profile that extends many degrees on the sky. In addition, there are nearby low-mass clusters, galaxy groups, and individual galaxies that also produce resolved signals. Such systems have been carefully looked at in X-rays and SZ in hopes of closing the baryon budget and understanding various feedback cycles (Bregman et al. 2018, Pratt et al. 2021, Bregman et al. 2022).

When constructing the training data, it appeared the simulations of Han et al. (2021) did not contain enough examples of the unique, resolved SZ sources observed in the real Universe. In order to overcome this, we created our own simulated set of resolved signals. These signals were generated based on X-ray observations reported in the *Meta-Catalog of X-Ray Detected Clusters of Galaxies* (MCXC; Piffaretti et al. 2011). We used the reported

[2]https://portal.nersc.gov/project/cmb/data/generic/mmDL/

masses (M_{500}[3]) and redshifts (z) and then calculated the angular size of R_{500} for each system. Resolved systems were selected as those with $R_{500} > 30^{'}$ which yielded a sample of 25 objects.

The next step was to simulate the SZ profiles of the resolved signals. They were generated using the universal pressure profile ($P(r)$) from the AGN 8.0 simulations of Le Brun et al. (2015). Their SZ surface brightness profiles, $y(r)$, as a function of physical radius is given by

$$y(r) = \frac{\sigma_{\rm T}}{m_{\rm e}c^2} \int_r^{R_{max}} \frac{2P(r')r'}{\sqrt{r'^2 - r^2}} dr' \tag{4.1}$$

where $R_{max} = 5R_{500}$, $\sigma_{\rm T}$ is the Thompson cross-section, $m_{\rm e}$ is the electron rest-mass, and c is the speed of light. These profiles were then superimposed with the simulated y-maps from Han et al. (2021). Herein, we denote the resolved part of the simulated y-maps as the resolved SZ component and that from Han et al. (2021) as background SZ. There were still a few resolved signals in Han et al. (2021), but we use this demarcation to distinguish the two components.

Then we superimposed the resolved profiles with the SZ background. Before injecting the signals, we added some randomization to help with generalization. Each object was placed at different distances by randomly simulating their signals at redshifts of $\pm 50\%$ their MCXC values. Furthermore, these were injected into the northern and southern Galactic hemispheres at random positions of moderately high Galactic latitudes ($|b| > 20^{\circ}$). This was to simply augment the sample while also avoiding the highly contaminating regions near the Galactic plane.

The resolved signals used for validation consisted of two data sets. The first was constructed in exactly the same way as the training data but using the three background SZ maps that were originally set aside. These were used for statistical analyses in section 4.4. The second set of validation data were made in order to inspect specific signals: a nearby galaxy group of $M_{500} = 10^{13} M_{\odot}$ at 10 Mpc ($\rm R_{500} = 113'$), a signal resembling the Coma cluster ($\rm R_{500} = 47'$), and that of the Virgo cluster ($\rm R_{500} = 177'$). These SZ profiles were also created using the AGN 8.0 pressure profile.

For the Coma- and Virgo-like sytems, ten realizations were generated with five injected both into the northern and southern Galactic hemispheres. For simplicity, we placed them at Galactic latitudes of $b = \pm 50^{\circ}$ and spaced them evenly in Galactic longitude starting at $l = 0^{\circ}$. For the galaxy group-like signal, we generated fifty signals and randomly placed them across the sky with a Galactic latitude restriction of $|b| > 20^{\circ}$. Separate y-maps were generated for each of the three systems, but they were superimposed with the same

[3]The subscript "500" denotes the property at which the density equals 500 times that of the critical density.

background SZ for consistency. These validation data were used to investigate the recovered radial profiles in section 4.4.

4.3.1.3 Planck Sky Model

Here we describe the modeling of non-SZ emissions, which we call contaminants. These were generated using the Planck Sky Model (Delabrouille et al. 2013) version that has been wrapped into Python (PYSM; Thorne et al. 2017). The Planck Sky Model was developed for simulating microwave radiation observed by the Planck satellite. This software was mainly developed to help researchers test their pipelines and validate cosmological models against observational data.

The components [4] used in this work included: Galactic thermal dust emission, synchrotron emission, anomalous microwave emission, free-free emission, the lensed CMB, CO line emission, cosmic infrared background (CIB), and radio galaxies. For some of these components, there was only one available model in PySM which included the SZ effect. A single realization of the SZ effect was not sufficient for our purposes which is why we incorporated the data products from Han et al. (2021). A consistent foreground model (d1-s1-a1-f1-c2-co1-cib1-rg1 components from PYSM) was used for the non-SZ components in all ten realizations. Therefore, the only differences between the simulated all-sky maps were the distributions of the SZ signal. The components were then integrated over the *Planck* and *WMAP* frequency response functions to simulate realistic observations. We implemented the publicly available transmission curves both for *Planck*[5] and *WMAP*[6] at their respective frequencies. Lastly, all of the frequency maps were produced in *HEALPix* format (Górski et al. 2005) with a resolution parameter NSIDE = 1410 which yields four pixels per resolution element of $10'$. Instrumental noise and beam effects were ignored for simplicity, but they may be worth including in future work.

4.3.2 SZ Signal Extraction

In this section, we explain the methods used to extract the SZ signal. We first present NILC in detail. Most importantly, we demonstrate the significance of its spatial parameter, Γ, that controls a bias-variance trade-off. Then we use the data products from multiple NILC extractions as input to a neural network called Deep-NILC. In the following, bold symbols indicate matrices or vectors.

[4] https://pysm3.readthedocs.io/en/latest/index.html
[5] https://portal.nersc.gov/cfs/cmb/planck2020/misc/
[6] https://lambda.gsfc.nasa.gov/product/wmap/dr5/bandpass_get.html

4.3.2.1 Internal Linear Combination (ILC)

The SZ effect boosts the energy of low-energy CMB photons ($\nu < 217$ GHz) to higher energies. This causes a distortion in the CMB spectrum that is well-grounded in theory and is given by

$$g_\nu = g(x) = \left(x \frac{e^x + 1}{e^x - 1} - 4 \right) \tag{4.2}$$

where $x = \frac{h\nu}{k_\mathrm{B} T_\mathrm{CMB}}$ (k_B is the Boltzmann constant, h is Planck's constant, and T_CMB is the temperature of the CMB). The amplitude of the SZ effect is measured as a dimensionless quantity known as the Compton parameter, y, given by

$$\frac{\Delta T}{T_\mathrm{CMB}} = g_\nu y \tag{4.3}$$

where $g(\nu)$ is the SZ spectral dependence, $\frac{\Delta T}{T_\mathrm{CMB}}$ is the change in temperature relative to the CMB.

In practice, the SZ signal is observed alongside other cosmological signals and Galactic emissions in the radio/IR bands. The observed intensity, X_ν, for each frequency channel, ν, at pixel, p, can be written as a sum of various components

$$X_\nu(p) = g_\nu y(p) + N_\nu(p) \tag{4.4}$$

where $N_\nu(p)$ denotes the signals from all non-SZ components, including instrumental noise as well as contaminating astrophysical signals. One can also rewrite Equation 4.4 as

$$\Delta X_\nu(p) = \Delta g_\nu y(p) + \Delta N_\nu(p) \tag{4.5}$$

where Δ represents the difference between two frequency bands. When X_ν is expressed in thermodynamic temperature units, the CMB has the same amplitude in each band and is deprojected from ΔN. This strategy was used by Pratt et al. (2021) where these authors subtracted subsequent frequency maps from the same instruments, and we applied their same method in this work. In the following equations, however, we drop Δ in our notation since Equation 4.4 and Equation 4.5 are mathematically similar.

ILC groups all non-SZ signals into a single noise term such that

$$\widehat{y(p)} = y(p) + \sum_\nu w_\nu(p) N_\nu(p) \tag{4.6}$$

where $\widehat{y}$ is the estimated SZ signal, and w_ν are the weights that minimize the total covariance projected along the $g(\nu)$ direction while also preserving the signal i.e., $\sum_\nu g_\nu w_\nu = \mathbf{g}\mathbf{w}^T = 1$.

These weights can be solved for with Lagrange multipliers

$$\mathbf{w} = \frac{\mathbf{g^T R^{-1}}}{\mathbf{g^T R^{-1} g}} \tag{4.7}$$

and the estimator of the SZ signal is

$$\widehat{y} = \mathbf{w^T X} \tag{4.8}$$

where $\mathbf{X}$ is the matrix of frequency observations, $\mathbf{R}$ is the covariance matrix $\mathbf{R} = \mathbf{X}\mathbf{X}^T$, and $\mathbf{w}$ is the vector of calculated weights.

The ILC solution completely depends on the construction of $\mathbf{R}$, which is derived from the data themselves. In the standard (simplest) ILC method, one uses all available data over the entire sky to calculate the weights. This assumes the spectral properties of the non-SZ emissions do not change across the sky. Such an assumption is naive since the contaminants are known to be non-stationary. In turn, the standard ILC method poorly separates the contaminants from the SZ signal.

One can achieve better ILC extractions by localizing data when constructing $\mathbf{R}$. Localization refers to the sub-grouping of data, under certain assumptions, to calculate the ILC weights. When the localization is strong—that is when data are finely segmented—the propagation of contamination can be suppressed. This reduces the variance in the reconstructed y-map. Conversely, strong localization renders a biased result when the localized contamination and SZ signal are correlated. While many of the contaminating signals may not be physically correlated with the SZ effect, random empirical correlations still exist.

This bias has been discussed in previous studies (Delabrouille et al. 2009, Remazeilles et al. 2013, McCarthy & Hill 2024) and we present an overview for completeness. The estimated SZ signal can be written as

$$\langle \widehat{y}^2 \rangle = \langle (y + \widehat{N})^2 \rangle = \langle y^2 \rangle + 2\langle y\widehat{N} \rangle + \langle \widehat{N}^2 \rangle \tag{4.9}$$

where $\widehat{N} = \sum_\nu w_\nu N_\nu$ equals the last term in Equation 4.6 and denotes the total amount of reconstructed noise. There is a correlation term between the SZ signal and the noise known as the ILC bias defined as

$$\langle y\widehat{N} \rangle = \frac{-\langle y^2 \rangle (m-1)}{N_p} \tag{4.10}$$

where m denotes the number of available frequency maps (or difference maps in this study) and N_p is the number of modes used to construct $\mathbf{R}$ (see derivation by Delabrouille et al. 2009). Note that this term is negative and, thus, reduces the power of the SZ signal. Rear-

ranging Equation 4.9 we get

$$\langle \widehat{y}^2 \rangle = \langle y^2 \rangle - \frac{2\langle y^2 \rangle (m-1)}{N_p} + \langle \widehat{N}^2 \rangle. \tag{4.11}$$

An optimal solution is reached when the sum of the last two terms is zero, or equivalently when

$$2(m-1)\langle y^2 \rangle = N_p \langle \widehat{N}^2 \rangle. \tag{4.12}$$

It is important to note that the reconstruction noise depends on N_p. Empirically, $\langle \widehat{N}^2 \rangle$ and N_p are positively correlated. Their relation, however, cannot be easily described because $\langle \widehat{N}^2 \rangle$ depends on the changing the contamination properties across the sky. This positive correlation suggests when $N_p \langle \widehat{N}^2 \rangle$ is large, an optimal balance can be achieved when $\langle y^2 \rangle$ is also large. This is a key point: one can afford a larger reconstruction error if the underlying signal is strong enough. On the other hand, if the true signal is weak, then one should consider reducing N_p to achieve a better solution.

4.3.2.2 Needlet Internal Linear Combination (NILC)

Among the most popular localization methods is the NILC algorithm, a modified ILC algorithm that controls N_p i.e., the strength of data localization. NILC harmonically and spatially localizes data on the sphere (Guilloux et al. 2007) by clustering them based on angular size and location on the sky. In practice, one first transforms the data into a wavelet basis, and then applies a spatial weighting scheme when constructing the covariance matrix in Equation 4.7. Below we describe the NILC method used throughout this work. We refer to Equation 4.13 as a guide for the workflow

$$\mathbf{X} \Longrightarrow \tilde{\mathbf{X}} \longrightarrow \tilde{\mathbf{R}} \longrightarrow \widehat{\tilde{\mathbf{y}}} \Longrightarrow \widehat{y}. \tag{4.13}$$

The double arrows ($\Longrightarrow$) denote a transforms to/from the wavelet basis. Single arrows ($\longrightarrow$) represent processes performed on individual wavelet scales. We denote some variable, Y, transformed in the wavelet domain as $\tilde{Y} = \{\tilde{Y}_1, \tilde{Y}_2, ..., \tilde{Y}_K\}$, where K is the number of window functions.

The first step ($\mathbf{X} \Longrightarrow \tilde{\mathbf{X}}$) was to transform the frequency data into a wavelet basis using harmonic window functions; this is the same as *Analysis* step from Delabrouille et al. (2009) These consisted of subtracted Gaussian beams characterized by their full-width at half-maximum (FWHM = $\mathcal{F}$). The wavelet bands were defined as: 10′-15′, 15′-30′, 30′-60′, $\mathcal{F}^u_{i-1}$ - $2\mathcal{F}^u_{i-1}$, ..., 960′-1200′. The window functions scaled dyadically using the largest FWHM of the previous window which we define as $\mathcal{F}^u_{i-1}$ where i indexes the wavelet bands and the

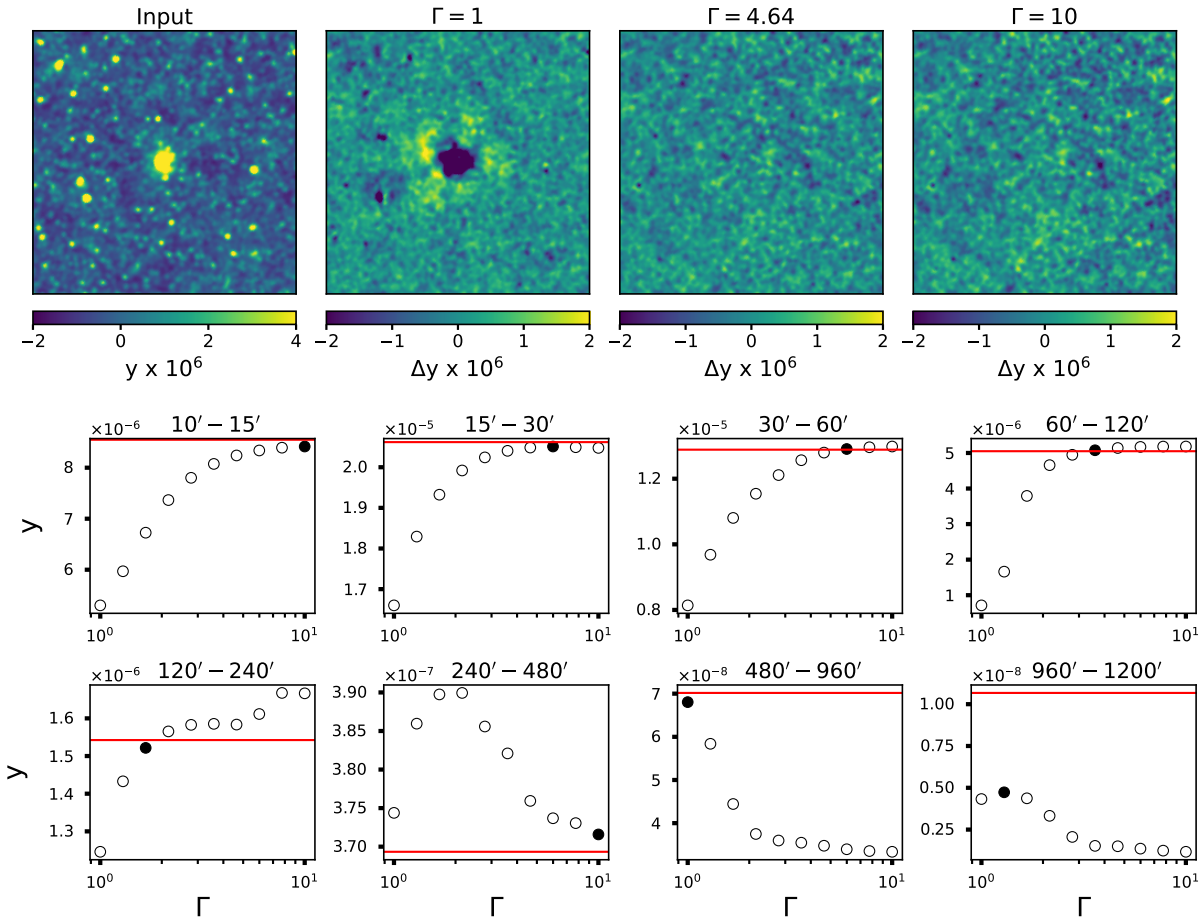


Figure 4.1 An example of how different values of Γ affect the NILC extraction of the SZ signal. The images in the top row are $10°x10°$ and centered around a strong simulated SZ source. The leftmost panel denotes the input SZ signal. The panels to the right show residuals between the input and reconstructed y-maps using three values of Γ. The eight panels below display the different estimates of the center pixel in the above images. They are shown as a function of wavelet scale and Γ. The best possible NILC solution given an array of Γ values are shown as filled circles; this is the closest estimate to the true value which is shown as a horizontal line in red. Summing the true values (red lines) on each wavelet scale yields the total SZ signal. The main point of this plot is to demonstrate how the choice of Γ impacts the estimate of the SZ signal. It also shows that larger values of Γ are typically preferred when performing extractions where the SZ signal is strong.

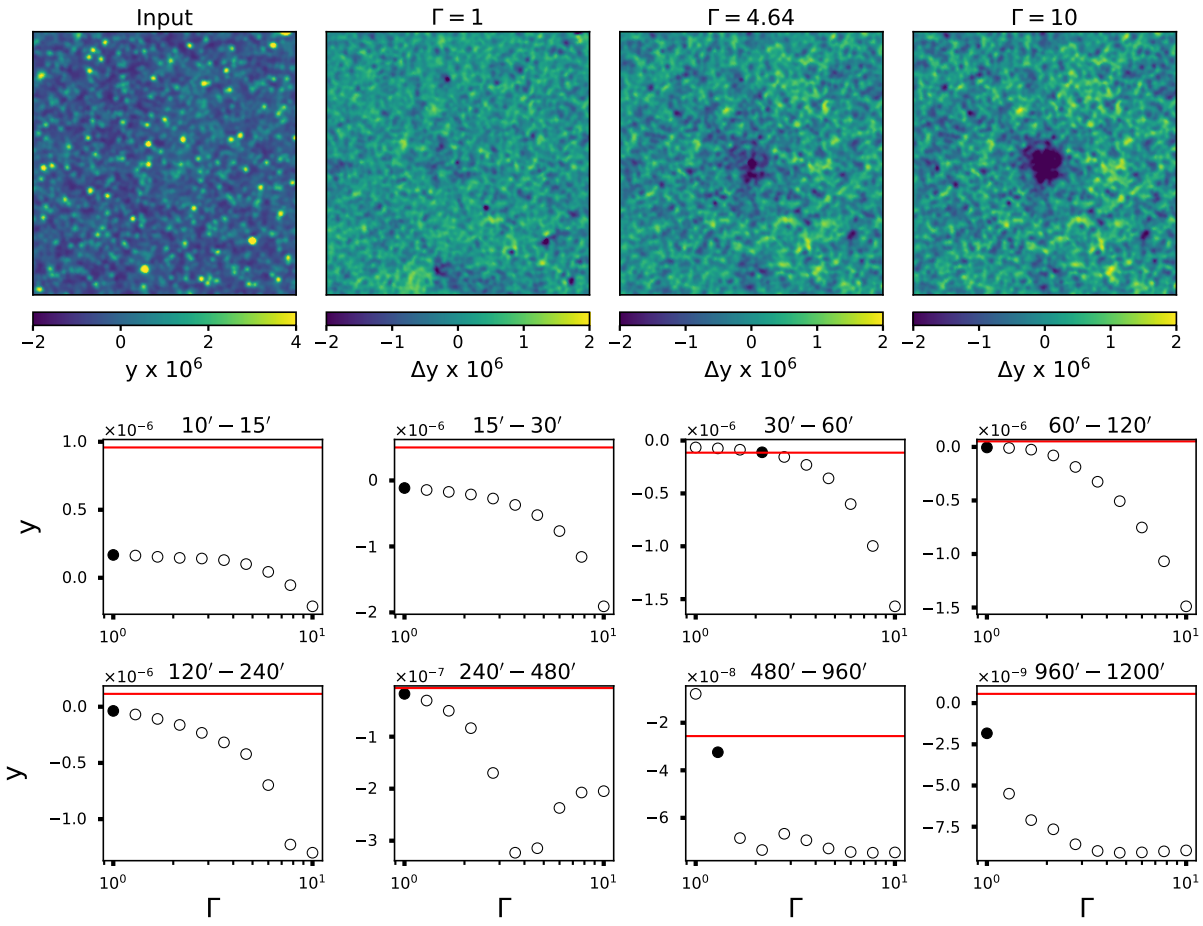


Figure 4.2 Same as Figure 4.1 except for the change in location of the sky. This example is centered around a pixel with a weak SZ signal, but it is also centered around a known radio source from the simulations. Smaller values of Γ were preferred in this scenario, which were generally true for pixels with weak SZ signals and/or strongly contaminated regions.

superscript $u(l)$ denotes upper(lower) FWHM for each window. For clarity, we note that $\mathcal{F}_i^l = 2\mathcal{F}_{i-1}^l$. However, dyadic scaling was not applied to the first and last windows because we set a maximum resolution of $10'$ and the largest scale at $20°$. Typically, the standard wavelet functions, ψ_i, are defined such that $\sum_i^K |\psi_i|^2 = 1$. The window functions used in this study, however, altered the sum to $\sum_i^K |\psi_i|^2 = G(\mathcal{F} = 10') - G(\mathcal{F} = 20°)$, where $G(\mathcal{F})$ represents the transmission of the Gaussian beam.

The first half of the window functions were applied to the frequency data, transforming them into a wavelet basis i.e., $\tilde{\mathbf{X}}_i = \langle \mathbf{X}, \psi_i \rangle$. (The second half will be applied later to satisfy the square-integrable condition.) Only some of the frequency data could be used in certain wavelet bands based on their corresponding beam sizes in either the *Planck* or *WMAP* missions. For example, only the data from the high-frequency instrument on *Planck* could be used in the first wavelet band because the resolution was better than $10'$.

The next step ($\tilde{\mathbf{X}} \longrightarrow \tilde{\mathbf{R}}$) was to obtain $\tilde{\mathbf{w}}$ by solving Equation 4.7. As previously mentioned, this depends entirely on the construction of $\tilde{\mathbf{R}}$. NILC spatially localizes data on a pixel-by-pixel basis by constructing $\tilde{\mathbf{R}}$ from only nearby pixels. The contribution of each pixel to $\tilde{\mathbf{R}}$ was based on an angular separation weighting scheme where closer pixels carried higher weights. We implemented a Gaussian weighting scheme (β) as a function of pixel separation, Δs, such that

$$\beta \propto e^{-\Delta s^2/\sigma^2} \tag{4.14}$$

where σ controlled the amount of spatial localization. σ was scaled with each window function such that

$$\sigma_i = \Gamma \times \mathcal{F}_i^{\mathrm{u}} \tag{4.15}$$

where Γ is the spatial localization parameter.

The next step ($\tilde{\mathbf{R}} \longrightarrow \widehat{\tilde{\mathbf{y}}}$) solved for the SZ signal in each wavelet band using Equation 4.7 and Equation 4.8. Then one applies the second application of the wavelet function to achieve full spatial resolution. The last step ($\widehat{\tilde{\mathbf{y}}} \Longrightarrow \widehat{y}$) was the wavelet reconstruction $\widehat{y} = \sum_i^K \tilde{y}_i$ which added the y-maps per wavelet scale; this is the same as *Synthesis* step from Delabrouille et al. (2009). In the next section, we skip this last step and, instead, use the y-maps per wavelet scale as input to a neural network.

4.3.2.3 Deep-NILC

In this section we explain the pipeline to produce a y-map with Deep-NILC. There are two main parts: the first is a data pre-processing stage using the NILC algorithm, and the second step models these data using a neural network.

The first part of the pipeline was to apply the NILC algorithm to our set of simulated data.

Unlike the traditional NILC, we did not assume some Γ but rather performed extractions for a range of reasonable values; specifically, ten values of Γ with logarithmic spacing from [1-10] (i.e., 1, 1.292, 1.668, ..., 10). A total of 80 decomposed y-maps were created for a single simulation of the sky given the eight harmonic bands and ten values of Γ.

Varying Γ provided information on how the ILC weights reacted to the surrounding contamination. One could imagine scenarios where using one value would be more suitable than others. For example, Figure 4.1 shows an example of how altering Γ affected the extraction for a pixel near the center of a strong cluster. According to Equation 4.12, extracting the SZ signal around a massive cluster should be done with a large value of Γ. In this case, the signal was large enough where one becomes more concerned about the bias rather than contamination. The residual images shown in the top row of Figure 4.1 demonstrated that larger values of Γ yielded better estimates near a strong SZ source. On the other hand, Figure 4.2 shows a case where the SZ signal was weak and coincident with a known radio source from the PySM simulations. In this case, $\Gamma = 1$ helped reduce the contaminating signal from the radio source. One can see the true values (red lines) did not agree well with any of the NILC solutions for the first couple of wavelets, however, the solution when $\Gamma = 1$ was the closest match. Based on the arguments above, one can achieve better NILC extractions when Γ is allowed to vary.

Now, we seek a model that can take NILC extractions from various Γ values to improve estimations of the SZ signal. In order to tackle this problem, we used a fully connected, feed-forward network known as a multilayer perceptron (MLP). MLPs consist of multiple layers of interconnected nodes, known as neurons. The networks are designed to process information from the input layer, through a set of hidden layers to the output layer. Each neuron receives signals from the neurons in the previous layer and returns a weighted linear combination of the inputs. The result then undergoes a non-linear activation function which is then fed as input to the next layer. The parameters of the network are then trained with supervised learning through an iterative procedure known as gradient descent. After each iteration, the trainable parameters are updated to minimize the error between the desired output and predicted output.

The network performed regression by minimizing the mean absolute error (MAE) loss function

$$\text{MAE} = |y - y'| \tag{4.16}$$

where y' denotes the best possible NILC solution. In other words, y' was constructed from the Γ that yielded the closest value to the true SZ signal on each wavelet scale then summing them together. Examples of this are shown as the black circles in Figure 4.1 and Figure 4.2. We note the only purpose of $y^{'}$ was for training the MLP, and it is not available for real

data.

We chose to regress on y' instead of the true SZ values to keep our model from over-correcting, and keeping the results within the confines of the NILC method. Taking Figure 4.2 as an example, many of the NILC predictions were far away from their true values when extracting the SZ signal in a highly contaminated region. If we regressed on the true values, this region would increase the MAE and the model would work hard to accommodate to the large residuals. Replacing the true values with y' mitigates this impact by reducing the range of residuals.

Table 4.1: Neural Network Parameters

Input dimensions	10 (N_Γ) $\times$ 8 (K)
Output dimensions	1
Number of hidden layers	9
Number of neurons	80, 40, 20, 20, 10, 10, 5, 5, 3
Activation (hidden)	Leaky ReLU
Activation (output)	Linear
Optimizer	Adam
Batch size	64
Initial learning rate	0.001
Loss function	MAE

A number of hyperparameters had to be defined, and those of our network are shown in Table 4.1. The input layer accepted a matrix of shape (K $\times$ N_Γ) where N_Γ represents the ten Γ values. The data were then flattened into a vector before passing to the first hidden layer. The MLP contained nine hidden layers with Leaky Relu activation functions (slope for negative values was 0.01) after each hidden layer. The output layer used a linear activation and yielded a single number. In addition, normalization was applied to the input and output data to help train the model by scaling and shifting them to have zero mean and unit variance. We tuned our model to find optimal values of the initial learning rate, mini-batch size, number of layers, and number of nodes per layer. We decided to use the Adam optimizer (Kingma & Ba 2014) with an initial learning rate of 0.001 with exponential decay rates of 0.9 and 0.999 for the first and second moments respectively. The most sensitive hyperparameter was the learning rate. All other hyperparameters, such as the batch size and network architecture, did not require meticulous tuning. Finally, we restricted the set of training pixels to be at Galactic latitudes $|b| > 10^\circ$ to avoid training in the most highly contaminated regions.

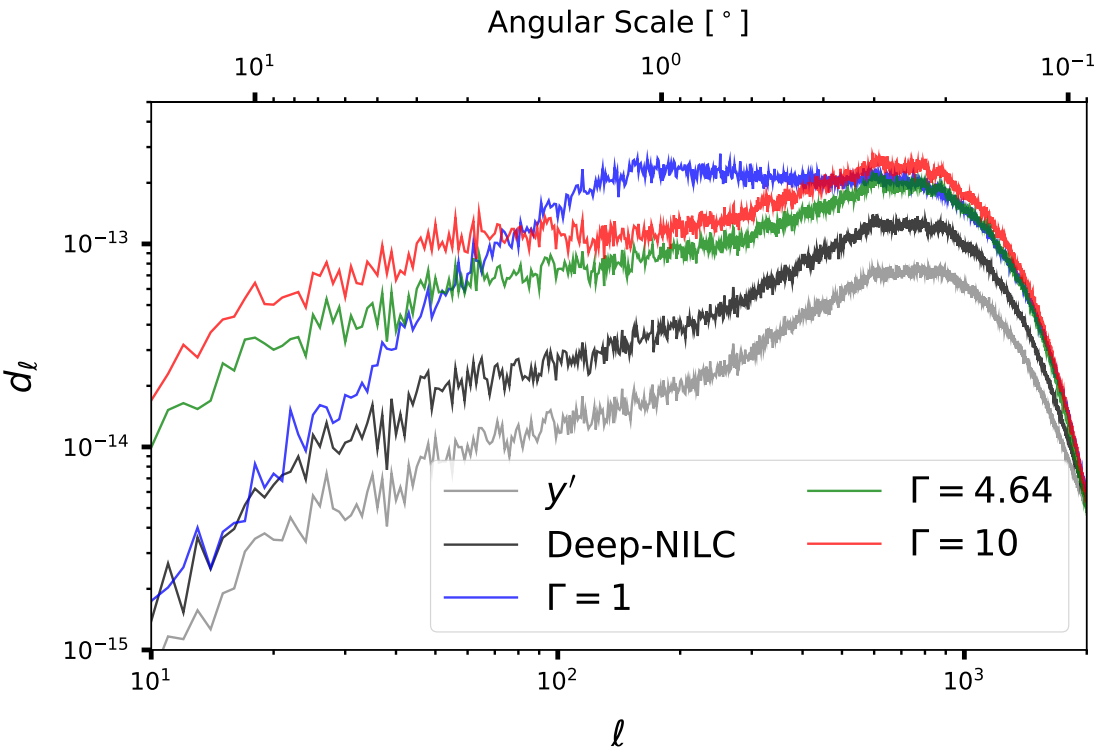


Figure 4.3 Average residual power spectra for the three validation y-maps. The gray line denotes the residual for the best possible NILC solution and black is the results from Deep-NILC. The blue, green, and red are the residuals for $\Gamma = 1, 4.64, 10$ respectively.

4.4 Results

In this section, we present the main results from the validation data. Specifically, we focus on the performance of Deep-NILC to the y-maps generated with fixed values of Γ. We consider three nominal values of gamma to give a sense of how NILC extractions behave: $\Gamma = 1, 4.64$, and 10. (These were selected from a set of Γ values with logarithmic scaling.) First, we show residual statistics between the estimated y-maps and the true signal including: power spectra, bias estimates, and cross-correlations between the strongest contaminants. Then we present the radial profile extractions for resolved systems.

4.4.1 Residual Power Spectra

Here we consider the power spectra of the residual maps $(\widehat{y} - y)$, where y is the true SZ signal. The residual power, $\mathbf{d}_\ell$, defined as $\frac{\ell(2\ell+1)}{2\pi}\Delta C_\ell$ where ΔC_ℓ was computed from the residual map after setting pixels of low Galactic latitude ($|b| < 10°$) to zero. In Figure 4.3, we show the residual power for five y-maps. The gray line shows the results for the best

possible NILC solution (y'); the black line denotes Deep-NILC; and the colored lines display the results for fixed values of Γ. As expected, the gray line showed the smallest amount of residual power. The blue line exhibited the largest amount of power for $\ell \sim 200$, but less power compared to the other values of Γ when $\ell \lesssim 40$. Deep-NILC had the least amount of residual power compared to all fixed values of Γ on all angular scales.

4.4.2 Bias and Scatter

This section presents the residuals as a function of SZ signal strength. For this part, pixel values were first separated into logarithmic bins of size 0.25 dex. Then we calculated two quantities: the empirical bias $B = \langle \widehat{y} - y \rangle$ and scatter $\mathbf{\Sigma^2} = \langle (\widehat{\mathbf{y}} - \mathbf{y} - \mathbf{B})^{\mathbf{2}} \rangle$. In Figure 4.4, we plot the average values of the three validation maps. The color coding is the same as in Figure 4.3.

In the top-left panel, we show the fractional empirical bias. The $\Gamma = 1$ extraction yielded a negative fractional bias, especially for moderate to large SZ signals. Larger values of Γ (i.e., 4.64 and 10) appeared to show almost no bias for $y > 10^{-7}$, but yielded a positive bias for weaker signals. Finally, the best NILC solution showed a slight negative fractional bias that decreased as the SZ signal increased, albeit only by a few percent. The results of Deep-NILC produced an unbiased solution for strong SZ signals $y \gtrsim 10^{-5}$, however, it returned a steep negative bias moving toward weaker signals, reaching 50% bias by $y \sim 10^{-7}$. We note the the empirical bias is not the same as the ILC bias presented in Equation 4.10. The ILC bias stems from the amount of available modes used to construct the covariance matrix in each wavelet band. The empirical bias includes the ILC bias, however, it also depends on the contaminating properties which are not stationary.

The top-right and bottom-left panels include the fractional empirical scatter. The bottom-left panel shows dashed and solid lines to denote the empirical bias and scatter respectively. The circle points represent these two quantities added in quadrature, and we call this the total fractional error. One can see the total fractional error for $\Gamma = 1$ was dominated by the bias for large SZ values, but this changed as the signal dropped below $y < 10^{-5}$. For $\Gamma = 10$, however, the bias remained subdominant to the scatter for all values. Looking at y$'$, the total error was controlled by the scatter for all signal strengths. This same trend was also observed for Deep-NILC.

In the bottom-right panel we show the expected signal-to-noise which we define as

$$\mathrm{S/N} = \frac{y - B}{\Sigma} \tag{4.17}$$

The main takeaway from this plot is the S/N for Deep-NILC was larger for all fixed values

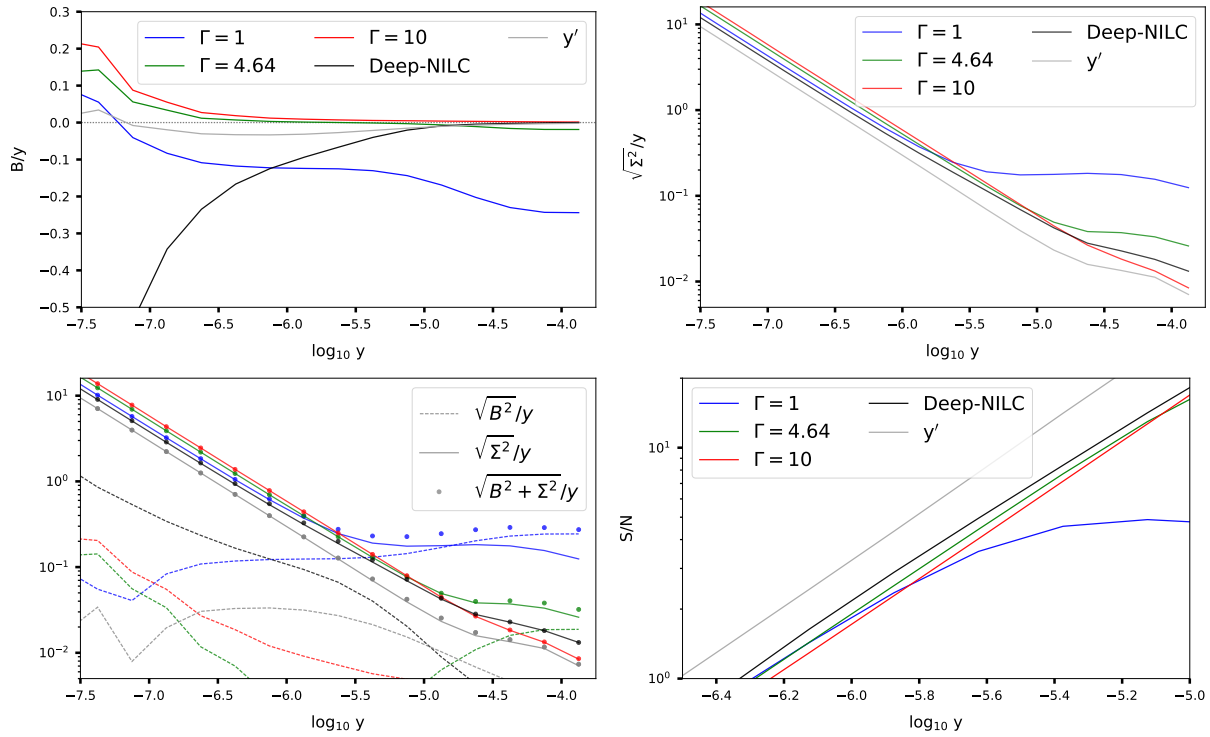


Figure 4.4 (top-left) The fractional bias as a function of SZ signal strength. We show the results for the three nominal values of Γ, Deep-NILC, and the best possible NILC solution. (top-right) Same as top-left panel but for the empirical scatter. (bottom-left) Displays the contributions from each source of error. The dashed lines show the absolute values of the top-left panel, solid lines show those from the top-right panel, and the circles denote the total contribution from both components. (bottom-right) The expected S/N for the pixel values. The y-axis is truncated at S/N= 1 and where $\log_{10}$y = −5.

of Γ over most values of SZ signal. We discuss the implications of these results in section 4.5 to argue Deep-NILC offers an improved solution.

4.4.3 Component Correlation

These results show the correlation between the residual y-maps and known sources of contamination. We used the correlation coefficient

$$r_\ell = \frac{C_\ell^{a\times b}}{\sqrt{C_\ell^a C_\ell^b}} \tag{4.18}$$

where a and b represent two maps of the sky, and $a \times b$ denotes a cross-correlation. We set one of these to be the residual y-map while the other was a map of the contamination component. Most of the components did not show significant correlation with the residuals.

The strongest correlations occurred with the SZ effect itself and the CIB.

The cross-correlation coefficients between the residuals and the SZ signal are shown in the left panel of Figure 4.5. A strong negative correlation existed for $\Gamma = 1$ on nearly all scales. As Γ increased, however, the correlation coefficient decreased. Essentially, no correlation was seen by the time $\Gamma = 10$. The best NILC solution also exhibited a slight negative correlation and was similar to the results of $\Gamma = 4.64$ and Deep-NILC.

The right panel of Figure 4.5 shows the residual correlation with the CIB. Positive correlations were seen on moderate to large scales for most values of Γ. The most positive correlations were observed for the largest values of Γ. Deep-NILC and y' produced nearly identical correlations and were quite similar to that of $\Gamma = 4.64$.

4.4.4 Radial Profiles of Resolved Systems

Here we explain how radial profiles of the resolved systems were extracted from a given y-map. Before the extractions, the largest SZ values were masked to mitigate the contributions from nearby signals. We masked the pixels in the top 5% of pixel values found in a 20° radius in the background SZ. The group- and Coma-like signals were extracted out to $400'$ and $300'$ respectively in $10'$ circular bins. Mean values calculated from the outer five bins were then subtracted off as a local background correction for each field. The Virgo-like system was extracted out to $700'$ using the last ten annuli for the local background correction.

Next, we calculated the stacked signal for each type of systems. For the ten Coma- and Virgo-like signals, we took the mean value and the standard deviation across each annulus as a measure of the uncertainty. We did not use the error on the mean value since these signals are unique in the sense we can only make one observation of them in the real Universe. For the galaxy group-like signal, we performed bootstrap sampling using sample sizes of ten. Galaxy group signals are too weak to be studied individually, so in practice, one would have to stack their signals to get a robust measurement. We chose a sample size of ten to mimic the sample size of nearby galaxy groups used in (Pratt et al. 2021).

In the left column of Figure 4.6, we show the stacks of resolved signals. The results from Deep-NILC are plotted as black circles while those from the three nominal values of Γ are shown as colored stars. We omit the results for $\Gamma = 4.64$ in the group- and Virgo-like rows for visualization purposes; the results for $\Gamma = 4.64$ generally lied between those from $\Gamma = 10$ and $\Gamma = 1$. The black line represents the injected profile that we tried to recover, however, it is more important to look at the cyan data. These represent the true stacked signal which is the superposition of the background SZ signals and the injected signals. In reality, one can not perfectly recover the black line as the injected signal becomes convolved with the

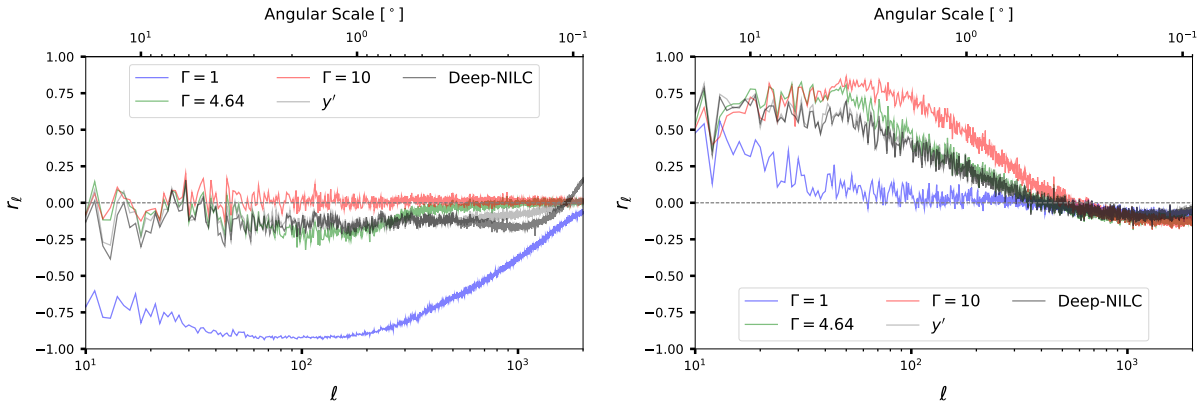


Figure 4.5 Cross-correlation coefficients using the residuals from y', Deep-NILC, and the three nominal values of Γ. (left) Correlation between the residuals and the SZ signal. The best possible NILC solution is in gray and lies just below zero for all ℓ. (right) Same as left panel but for the CIB. The main takeaway here is that Deep-NILC (black line) closely followed the best NILC solution (gray line) which was desirable.

background SZ.

For the galaxy group-like signal, the results of Deep-NILC generally were between those of $\Gamma = 10$ and $\Gamma = 1$. The statistical errors for Deep-NILC were roughly 60% those of $\Gamma = 10$, however, Deep-NILC yielded a larger bias as seen in Table 4.2. There was very little difference between Deep-NILC and $\Gamma = 10$ for the Coma-like signal, but $\Gamma = 1$ performed poorly with large bias. Looking at the Virgo-like system, there was a clear negative bias for Deep-NILC while $\Gamma = 10$ returned accurate and acceptable results. For better inspection, we plot the empirical bias, scatter, and total error for the stacks in the appendix.

In the right panel of Figure 4.6 we show the cumulative "SZ flux" given as

$$Y(r) = \sum_{i;r_i<r} 2\pi r_i y(r_i) \Delta r \tag{4.19}$$

each radial bin is indexed by i, and $\Delta r = 10'$ which is the angular width of each bin. This observed quantity is important as it is directly relatable to the total gas mass enclosed within some radius. We estimated the SZ flux values within 1, 2, and 3 R_{500} for each system indicated by the dotted brown lines. Then we calculated the percent differences from the true Y for the three Γ values and Deep-NILC which are presented in Table 4.2. We discuss these results further in section 4.5.

Galaxy Group	R_{500}			2 R_{500}			3 R_{500}		
	$\langle B \rangle$	$\langle \Sigma \rangle$	$\langle \sqrt{B^2+\Sigma^2} \rangle$	$\langle B \rangle$	$\langle \Sigma \rangle$	$\langle \sqrt{B^2+\Sigma^2} \rangle$	$\langle B \rangle$	$\langle \Sigma \rangle$	$\langle \sqrt{B^2+\Sigma^2} \rangle$
$\Gamma = 10$	-18.6%	51.1%	54.4%	-14.8%	62.2%	64.0%	35.7%	76.3%	84.3%
$\Gamma = 4.64$	-15.9%	44.0%	46.7%	6.66%	53.2%	53.6%	16.9%	69.2%	71.2%
$\Gamma = 1$	-55.2%	21.0%	59.0%	-60.2%	22.7%	64.4%	-72.2%	36.3%	80.9%
Deep-NILC	-42.3%	28.7%	51.1%	-41.0%	24.4%	47.7%	-39.3%	33.1%	51.4%
Coma	R_{500}			2 R_{500}			3 R_{500}		
	$\langle B \rangle$	$\langle \Sigma \rangle$	$\langle \sqrt{B^2+\Sigma^2} \rangle$	$\langle B \rangle$	$\langle \Sigma \rangle$	$\langle \sqrt{B^2+\Sigma^2} \rangle$	$\langle B \rangle$	$\langle \Sigma \rangle$	$\langle \sqrt{B^2+\Sigma^2} \rangle$
$\Gamma = 10$	0.6%	1.1%	1.3%	1.6%	2.5%	2.9%	2.5%	4.5%	5.1%
$\Gamma = 4.64$	-8.4%	4.1%	9.3%	-5.2%	3.2%	6.1%	-1.9%	4.9%	5.3%
$\Gamma = 1$	-79.2%	7.0%	79.5%	-75.4%	8.2%	75.8%	-65.4%	11.5%	66.4%
Deep-NILC	0.4%	1.9%	1.9%	0.8%	2.3%	2.4%	0.8%	4.1%	4.2%
Virgo	R_{500}			2 R_{500}			3 R_{500}		
	$\langle B \rangle$	$\langle \Sigma \rangle$	$\langle \sqrt{B^2+\Sigma^2} \rangle$	$\langle B \rangle$	$\langle \Sigma \rangle$	$\langle \sqrt{B^2+\Sigma^2} \rangle$	$\langle B \rangle$	$\langle \Sigma \rangle$	$\langle \sqrt{B^2+\Sigma^2} \rangle$
$\Gamma = 10$	2.4%	2.7%	3.6%	2.4%	4.2%	4.8%	2.3%	8.5%	8.8%
$\Gamma = 4.64$	1.1%	2.1%	2.4%	3.0%	3.8%	4.8%	3.5%	7.1%	7.9%
$\Gamma = 1$	-51.4%	10.3%	52.4%	-42.9%	10.5%	44.1%	-41.0%	14.2%	43.4%
Deep-NILC	-2.6%	3.4%	4.3%	-4.5%	5.3%	7.0%	-7.4%	7.4%	10.5%

Table 4.2 Percent Difference in Y.

4.5 Discussion

4.5.1 Deep-NILC vs. Fixed Spatial Parameter

Our results demonstrated that Deep-NILC outperformed NILC algorithms that assumed a fixed value of Γ. Small values of Γ, specifically $\Gamma = 1$, produced highly biased results. This was most evident in the top-left panel Figure 4.4 where the average bias was $\sim 10\% - 20\%$. It was also manifested in the bottom-left panel of Figure 4.4 where the bias term provided the most contribution to the total fractional scatter for large SZ signals. The same idea was also reflected in the left panel of Figure 4.5 which showed a very strong correlation between the residuals and the SZ signal. This is why $\Gamma = 1$ exhibited the largest residual power in Figure 4.3.

Furthermore, $\Gamma = 1$ yielded the worst extraction for Coma- and Virgo-like systems, however, its performance was better for the galaxy group-like signal. For the pixel-by-pixel statistics, $\Gamma = 1$ yielded the best results for weaker SZ signals and on the largest scales. Part of the reason could be due to the lack of correlation seen between the residuals and the CIB. In other words, smaller values Γ did better at extracting weak and/or large-scale signals because they reduced the effects from contamination. Nevertheless, the large observed bias was prominent and would not be suitable for most SZ studies.

The story was essentially reversed when looking at larger values of Γ. We found that $\Gamma = 10$ provided the most unbiased solutions but with the strongest residuals. In Figure 4.4 we demonstrated the bias term was insignificant compared to the empirical scatter. Moreover, there was a modest positive bias for weak SZ signals at large radii which likely coincided with the positive correlation seen with the CIB in Figure 4.5.

Deep-NILC outperformed the extractions for both large and small values of Γ by providing a balance between the bias and variance. This balance was seen in the bottom-left panel of Figure 4.4 where Deep-NILC approached the solution for $\Gamma = 10$ for large SZ values and that of $\Gamma = 1$ for weak signals. These results mean that Deep-NILC was able to adjust the localization based on the strength of the SZ signal. We also observed Deep-NILC to have the smallest residual power in Figure 4.3 and more accurate recoveries of the group- and Coma-like profiles in Figure 4.6 and Table 4.2.

4.5.2 Caveats

Deep-NILC comes with limitations. Most importantly, the algorithm relies heavily on the quality of simulated data. The data used in this work were generated using a set of ten different y-maps but only one realization of contaminating components. One might argue

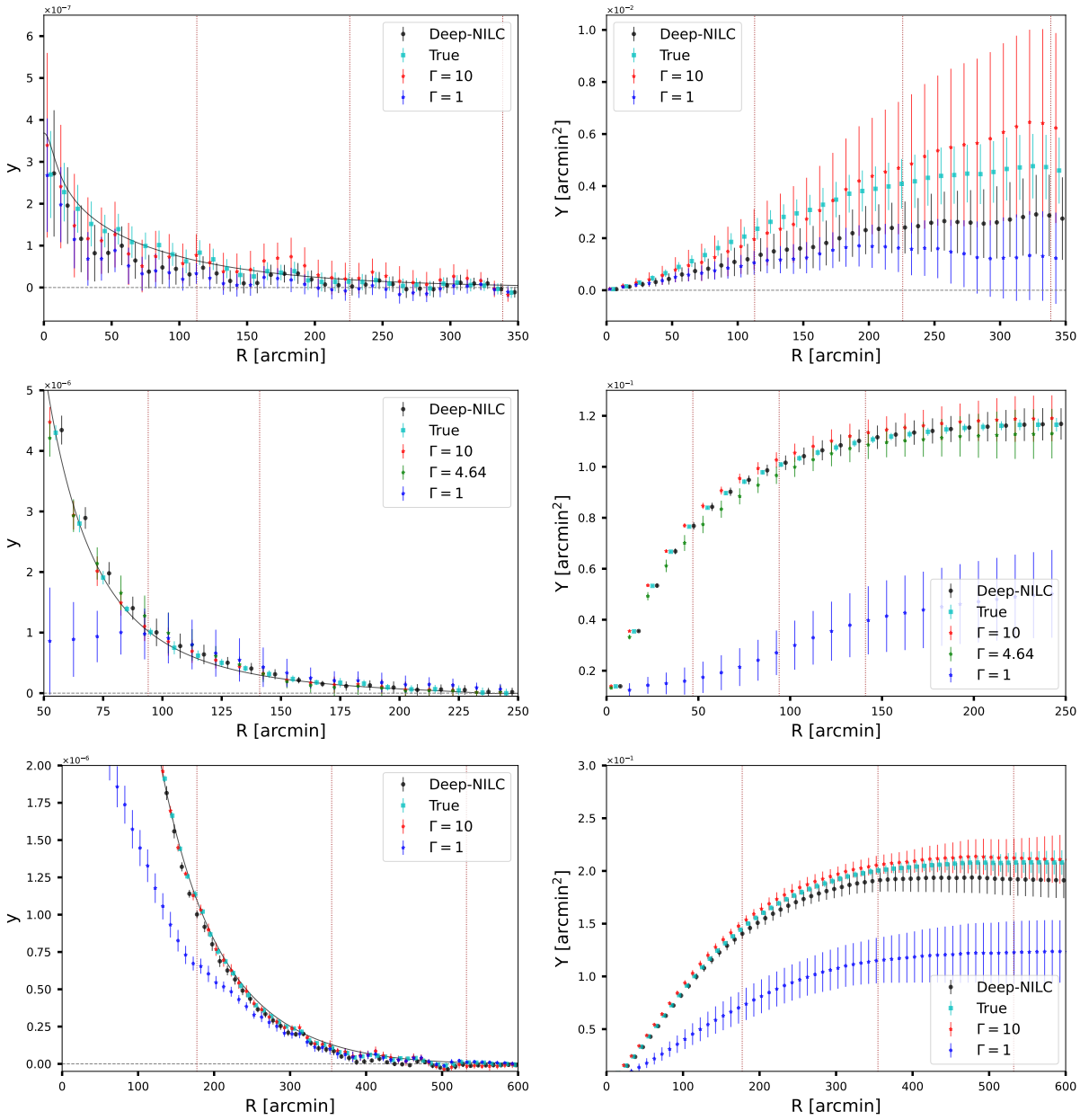


Figure 4.6 The left column shows the stack of ten radial profiles for three resolved signals. The right column shows the cumulative SZ flux. The group-, Coma-, and Virgo-like signals are shown in the top, middle and bottom panels respectively. The results from different values of Γ are shown as stars, those from Deep-NILC as black circles, and the true signal as cyan squares. The stars and circles are slightly offset in the horizontal direction to help with visualization. Extractions for $\Gamma = 4.64$ are not shown in the group- and Coma-like panels to avoid over-crowding. The black line shows the profile that was injected into the simulated y-map, and the dotted brown lines indicate the positions of 1, 2, and 3 R_{500}. The error bars show the standard deviation of the mean for each annulus. The cyan points do not exactly match the input profile since the injected signal has been convolved with other nearby SZ signals. The error bars on the cyan squares are the statistical fluctuations of the true signal within the stack after some masking. The main point of this plot is to show how well resolved signals are recovered with Deep-NILC and different values of Γ.

that this could lead to over-fitting to this specific set of signals. In the future, emphasis should be placed on including varying the foreground emission models. However, we note that the NILC estimate was also affected by other nearby SZ signals as they were contained in the covariance matrix. In this sense, the SZ signal can be thought of a contaminant itself using NILC. One way around this might be to mask strong SZ sources before constructing $\mathbf{R}$. Nevertheless, the different y-maps we used gave a variety SZ distributions, and this helped provide generalization to our model.

Also, building a model with supervised learning is sensitive to the diversity of training examples. We had to include additional resolved SZ signals to augment the y-maps from Han et al. (2021). This was imperative for our model to learn about the resolved "anomalies" seen in our real sky, such as the Coma and Virgo clusters. It is likely, however, that there were not enough examples in the training data of a Virgo-like cluster. The Virgo cluster is very unique as it is the only prominent SZ signal that extends multiple degrees on the sky. In our methodology, we injected resolved systems based on the MCXC catalog, so only a few instances of Virgo-like systems were included in the training set. In Figure 4.6, a non-trivial bias was observed for the Virgo-like stack, however, this was not observed for the Coma-like and galaxy group-like signals which were much smaller in angular size. Furthermore, the majority of SZ sources produced zero signal on large-scales. Wrapping this together with the sample imbalance is what probably caused Deep-NILC to under-predict the signal of Virgo.

Another potential drawback of our simulated data set was the omission of spatially correlated components. For example, a background AGN may produce strong emissions both in radio and IR. If strong enough, they may significantly affect the NILC extraction. Also, radio-loud AGNs often sit at the center of galaxy clusters (e.g., Virgo cluster). Deep-NILC was not trained to see these spatially correlated components, thus, we caution that Deep-NILC could yield unreliable results in some instances of real data. This may be worth exploring in future work as simulations improve.

The simulated data used in this work also did not consider instrumental noise or beam effects. Currently, adding realistic instrumental noise is not incorporated into PySM, however, one could simply add white Gaussian noise to the frequency data. Adding instrumental noise would affect the calculation of the ILC weights and raise the reconstructed uncertainty floor. In turn, the gray line in Figure 4.3 would shift upward along with the rest of the lines. Deep-NILC, however, does not explicitly handle the noise after the ILC calculation as it takes the different NILC solutions as preprocessed input. In addition, beam effects were ignored in the development of Deep-NILC. For real data, one must deconvolve the individual frequency maps and reconvolve them to a common frequency (McCarthy & Hill 2024, Chandran et al. 2023; e.g.,). We do not include this component to focus on the method as

a proof-of-concept.

Finally, we reiterate that Deep-NILC was still bounded by the capabilities of the NILC algorithm. This is because we regressed using the best NILC solution, so Deep-NILC could not perform better than the Γ values used here. If no combination of the Γ values could yield reliable results then Deep-NILC would not do any better. Furthermore, we did not investigate the full parameter space of NILC. Even though we considered a grid of spatial parameters, we chose to fix the set of harmonic window functions. Using a more diverse set of harmonic filters could help improve the performance of Deep-NILC, but we leave this to future work.

4.6 Summary

This study investigated the systematic effects of the NILC method when extracting the SZ signal. Our methods included injecting synthetically generated y-maps into a simulated foreground of radio/IR emissions. These emissions were then computed as band-averaged signals that would mimic the observations seen by the *Planck* and *WMAP* satellites.

Next, we performed the NILC component separation technique in attempt to recover the input SZ signal. The main focus was on the spatial parameter, Γ, which controlled the amount of contamination and bias. Mathematically, we demonstrated an optimal value for Γ exists that minimizes the contribution from both of these effects. It was then argued that it is nearly impossible to analytically calculate the best value of Γ *a priori* as it depended on many complicated variables, such as the varying level of nearby contamination.

We went on to show how altering the value of Γ significantly changed the performance of the SZ extraction. Specifically, we found that small values of Γ tend to yield better results when attempting to extract weak SZ features and/or when there exists significant contributions from contamination. One the other hand, bigger values of Γ yielded unbiased solutions and performed better when extracting large SZ signals.

Rather than using a fixed value of Γ, we developed an algorithm to improve the NILC solution known as Deep-NILC. Deep-NILC required various NILC extractions for different values of Γ. These were then fed into a MLP to predict the SZ signal. The main takeaway from our experiments are the following:

- Deep-NILC yielded smaller residual power on all angular scales compared to all values of fixed Γ as shown in Figure 4.3.
- The correlation between the Deep-NILC residuals and known contaminants, particularly the CIB and the SZ signal itself, were closest to that obtained by the best possible

NILC solution (see Figure 4.5).

- The sum of the empirical bias and scatter terms seen in Figure 4.4 suggested Deep-NILC rendered the smallest deviations for nearly all strengths of SZ signals. The one exception being at $y \gtrsim 10^{-4}$ where $\Gamma = 10$ performs slightly better, but this was a marginal difference.

- When stacking the resolved profiles for galaxy group-like signal, Deep-NILC yielded the best results when considering the total contributions from the bias and scatter.

- Deep-NILC under-predicted the signal coming from a Virgo-like source which was likely due to an imbalance in the training data. However, the inferred SZ flux for Deep-NILC was only biased at the 10% level.

There are many other approaches that can, and should, be investigated using machine learning. As simulation data quality continues to improve and as future missions bring observational insights, data-driven models may soon supersede analytical techniques. Deep-NILC provides a bridge between analytical and data-driven solutions which could provide potential improvements to a variety of problems. In the future, one might be able to build a model that could learn the SZ signal without doing any pre-processed component separation.

We would like to thank the anonymous referee for providing excellent feedback to help improve this work. We would also like to thank Camille Avestruz, Jennier Li, and Ashley Villar for useful conversations regarding DL. In addition, we want to thank Charles Antonelli and John Theils for computational support. This project also made use of the Great Lakes computing cluster at the University of Michigan–Ann Arbor. We are grateful for support from the NASA grants AWD012791 and 21-ADAP21-0069.

4.7 Appendix

4.7.1 Wavelet Bands

In the figure below, we show the wavelet bands in multipole space. The black lines are show the individual bands while the dashed red line is the full beam profile. The full profile is a Gaussian beam with FWHM = $10'$ truncated at FWHM = $20°$.

4.7.2 Bias and Scatter of Radial Profiles

Here we provide the empirical bias, scatter, and total error for the resolved systems considered in this work: galaxy group-, Coma-, and Virgo-like systems shown in Figure 4.8, Figure 4.9,

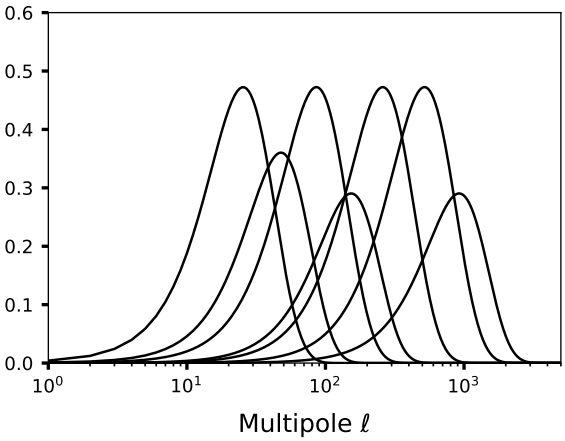


Figure 4.7 Harmonic window functions as a function of multipole.

and Figure 4.10.

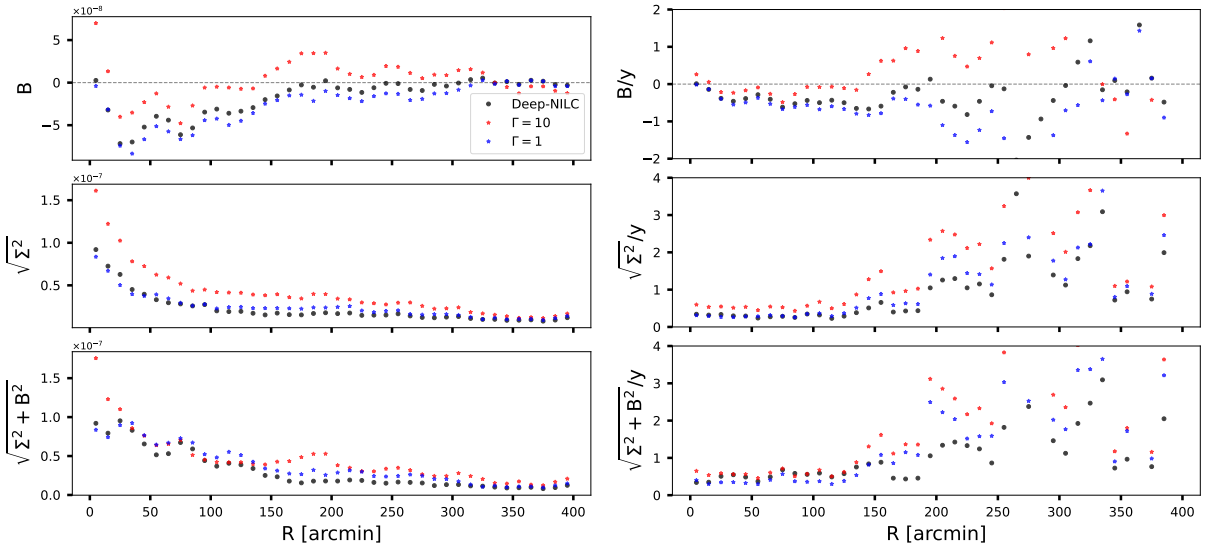


Figure 4.8 The average bias, scatter, and total error for galaxy group-like signals are shown in the top, middle, and bottom panels respectively. These quantities are shown in the left column while they are shown as a fraction of the SZ signal in the right column.

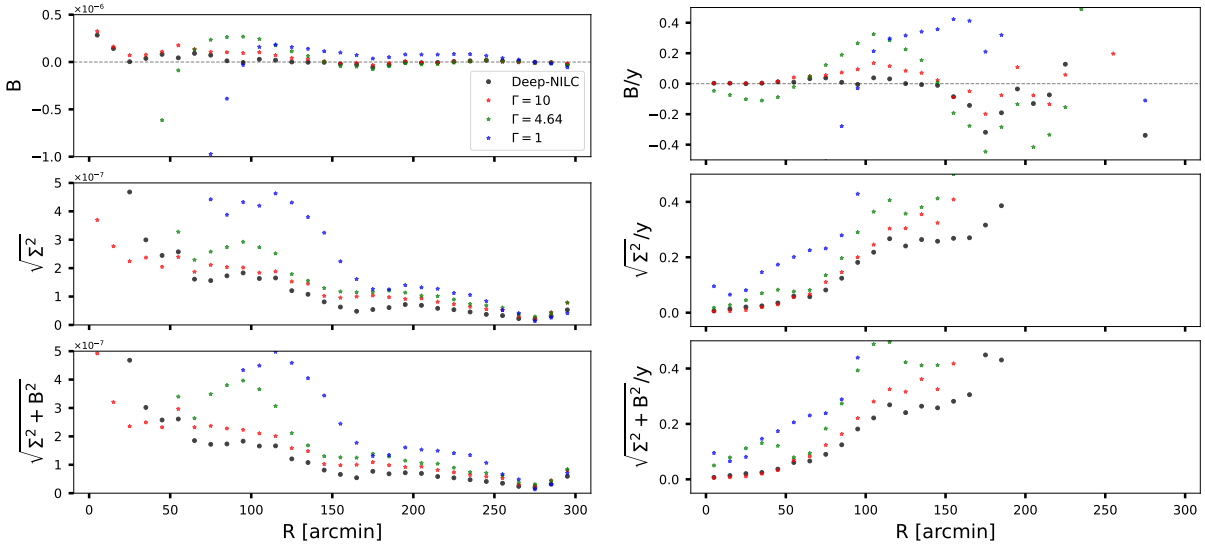


Figure 4.9 Same as Figure 4.8 but for a Coma-like system.

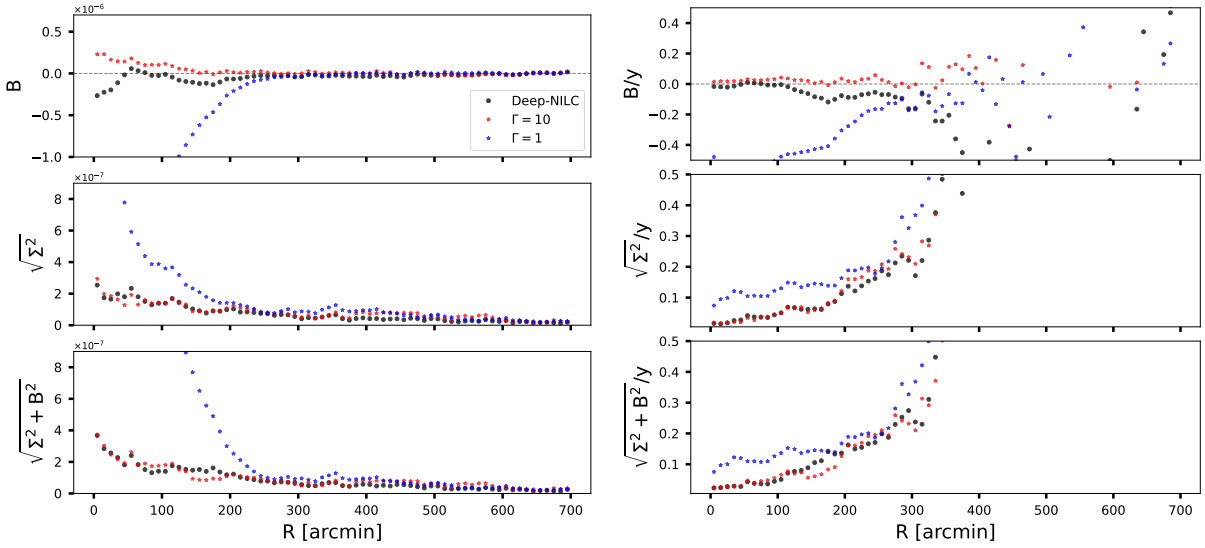


Figure 4.10 Same as Figure 4.8 but for a Virgo-like system.

CHAPTER 5

Extracting the Thermal Sunyaev–Zel'dovich Effect with a 3D Convolutional Neural Network

5.1 Abstract

The thermal Sunyaev-Zel'dovich (SZ) effect offers an independent probe of the hot and diffuse Universe that may not be easily detected by X-rays. The SZ effect could be used to help close the missing baryon problem, however, current SZ data suffer from systematic noise, making it hard to detect weak signatures. In this work, we use state-of-the-art simulations of the microwave sky, as seen by *Planck* and *WMAP*, to train a three-dimensional convolutional neural network (3D-CNN) that extracts the SZ signal. Our results show that the 3D-CNN generalized well on a set of unseen test data and yielded lower noise compared to the popular NILC method. When applied to real data, we found the variance of the 3D-CNN to be significantly larger than NILC while the opposite trend was seen for the simulated data. Both 3D-CNN and NILC yielded larger variances for the real data compared to the simulated which suggests the simulated data were too simple and not fully representative of the real sky. This shortcoming also explains why the 3D-CNN underperformed on the real sky compared to NILC. Finally, we argue that n order to do simulation-based prediction in the future, more realistic and diverse datasets are needed.

5.2 Introduction

Over the past few decades, most of our knowledge about the hot, diffuse gas that permeates our Universe has come through X-ray observations. X-rays are easily observed for massive galaxy clusters, however, they are more challenging to detect with decreasing halo mass or increasing distance from the halo center. As such, much of this gas has been elusive to

X-ray observers. It is suspected that much of the baryons in the Universe are too diffuse to observe with current X-ray observatories, and this known as the "missing baryon problem" (Bregman 2007, Shull et al. 2012).

The thermal Sunyaev–Zel'dovich (SZ) effect offers a unique view of hot and diffuse gas. It is caused by the inverse Compton scattering of cosmic microwave background (CMB) photons with free electrons in a cosmic plasma. The amplitude of the SZ effect is given by the dimensionless y parameter which is the integrated electron pressure along a line of sight

$$y \propto \int_0^\infty n_e T_e dl \tag{5.1}$$

where n_e is the electron number density, T_e is the electron temperature, and dl is the differential path length along a line of sight. On the other hand, X-ray radiation has a quadratic dependence on the electron density, $\mathrm{S_X} \propto n_e^2$, so it is less sensitive to diffuse environments. Since the SZ effect has a linear dependence on the density, it is more sensitive to low-density gas. Therefore, in theory, the SZ effect can be an effective tool for capturing the remainder of the missing baryons.

Extracting the SZ effect from real observations, however, is a challenging task. It is quite weak compared to other galactic and extragalactic signals appearing in the radio/infrared bands, causing a distortion to the CMB temperature on the order of $\frac{\Delta T}{T} \lesssim 10^{-4}$ which is for the strongest signals coming from the most massive clusters of galaxies (Cavaliere et al. 1991). Observations from *WMAP* and *Planck* amount to a mixture of photons coming from many different physical sources. In order to extract the SZ signal, one must solve an unmixing problem that separates the SZ component from all other signals.

A number of techniques have been built to address component separation problems, and many were developed to extract the CMB. One of the best methods is known as the *needlet internal linear combination* (NILC; Cardoso et al. 2008, Delabrouille et al. 2009, Remazeilles et al. 2011). NILC is a semi-blind extraction that aims to minimize the variance of the reconstructed SZ map (y-map) while preserving the spectral dependence of the SZ effect. It also assumes zero correlation between the SZ effect and all other components which, empirically, is untrue. Despite this limitation, it has shown to be very effective for SZ studies (Planck Collaboration et al. 2016b, Pratt et al. 2021, Bregman et al. 2022, Chandran et al. 2023, McCarthy & Hill 2024).

More recently, neural networks (NNs) have migrated into this field in hopes of offering improvements. This has come with the continual progression of computing resources that can train large nonlinear models on big datasets. For example, the authors of Pratt et al. (2024) implemented a NN pipeline to enhance the quality of NILC extractions. Similar

concepts were applied by McCarthy et al. (2024) where these authors used a NN to calculate a correction factor that was then combined with a traditional ILC solution to reduce the noise in the reconstructed y-maps. Also, the authors of Guzman & Meyers (2022) developed a convolutional neural network (CNN) to extract the CMB polarization.

Deep learning models are often trained using supervised learning on simulated data. Gathering robust sets of simulated data, however, have only recently become available. In this work, generate a set of mock observations that would be seen by *WMAP* and *Planck* satellites. We then use these data to train a three-dimensional CNN (3D-CNN) that extracts the SZ signal. Finally, we use it to predict y-map patches of the real sky.

The rest of the paper is structured in the following way: in section 5.3 we present the methodology, the main results are presented in section 5.4, which are discussed in section 5.5, and a summary is provided in section 5.6.

5.3 Methods

The SZ effect is just one of many components that causes an observable signal near the CMB frequencies ($\sim 23 - 857$ GHz). However, there are other astrophysical (Galactic and extragalactic) and instrumental components that produce non-trivial signals at these same frequencies. In this section, we describe the set of simulated data used to create mock observations of the sky as seen by *WMAP* and *Planck*.

A total of 100 independent realizations were produced from 23-353 GHz. We excluded the highest frequencies 545 GHz and 857 GHz bands as has been done by others to mitigate the effects of dust and strong IR sources (e.g., Planck Collaboration et al. 2016c). It was also found that omitting these data helped stabilize training. We split the data such that 80 were used for training and 20 for testing. Furthermore, one of the test maps was designated to make comparisons between NILC and the 3D-CNN. Finally, 3D-CNN was used to extract SZ patches of the real sky.

5.3.1 Simulations

5.3.1.1 Physical Components

The simulated data used in this work were very similar to those used by Pratt et al. (2024). These authors utilized the Planck Sky Model software in Python (Thorne et al. 2017; PySM) to generate emission models of the foreground components. An important caveat of their study was the implementation of only a single foreground model. We expanded this and generated multiple realizations using PySM. Specifically, we produced different realizations

of the thermal dust and synchrotron components with random small-scale fluctuations in the spatial and spectral dimensions. Other components, such as CO line emission, were not included because PySM does not currently have the capability to feasibly generate randomized signals. This is an important caveat which we discuss further in section 5.5.

Extragalactic components were added using data products from Han et al. (2021). Similar to Pratt et al. (2024), y-maps were derived from their 148 GHz maps and using the known spectral dependence of the thermal SZ signal

$$\frac{\Delta T}{T_{\rm CMB}} = g(\nu) y \tag{5.2}$$

where $g(\nu)$ is the SZ spectral dependence, $\frac{\Delta T}{T_{\rm CMB}}$ is the change in temperature relative to the CMB. In addition, we used their radio, infrared, and CMB maps. These were important because they included physically and spatially correlated components. An example of a correlated source is a galaxy cluster hosting an AGN that produces both strong radio and SZ signals.

The authors of Han et al. (2021) released publicly available maps of the different extragalactic components at six different frequencies. They are publicly available in Healpix format (Górski et al. 2005) with a resolution parameter NSIDE= 4096, but we downgraded them to NSIDE= 2048 to reduce computational expenses without compromising performance. These data were then used to estimate continuous emission models for the IR and radio sources. For the IR sources, we fit a double power law to the frequency data, and for the radio sources, we fit a single power law. Although arbitrary, they provided simple approximations for the emission laws of these components.

Some of these fits yielded unrealistically large positive/negative values. Moreover, outliers can be troublesome for machine learning models when the range of data values are except large. To overcome this, we set upper/lower limits to the simulated data, truncating any simulated values to be no more than ten times the maximum values seen in PR3 and WMAP.

5.3.1.2 Instrumental Component

Instrumental effects were also considered. Each frequency map was smoothed using a Gaussian beam defined by its full-width at half-maximum (FWHM; Jarosik et al. 2003, Planck Collaboration et al. 2014b). The convolution was done in pixel-space to avoid high-frequency noise arising from transforming strong point sources into harmonic space. Gaussian noise was also included to make realistic mock observations. The noise power spectrum is given by

$$C_\ell = \Omega \sigma^2 \tag{5.3}$$

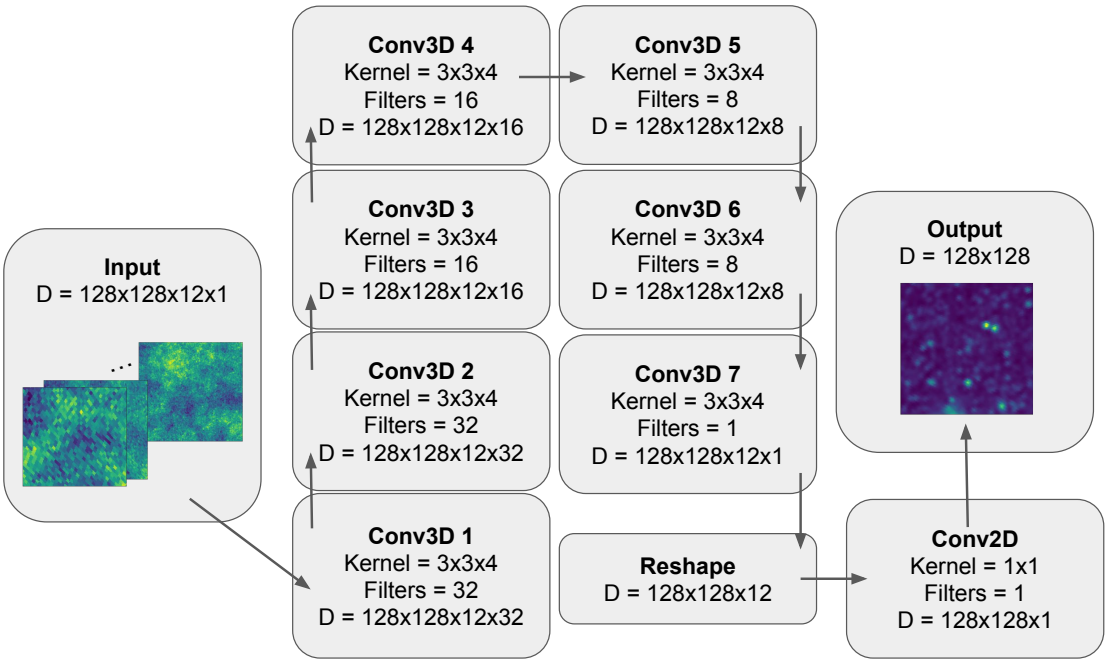


Figure 5.1 Flowchart describing the 3D-CNN architecture. D represents the dimension of the output after passing through that layer. The first two dimensions were always 128x128 since padding was the same for all layers. For the 3D layers, the third dimension remained at 12 which represents the number of spectral bands, and the fourth dimension represented the number of feature channels. A leaky ReLU activation function was also applied at the end of each 3D convolution layer; a linear activation was used for the output, which comes from the 2D point-wise convolution.

where Ω is the solid angle covered by a pixel in units of radians^2, and σ is the variance per pixel. For *WMAP* data, values of Ω and σ were taken from Table 2 in Jarosik et al. (2003); the same relevant information for Planck can be found in Table 1 of McCarthy & Hill (2024).

Frequency [GHz]	**Standard Deviation [$\mathbf{K_{CMB}}$]**
23	0.0001828
30	0.0001457
33	0.0001124
41	0.0001010
44	0.0001154
61	0.0001018
70	0.0001156
94	0.0001066
100	0.0001147
143	0.0001105
217	0.0001599
353	0.0008577

Table 5.1 Standard deviation values of the real frequency data that were used as normalization factors to the input data.

5.3.2 Modeling

5.3.2.1 Train/Test Data

The next step was to turn the simulated data described above into a set of training and test data. Before training, we scaled the input and output data to help stabilize the gradient descent process. For the output data, we divided the y-maps by 10^{-6} in order to bring the range of values closer to unity. The input data were divided by the standard deviation of the real frequency maps where $|b| > 20^\circ$ as given in Table 5.1. This was particularly important for the 353 GHz data which exhibited a range in values almost an order of magnitude larger than the lower frequencies. In many deep learning applications, it is customary for the inputs and outputs to also have zero mean in addition to unit variance, however, we found that subtracting the mean did not have much effect.

Each training example consisted of a 128x128x12 multispectral image cube i.e., 128 pixels for the spatial dimension and 12 channels in the spectral dimension. For the 3D convolutional layers, the last dimension represented the number of feature channels; this was dropped in the "Reshape" layer before the point-wise convolution. The 2D patches were created using the Gnomonic projection in Healpy (Zonca et al. 2019). For each of the 100 full-sky realizations, we selected 250 random patches on the sky under the condition of $|b| > 20^\circ$, which provided

sufficient sampling of the full-sky map.

Each patch was generated with pixel sizes ranging from of $\frac{2}{3} - 2$ arcminutes per pixel. These were drawn from a half-Gaussian centered at 2 arcminutes and truncated at 2/3 arcminutes. The idea was to generate most images with resolutions close to 2 arcminutes per pixel, but a few were more zoomed in. This was done to help avoid over-fitting to point sources since most SZ signals are unresolved by *Planck* and *WMAP*. By changing the pixel size in some of the examples, we were able to show the network more cases of resolved signals. Lastly, an 80:20 split was used for the training and test data respectively; one map from the test set was designated for comparisons with NILC.

5.3.2.2 Architecture

The model architecture, shown in Figure 5.1, consisted of a seven layer 3D-CNN followed by a 2D point-wise convolution. Each of the 3D convolutional layers generated four-dimensional tensors of shape (128x128x12xN_f) where N_f is the number of feature channels for a given layer. Each layer utilized the same 3D kernel of 3x3x4 i.e., 3x3 for the spatial and 4 in the spectral. The output from the convolutions then went through a leaky ReLU activation function, which is known to be helpful against the vanishing gradient problem (Xu et al. 2015). Finally, we used the Adam optimizer with an initial learning rate of 0.0005 and a batch size of 64.

The basic idea behind our chosen architecture was to expand the inputs and then compress the information back into its original shape. One can imagine the initial expanding layers as filtering/capturing different types of spatial-spectral signatures coming from various sources. Once condensed back to its original shape, the second to last layer (Conv3D 7 in Figure 5.1) can be thought of as the SZ signal at each frequency. Then the final point-wise convolution would be similar to learning the SZ spectral dependence and projecting the features into a 2D y-map. This was the motivation for our chosen architecture, however, a deep learning models is still inherently a black-box.

We chose to minimize the mean squared error MSE $= (y - \hat{y})^2$ as the loss function for training. The MSE values of the training and test sets as a function of training epoch are shown in Figure 5.2; we also show the mean absolute error MAE $= |y - \hat{y}|$. The MSE is a common metric used in regression problems that imposes large penalties for outliers. Different loss functions, however, can be tailored to solve unique problems. We discuss the implications of this in section 5.5.

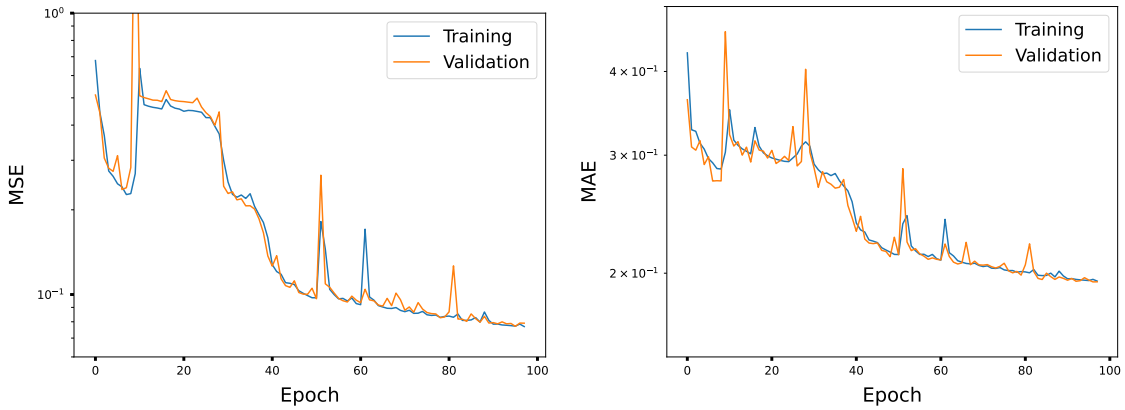


Figure 5.2 The top panel shows the MSE for both the training set (blue) and the test set (orange) as a function of training epoch. The MSE was used as the training loss function. The bottom panel shows the same as the top panel but for the MAE. These plots demonstrate that training was able to eventually converge in both metrics.

5.3.2.3 Simulation-Based Prediction of the Real Sky

The overall goal of training our model with simulated data was to eventually apply it to real data for prediction. To do this, we used the third release of *Planck* data (Planck Collaboration et al. 2020a) and the nine-year *WMAP* data (Bennett et al. 2013). These data were normalized using the values in Table 5.1 and then cut into square patches with $2'$ pixels using the Gnomonic projection.

5.4 Results

In this section, we present the main results. First, we focus on the quality of the 3D-CNN and NILC extractions using the test set of simulated data. Then we compare the results from applying these methods to the real sky.

5.4.1 Performance on Test Data

In Figure 5.2, we show the MSE and MAE metrics throughout the training process. The training loss (MSE) exhibited unstable behavior at the beginning, but was able to start converging after $\sim$ 30 epochs. This was also manifested in the MAE, which is a measure more sensitive to archetypal changes, whereas the MSE better captures outlier behavior.

In Figure 5.3 we provide a single example of the models performance on a random patch of simulated sky. The left and right columns show the results from the NILC and NN extractions, respectively. Following the work of Pratt et al. (2024), the NILC data were

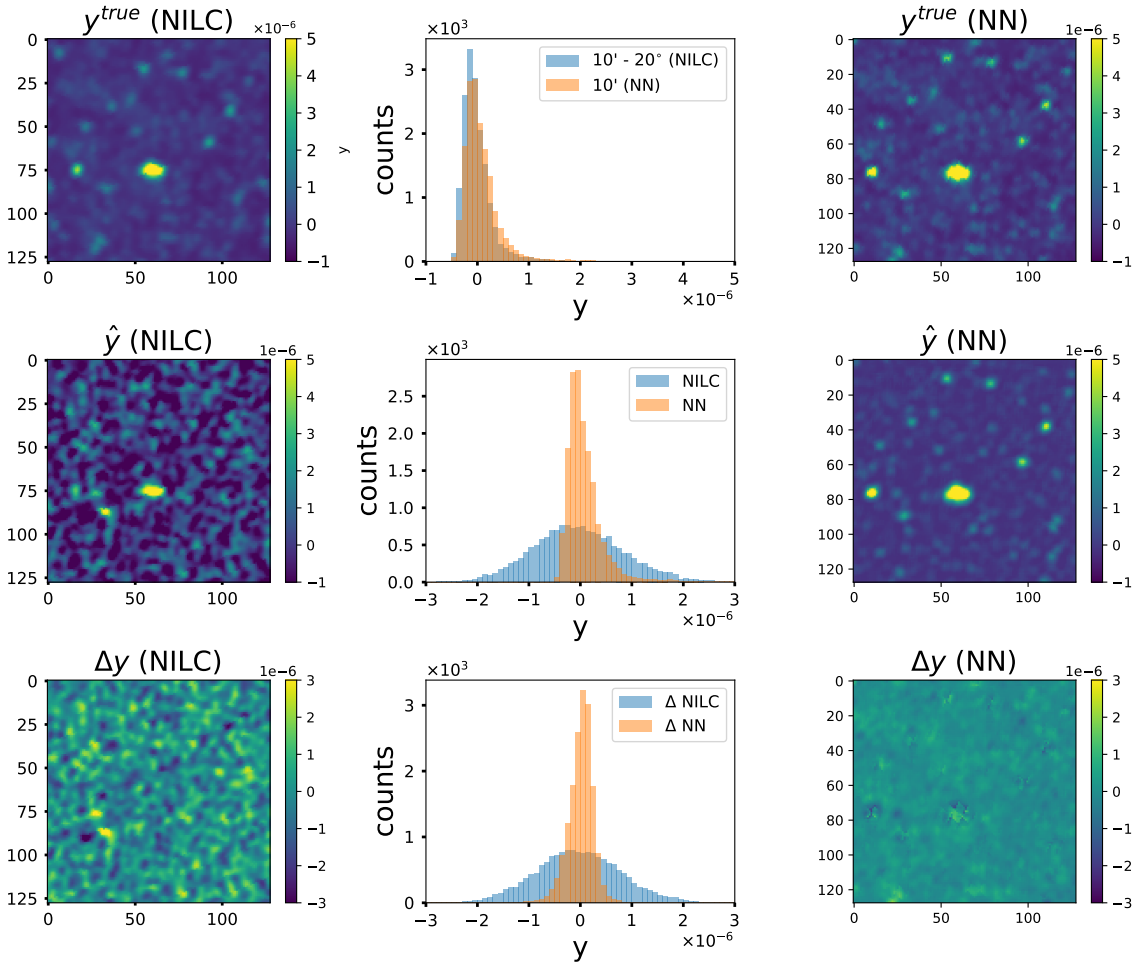


Figure 5.3 An example of the extraction for a random patch of sky in the test set ($l = 96.1°$, $b = -59.6°$). The left column presents data from the NILC extraction, and the right column is that for the NN. The middle column shows the distribution of pixel values for the respective rows. The top row shows the true values i.e., the SZ signal that was input to the simulations. The NILC pixel values are represented by the blue histograms while the NN data are shown in orange. In order to compare the two different extractions, we subtracted their median values to center the distribution around zero. The second row shows the results from the NILC and 3D-CNN predictions, and the last row shows the residuals between the input y-map and the recovered y-map.

filtered with Gaussian kernels. The point spread function was roughly a Gaussian with fwhm=10′ and there was no signal on scales larger than 20°. On the other hand, the NN data retained large-scale information, so every patch of the sky contained its own background level. In Figure 5.3, the median values of y^{true} and $\hat{y}$ were subtracted to flatten the background and make the data more comparable to those of NILC.

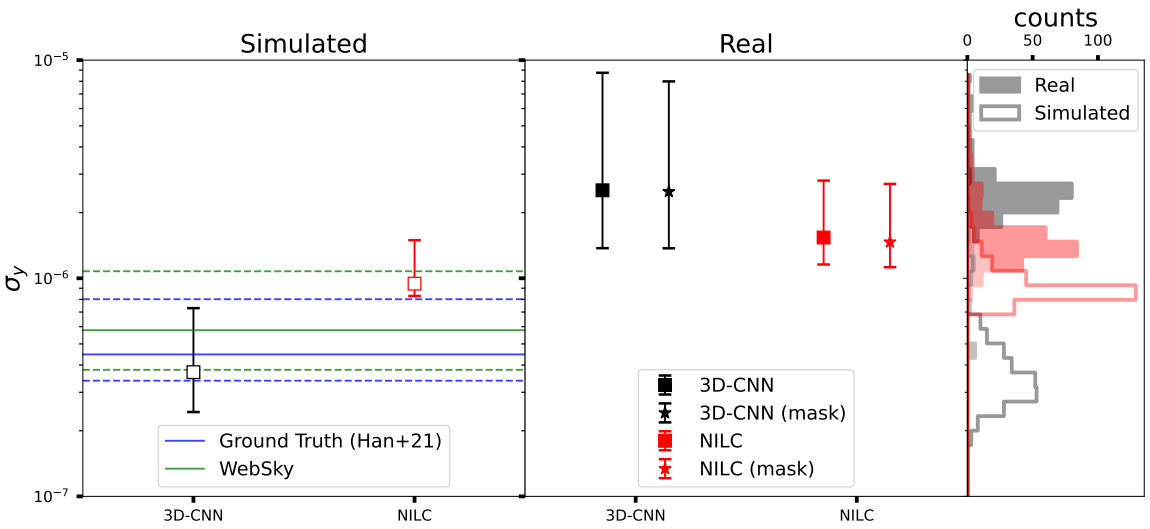


Figure 5.4 Statistical evaluations of the NILC and 3D-CNN methods. The left panel shows the results for 250 patches using one of the full-sky test maps. The solid blue line shows the median variance and the dashed blue lines denote the 5%-95% spread of the pixels in the ground truth map; the same is shown in green for the WebSky simulations. The squares and error bars show the same statistics but for the recovered y-maps. The middle panel shows the same as the left but for real data. Stars represent the calculated σ_y values after masking known galaxy groups and clusters. We do not show horizontal lines in the middle panel since we do not know the ground truth. In the right panel, the open histograms show the distributions of simulated data, and the filled represent the real data.

5.4.2 Performance on Real Data

We applied both the NILC and 3D-CNN algorithms on the real sky using PR3 and *WMAP* data, and compared them with the results of the test map described above. For simplicity, we extracted square patches centered around the same 250 coordinates used in the simulated data (250 locations). The main results are shown in Figure 5.4.

The standard deviation of each patch, σ_y, was calculated to be the metric of statistical comparison. Open points represent σ_y for the simulated data while the filled ones denote the real sky. The squares mark the median values of each distribution, and the error bars show the $5\% - 95\%$ range of the data. Stars show the same results but after masking known galaxy clusters in the second *Planck* SZ catalog (Planck Collaboration et al. 2016a) and all-sky X-ray catalog (Piffaretti et al. 2011). The full distributions are plotted as histograms in the right panel following the same open/filled scheme.

In the left panel, the blue lines show the distribution of σ_y taken from the ground truth y-map using data Han et al. (2021). This gives a sense of how much intrinsic variance is expected to be present in a realistic y-map. In green, we show the same y-map values but

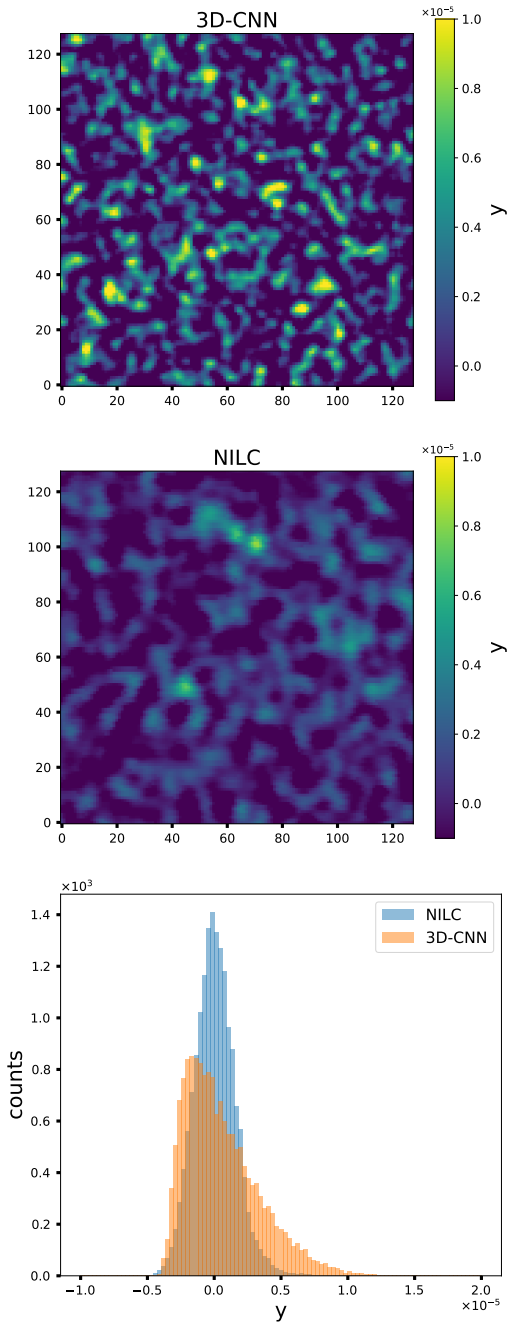


Figure 5.5 Example 2D cutouts for the 3D-CNN and NILC extractions of the real sky. The field was randomly selected and centered around the Galactic coordinates of $l = 227.61°, b = 53.52°$. A few known galaxy clusters are present in this field which were identified in all-sky X-ray and SZ catalogs (Piffaretti et al. 2011, Planck Collaboration et al. 2016a) at pixel positions near (x=60,y=100) and (x=45,y=50).

from the WebSky simulations (Stein et al. 2020) which were also smoothed to a resolution of 10'. The purpose of including WebSky values was to show an independent estimation of

the intrinsic fluctuations caused by SZ sources. To be clear, we did not apply the 3D-CNN or NILC algorithms to WebSky data.

The 3D-CNN yielded values of σ_y typically below the ground truth. These results also compliment those presented in Figure 5.3. Looking at y^{true} (NN) and $\hat{y}$ (NN), the weak SZ signals in y^{true} were not recovered nearly as well as the strong signals. Smaller variances were observed in $\hat{y}$ since power was suppressed from weak signals. On the other hand, opposite results were seen for NILC where $\hat{y}$ yielded larger values of σ_y compared to the ground truth. The residuals for NILC also appeared larger than for 3D-CNN, suggesting it did not perform as well as 3D-CNN on the test data.

Next, we highlight the differences seen between the real and simulated panels. The most prominent difference was the 3D-CNN method yielded a median σ_y much larger on the real data compared to simulated data. The spread of the inner 90% of the pixel values appeared larger as well. For NILC, the simulated and real σ_y values were much closer to each other. They also appeared significantly above the ground truth of the simulations. The implication of these results are discussed in section 5.5.

Very little difference was seen between the masked and unmasked σ_y values for the real sky, suggesting the σ_y values were mainly caused by the systematic uncertainties inherent to each method. This meant the fluctuations coming from known SZ sources hardly affected the estimation of σ_y for real data. Thus, the differences in σ_y between the simulated and real panels cannot be explained by a simple underestimation of SZ power in the simulations.

A visual example for a random field of the real sky using the two methods is shown in Figure 5.5. Again, their median values were subtracted and their pixel distributions are shown as histograms in the bottom panel. The goal of this figure is to give a visual sense of the increased fluctuations in 3D-CNN compared to NILC.

5.5 Discussion

Here we discuss the possible causes for the features seen in Figure 5.3, Figure 5.4, and Figure 5.5. We argue the main differences seen between NILC and 3D-CNN for the simulated/real data are due to the inherent nature of each method. Finally, we point out how the results also depend on the quality of simulated data used in this work.

We first consider the expected differences between the simulated and real data. The simulations used in this work were made to mimic real physical emissions and instrumental effects. At the end of the day, however, simulated data cannot perfectly represent real data due to the innate simplifications. To point out a few examples: dust emission was modeled with a modified black body function, radio sources were fit with a power law, and

instrumental noise was assumed to be Gaussian. In reality, each of these are probably more complex. Another simplification was the omission of certain physical components such as CO line emission and free-free radiation which are additional sources of contamination. Because simulated data are simplified compared to the real sky, they will always yield lower noise extractions.

5.5.1 NILC

The NILC results provide support for the statement above. As a reminder, NILC relied on the strong assumption that the SZ signal was uncorrelated with sources of contamination. This assumption was certainly untrue as empirical correlations always exist, and adding more contaminants will introduce more noise. This is why we saw elevated values of σ_y in the real data compared to the simulated data. If the simulated data perfectly represented the real data then one should not observe any significant offset between the red squares seen in the left and middle panels of Figure 5.4.

Also, the NILC σ_y values for the real and simulated data both resided above the variations predicted by the ground truth from the simulations. This tells us the systematic uncertainties from the NILC method were larger than the expected fluctuations caused by the underlying SZ distribution.

5.5.2 3D-CNN

The results of 3D-CNN were quite different than NILC. We attribute most of this to the effect of supervised learning. Our 3D-CNN model was built to recognize features using only the training data, making 3D-CNN very highly dependent on the quality of simulated data. Therefore, any changes made to the simulation data could lead to systematic variations in the extraction.

The best evidence for the presence of systematic uncertainties in 3D-CNN is the difference between σ_y for the simulated and real data. In the left panel of Figure 5.4, we pointed out the observed σ_y was similar to that of the ground truth, but the results for the real sky were significantly larger both in the median and spread. If the simulated data were perfectly representative of the real sky, then one would not expect to see any significant differences. The observed contrast signified the simulations did not manifest the same level of complexity as real data.

Looking at Figure 5.2, the training curve for the unseen test data seemed to converge along with the training. This showed that the model was not over-fitting to the training set and was able to generalize well to the test set. However, the model likely over-fit to the

simulated data as a whole given the larger σ_y values in real data. NILC did not yield as large of a difference between the simulated and real data due to the blind nature of the algorithm. In conclusion, this trend was caused by the fact 3D-CNN was fully reliant on the simulated data while NILC was not.

One could mitigate this effect by considering a validation set—an independent, realistic test set from the training/test data. This was not feasible in this work as the generation of mock observations were quite limited. As previously mentioned, we could only generate robust simulated datasets using a few physical components. Furthermore, each of them were modeled in a similar and simplified fashion for every realization. In the future, we need software with more elaborate modeling of the non-SZ components as well as the inclusion of more contaminating sources. This was not possible with the current publicly available tools. Improvement on this front will certainly lead to better results for simulation-based prediction.

Rather than wait for new simulations, it may be possible to incorporate the real sky into the training process, such as adding a term to the loss function. For example, one could minimize a loss function that is a linear combination of the MSE and the variance of the real sky. However, this could be tricky since we do not know the true underlying variance of the real SZ sky. This would require careful tuning when weighting each term. Perhaps more elaborate loss functions could be constructed to achieve a similar goal.

5.6 Summary

The main goal of this work was to build a simulation-based prediction model for the thermal SZ effect. To do this, we trained a 3D-CNN with supervised learning on mock observations of the microwave sky. Obtaining robust simulated data was done using the PySM software as well as the data products provided by Han et al. (2021). PySM created spatially and spectrally varying emission models for thermal dust emission as well as Galactic synchrotron emission. The data from Han et al. (2021) allowed us to incorporate spatially correlated extragalactic signals, which was an important step toward more realistic data. Simple models were used to describe the emission laws of the physical components, and calculated band-averaged frequency maps as seen by the *Planck* and *WMAP* satellites.

With these data, we extracted the SZ signal using the semi-blind NILC method as well as using a trained 3D-CNN. The same was done with the real sky data to evaluate the systematic differences. Our main findings are as follows:

1. We generated a robust set of simulated data using publicly available tools, and used these to train a 3D-CNN with supervised learning. The model was able to converge

and generalize well to an unseen test set.

2. We evaluated the performances of our 3D-CNN and the NILC method using both simulated and real data. The variances plotted in Figure 5.4 show the amount of variance expected from simulations as well as the reconstructed variances. Both NILC and 3D-CNN exhibited larger variances when applied to real data. We argued this was due to the simulated data lacking the complexity needed to describe the real sky.

3. The variances of the real sky were much larger for the 3D-CNN compared to NILC. Similar to the point above, we claimed this increase was because the 3D-CNN was completely reliant upon the simulated data.

4. The 3D-CNN performed better on the simulated data compared to NILC, however, its larger variance in the real was concerning and should be used with caution.

We conclude by noting some areas where there could be immediate improvements. First, the 2D cutouts used for training/testing were no larger than $\sim 4^\circ \times 4^\circ$ which set a maximum angular size one could study. In the future, more training data should be developed in order to capture SZ signals on scales of a few degrees. Second, a method should be developed such that it can be applied to the entire real sky.

As already mentioned, an independent validation set of data should be introduced to evaluate any potential over-fitting to the current train/test set. We believe the data used for this project were gathered in the best way currently possible. Nevertheless, these data were simplified and certainly not perfect representations of the real sky. In order for simulation-based prediction to be applied we need more realistic mock data.

Lastly, we want to emphasize the most significant advances will be made in the advent of new observations with higher spectroscopic sampling. The biggest challenge when separating the SZ signal from other components is caused by the varying emission laws. More spectral coverage will provide essential information regarding the amount of presence a particular component may have on the SZ spectral signature.

In support of reproducible results, we provide code for this project at `https://github.com/campratt/multispectral/sz`.

CHAPTER 6

Summary and Future Work

6.1 Summary

This thesis focused on the study of hot and diffuse gas around collapsed structures primarily through the SZ effect. In Chapter 1, we presented the physical basis of the SZ effect and its potential for an effect probe of hot halos. The SZ effect yields a mass-weighted ($\propto n$) measure of hot gas while X-rays provide an emission-weighted measure ($\propto n^2$). Given the weaker dependence on density, the SZ effect may help us detect more diffuse baryons—those suspected to be the culprit of the missing baryon problem.

Much of the missing baryons are presumed to reside around the outskirts low-mass halos, particularly galaxies and galaxy groups. Galaxy clusters appear to retain most of their baryons near the virial radius, but the baryon fraction for lower mass halos likely reaches the cosmic prediction happens at much larger distances (Ayromlou et al. 2023). It has been postulated that AGN feedback is responsible, however, we are still missing crucial observational constraints to fully illustrate this scenario.

One of the proposed observational signatures of AGN feedback is the disruption of various scaling relations. Because AGN feedback pushes gas away from the gravitational potential, the X-ray and SZ observables are expected to be reduced within the virial radius (Paul et al. 2017, Farahi et al. 2018). It is also predicted that scaling relations should produce more scatter at lower masses where these systems can exist over a wide range of dynamical states. Most scaling relation investigations have been done using X-ray observations (Pratt et al. 2009, Lovisari et al. 2015), but very little has been done with the SZ effect.

6.1.1 X-ray and SZ Scaling Relations with Low-mass Systems

The first chapter of this thesis focused on the X-ray and SZ scaling relations of galaxy groups and clusters near the North Ecliptic Pole (NEP). The goal of this project was to provide the first SZ scaling relations with individual low-mass objects. Normally, low-mass objects are

not easily detected with the current noise levels in SZ data. However, the NEP is a unique region of the sky where both the *Planck* and *ROSAT* achieved their deepest observations, leading to lower noise levels. In addition, there exists robust multi-wavelength coverage of the NEP, making it a prime section of the sky to study scaling relations. Using archival X-ray and optical data, as well as our SZ extractions of the public NILC y-map (Planck Collaboration et al. 2016b), we obtained scaling relations for 62 groups and clusters Henry et al. (2006).

The main results from this project were:

- The scaling SZ and X-ray relations measured were consisted with the self-similar prediction using two different regression methods.

- Our reported SZ values add to the plethora of multi-wavelength coverage near the NEP. Also, we identified 10 strong SZ sources that were not labeled in the X-ray catalog from (Henry et al. 2006). Eight of these have been confirmed as known clusters from other observations, but 2/10 may be systems yet to be identified.

- The estimated SZ flux values within R_{500} were determined using two different profile prescriptions: (1) the universal pressure profile (UPP) for observed galaxy clusters (Arnaud et al. 2010), and (2) the pressure profile based on simulations from (Battaglia et al. 2010) (BPP). We found differences in the scaling relations based on which pressure profile was assumed. This prompted the call for measuring resolved SZ profiles to avoid assuming a fixed profile shape. This was the main motivation for the work done in Chapter 2

6.1.2 The Resolved SZ Profiles of Galaxy Groups

Considering the limitations discussed in Chapter 2, it became clear that resolved pressure profiles were needed in order to investigate the effects of AGN feedback. This prompted the work presented in Chapter 3 where we reported the first resolved SZ profiles of nearby galaxy groups. In this study, we devised an optically selected sample of 10 galaxy groups that were well-resolved by the *Planck* satellite. Next, we extracted their SZ signals using our own y-maps constructed from the most recent versions of *Planck* data and the popular NILC method. Radial profiles for each system were measured and then stacked together to increase the significance of the detection. We then fit the stacked signal with different pressure profiles and determined a model that provided the best fit.

In this study, we also incorporated simulated data to understand the fidelity of our results. Specifically, we injected known SZ signals into the *WMAP* and *Planck* frequency data at

random locations of the sky. We then recovered their SZ signals using the NILC algorithm and stacked their radial profiles. This allowed us to investigate the different sources of uncertainty and bias one should expect from stacking SZ signals from galaxy groups.

The main findings of this study were:

- The stacked radial profiles using the latest version of *Planck* data (PR4) was most consistent with the AGN 8.5 profile from Le Brun et al. (2015). Using this result we calculated a baryon fraction of $f_{b,500} \approx 0.056$ and a gas fraction of $f_{gas,500} \approx 0.038$ for galaxy groups. This value is lower than those seen in X-ray selected samples, as shown in Figure 6.1. We attribute part of this difference to the nature of the optically selected sample, since X-ray selected samples are known to be biased toward more virialized systems.

- A bump feature was detected near the virial radius for the stacked profile. This was at the $\sim 3\sigma$ level and was not seen in the stack of simulated data, suggesting it was not caused by the systematic effects of the NILC algorithm. One explanation for the origin of this feature could be from the displacement of gas due to AGN feedback i.e., gas driven from the center and piling up near the outskirts. We did a simple calculation showing the energy needed for this to happen was comparable to the mechanical energy needed to carve out X-ray cavities seen in some galaxy groups. We also considered the theory that it could be caused by other physical processes such as internal accretion shocks. Simulations predict that most of the thermal heating in galaxy group halos comes from shocked gas with low mach numbers. These are thought to dissipate much of their energy near the virial radius (Ryu et al. 2003) which may cause an enhancement in the SZ signal.

The results presented in Chapter 3 provided progress toward understanding AGN feedback in galaxy groups, but conundrums still remained. For instance, one would like to make further investigations into the bump feature seen near the virial radius. Was such an enhancement simply a statistical result from stacking a modest sized sample, or could it truly be evident in typical galaxy groups? Understanding this requires better cleaning of SZ data so that we can investigate these rather small differences in their radial profiles. This elicited the work presented in Chapter 4 and Chapter 5 where we searched for lower noise extraction methods using machine learning.

6.1.3 Improving NILC SZ Extractions with Deep Learning

In Chapter 4, we presented our first attempt to design a novel SZ extraction method. We created a hybrid technique that merged the well-known NILC algorithm with machine learn-

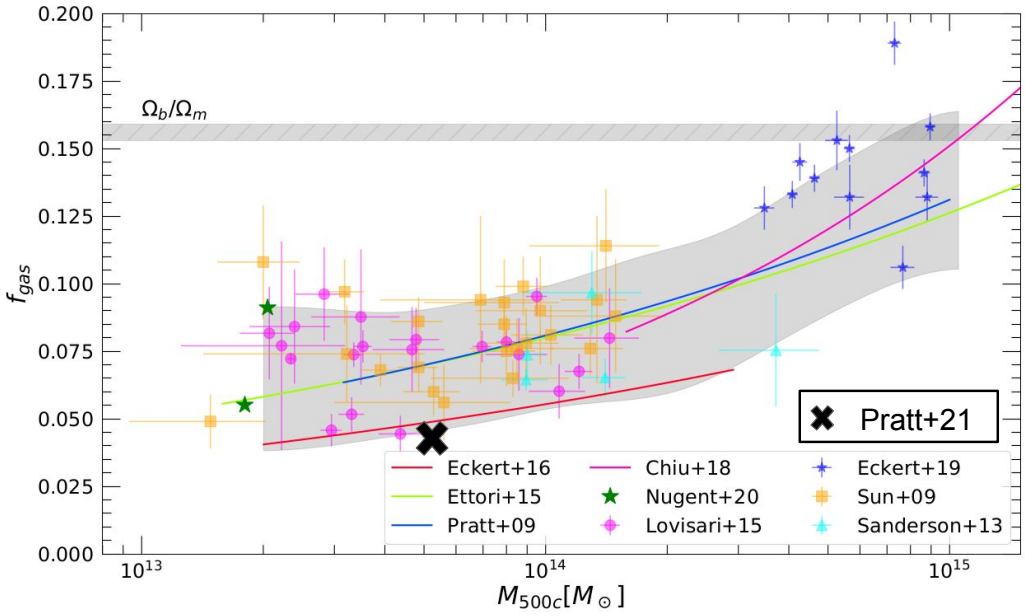


Figure 6.1 Estimated gas fractions compiled from various X-ray selected studies taken from Figure 7 of Eckert et al. (2021). The result from Pratt et al. (2021) is shown as a black cross, which lies at the lower range of X-ray values.

ing. The goal of this project was to use state-of-the-art simulated data representing the microwave sky to guide the NILC method toward a more optimized solution.

In this work, we presented a detailed review of the NILC algorithm, and specifically pointed out the necessary hyperparameters. NILC required two arbitrary hyperparameters to be defined *a priori*: the harmonic window functions ($\frac{\Delta\ell}{\ell}$) and the spatial localization parameter (Γ). The parameter space was explored for both of these, but we found the spatial localization to be the most significant.

Controlling the S/N of the SZ extraction was highly dependent on the selection of Γ. Small values of Γ were useful in the presence of strong contamination and/or weak SZ signals, while larger values of Γ worked better in the opposite scenarios. Previous works using the traditional NILC method fixed the value of Γ for the entire sky. We showed mathematically, however, that Γ should be flexible to obtain better solutions.

We took the idea of allowing Γ to vary and incorporated deep learning to improve SZ extractions. This was done by first calculating NILC solutions on simulated data over a grid of plausible Γ values. Next, these values were fed into a multilayer perceptron neural network that was trained with supervised learning. Our trained model, which we called Deep-NILC, was then able to predict the SZ value at each position on the sky. Finally, we tested Deep-NILC on a set of unseen simulations and compared the results to fixed values

of Γ.

The main results of this study were:

- Deep-NILC achieved the lowest residual power, over all angular scales, between the input and recovered y-maps compared to simply applying fixed values of Γ across the sky.
- We demonstrated that Deep-NILC provided a balance between different values of Γ. It approached the NILC solution for small Γ where the SZ signal was weak, but converged toward large Γ where the SZ signal was strong.
- Deep-NILC appeared to show the lowest total uncertainty when extracting the SZ flux for simulated signals of resolved galaxy groups. It also returned similar results to $\Gamma = 10$ for a Coma-like signal. However, its performance was inferior when considering a very extended SZ signal akin to the Virgo cluster.
- Given the statement above, we cautioned against using Deep-NILC in certain scenarios. For example, Virgo-like systems were not well-represented in the training data which was likely the reason for the poorer performance of Deep-NILC on recovering such systems. Also, the training data were known to miss other characteristics of the real sky, such as the spatial correlation between contaminating signals. This motivated some of the work done in Chapter 5 which included generating more realistic and robust simulated data.

Deep-NILC provided an interesting approach between analytical and machine learning solutions, however, it was still limited by the hyperparameters required by NILC. In theory, these arbitrary selections could be avoided by moving toward a full machine learning approach. In fact, some models like convolutional neural networks (CNNs), have proven to significantly outperform analytical solutions for a wide range of scientific problems. This was the main motivation for the work done in Chapter 5.

6.1.4 Comparison of Current NILC Extractions for Galaxy Groups

At this point, it is worthwhile to visualize the current systematic differences that exist between publicly available y-maps. Within the past couple of years, various NILC extractions have been implemented using new *Planck* data. In particular, Chandran et al. (2023) released a y-map using the same NILC algorithm used by the first public NILC y-map from Planck Collaboration et al. (2016b). This was nice because it isolated the differences caused by only

the processing of raw data. Additionally, McCarthy & Hill (2024) released y-maps using NILC while also trying to deproject certain components such as the CMB and the cosmic infrared background.

In Figure 6.2, we show the results of stacking the galaxy group sample used in Chapter 3 using six y-maps that are currently publicly available. The purpose of this figure is to give some sense of the systematic differences that exist between different SZ extraction methods. The shaded bands denote the $\pm\sigma$ range estimated for each stack. In general, the spread caused by different extractions was typically larger than the estimated statistical scatter. Thus, one should be wary of the systematic uncertainties when using different y-maps to stack the resolved profiles of galaxy groups. Unfortunately, it is very difficult to fully understand the systematic uncertainties caused by a given extraction method. All we can do is observe the variations using different methods.

The mean profile of the six methods are shown as black circles. This provides some additional insight, but it must be taken with a grain of salt. Taking the mean is not necessarily statistically appropriate since the extractions are not totally independent. As already mentioned, the extraction method used by Chandran et al. (2023) was identical to that of (Planck Collaboration et al. 2016b), where the only difference was the version of *Planck* data used. Nevertheless, the mean profile appears to be quite consistent with the Deep-NILC result. Interestingly, the bump feature near $2\mathrm{R}_{500}$ was not nearly as prominent as the results of Pratt et al. (2021) shown in green. While this observation does not prove the (non)existence of an enhanced signal near the virial radius, but it does raise suspicion as to whether or not systematic uncertainties caused a false positive signal.

6.1.5 SZ Extraction with a 3D-CNN

In Chapter 5, we presented another method for extracting the SZ signal with machine learning. Similar to the work done in Chapter 4, we created mock observations of the microwave sky as seen by the *WMAP* and *Planck* satellites. In this project, extra steps were taken to augment the simulated data and make them more realistic compared the simulations in Chapter 4. Unlike Deep-NILC, this new method did not require any data preprocessing. Also, it did not solve for the SZ signal on a pixel-by-pixel basis but rather worked on 2D patches of the sky.

We developed a 3D convolutional neural network (3D-CNN) that was built using supervised training. The input was a normalized multispectral cube of the frequency maps, and the output was the SZ signal. We chose a 3D-CNN due to its capability to capture both spatial and spectral information. Our architecture was designed to expand the inputs to

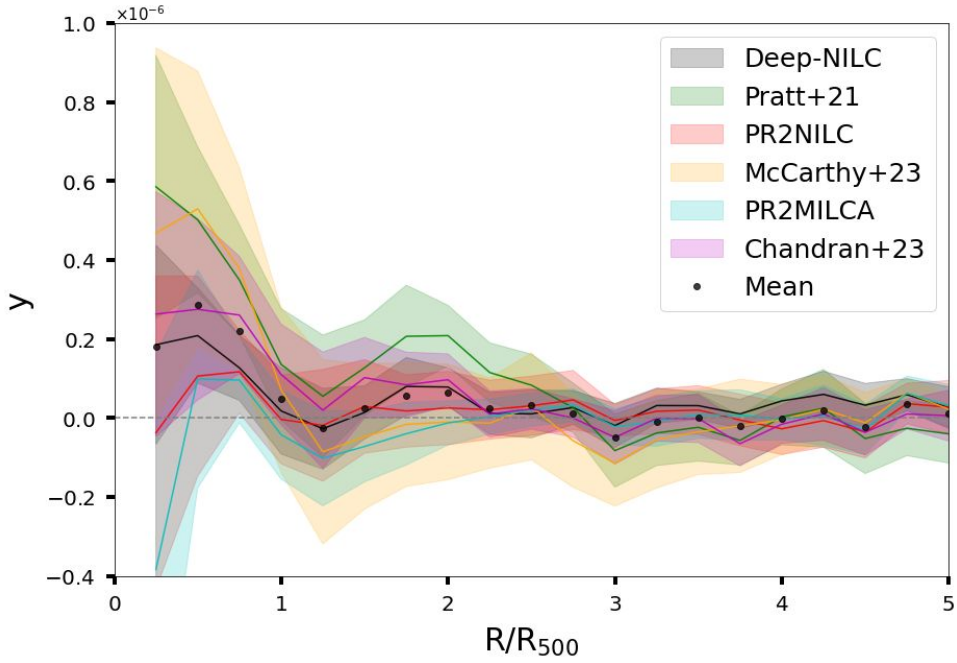


Figure 6.2 Comparison of different results for the stacked sample of galaxy groups studied in Chapter 3. Shown as shaded bands are the results from: (black) Deep-NILC, (green) the NILC solution from Pratt et al. (2021), (red) the publicly available NILC map from Planck Collaboration et al. (2016b), (yellow) one of the results from McCarthy & Hill (2024), (blue) the MILCA solution also released by Planck Collaboration et al. (2016b), and (magenta) the NILC solution from Chandran et al. (2023). The mean of all six solutions are shown as black circles.

higher dimensions and then collapse back to the original shape of the inputs (128x128x12), and then finishing with a point-wise convolution to obtain a 2D map of the SZ effect. Finally, we applied the 3D-CNN and NILC methods to the real sky and compared their results.

Our main findings of this project were:

- Using an 80/20 split for the training/test data, we were able to confirm convergence of the model and its generalization to test data. Furthermore, the 3D-CNN was able to outperform NILC on the test data by exhibiting smaller residuals between the recovered and ground truth maps.

- We compared the variances of 3D-CNN and NILC using the simulated and real data. Both algorithms yielded variances that were larger for the real data compared to the simulations. This suggested the simulated data were likely missing and/or simplifying some of the complex physics present in the real sky.

- Given the above statement, the difference between the simulated and real results were more pronounced for the 3D-CNN method. We interpreted this as further evidence

that the simulations could not capture the intricacy of the real data. This conclusion was drawn since the 3D-CNN was built through supervised training and, therefore, was heavily dependent on the quality of simulated data. On the other hand, NILC did not know anything about the data (simulated or real) before doing the extraction. Because of its blind nature, NILC yielded smaller residuals on the real sky.

- Finally, we cautioned against using simulation-based prediction given the current state of simulated data. In the future, and in the advent of advanced simulation software, perhaps 3D-CNN could be trained with data that is more similar to the real sky.

6.2 Future Work

The overall goal of this dissertation work was to improve the current state of SZ data. The first half focused on our ability to detect hot gas around low-mass halos which are thought to contain the rest of the missing baryons. The second half presented a couple of avenues to reduce the systematic effects of component separation. Here we discuss the possible avenues for future improvements.

Perhaps the most important aspect is the need for all-sky observations with more spectral coverage. One of the main reasons for the *Planck* mission was to expand the range of observed frequencies. The reasoning for doing so was to better constrain the foreground contamination when extracting the CMB, and the same principles apply to the SZ signal. Increased spectral coverage allows one to better constrain the contaminating emission laws. In the future, one of NASA's probe class missions is the Probe of Inflation and Cosmic Origins, and its goal will be to observe the sky in 21 frequency bands from 21–799 GHz (Hanany et al. 2019). This high-frequency sampling will drastically improve our ability to reduce contamination and better study weak SZ signals.

On the other hand, this issue is less important for high-z SZ studies using large ground-based telescopes such as the *Green Bank Telescope*, *South Pole Telescope*, and the upcoming CMB-S4 at the *Simons Observatory*. For these observatories, the Galactic contamination is smoother, but extragalactic sources (e.g., background galaxies and AGNs) become more important. Ground-based studies allow for higher spatial resolution but at the cost of smaller fields of view. While they are gaining attention, they will not be able to assist in studying nearby objects which typically have the most multi-wavelength coverage.

Another area for improvement is to create better cosmological simulations. Over the years, many have been able to reproduce most of the observed characteristics of the Universe over time, but disagreements still exists between models. One way to create better simulations

would be to incorporate the constraints from more recent observations. An example would be using *eROSITA* measurements to understand the spread in hot gas fractions as a function of mass. It would also be worthwhile to search for evidence of enhanced emission near the virial radius for galaxy groups. This may now become possible with stacking given the increase in the number of galaxy groups detected in X-rays.

In Chapter 5 we generated a set of mock data using state-of-the-art software and data products currently available, however, we showed these were still insufficient to train a model for simulation-based prediction. In the future, we need to improve upon the generation of more realistic mock observations. This includes better modeling both for the Galactic foreground emissions and the extragalactic components. One path toward achieving this goal would be to use generative adversarial networks (GANs) to create training data that is more representative of the real sky. Unfortunately, GANs can be difficult to train and may not yield reliable results.

A better direction would be to somehow include real data into the training process. This is also challenging because of two reasons: we do not know the ground-truth of the SZ signal and the sample size is limited given the fact we only observe one Universe. One possibility would be to include information obtained by X-ray telescopes, but this could lead to a biased result since X-ray bright sources are typically virialized and/or massive systems. Also, this would not yield a truly independent measurement of the hot gas which is arguably the most powerful aspect of using the SZ effect. Another path would be to evaluate statistical metrics of the real sky during training. One example would be to minimize the total variance shared between the validation set from the simulated data with that of the real sky. Thus, the loss function would be a linear combination of these two values with the coefficients being tunable hyperparameters.

Finally, there should be continuous efforts to develop new component separation methods. Most previous work has focused on analytical techniques, however, more attention is now being given to machine learning approaches. Machine learning has been deployed to do component separation in other disciplines of science, such as remote sensing (Ji et al. 2018), which could be transferable to SZ studies.

BIBLIOGRAPHY

Adam, R., Hahn, O., Ruppin, F., et al. 2018, A&A, 614, A118, doi: 10.1051/0004-6361/201731950

Akritas, M. G., & Bershady, M. A. 1996, ApJ, 470, 706, doi: 10.1086/177901

Andersson, K., Benson, B. A., Ade, P. A. R., et al. 2011, ApJ, 738, 48, doi: 10.1088/0004-637X/738/1/48

Andreon, S. 2010, MNRAS, 407, 263, doi: 10.1111/j.1365-2966.2010.16856.x

Arnaud, M., Pratt, G. W., Piffaretti, R., et al. 2010, A&A, 517, A92, doi: 10.1051/0004-6361/200913416

Ashdown, M. A. J., Baccigalupi, C., Balbi, A., et al. 2007, A&A, 467, 761, doi: 10.1051/0004-6361:20065829

Ayromlou, M., Nelson, D., & Pillepich, A. 2023, MNRAS, 524, 5391, doi: 10.1093/mnras/stad2046

Balogh, M. L., Mazzotta, P., Bower, R. G., et al. 2011, MNRAS, 412, 947, doi: 10.1111/j.1365-2966.2010.17957.x

Battaglia, N., Bond, J. R., Pfrommer, C., Sievers, J. L., & Sijacki, D. 2010, ApJ, 725, 91, doi: 10.1088/0004-637X/725/1/91

Baxter, E. J., Adhikari, S., Vega-Ferrero, J., et al. 2021, MNRAS, 508, 1777, doi: 10.1093/mnras/stab2720

Behroozi, P. S., Wechsler, R. H., & Conroy, C. 2013, ApJ, 770, 57, doi: 10.1088/0004-637X/770/1/57

Bell, E. F., McIntosh, D. H., Katz, N., & Weinberg, M. D. 2003, ApJS, 149, 289, doi: 10.1086/378847

Bennett, C. L., Larson, D., Weiland, J. L., et al. 2013, ApJS, 208, 20, doi: 10.1088/0067-0049/208/2/20

Bhattacharya, S., Di Matteo, T., & Kosowsky, A. 2008, MNRAS, 389, 34, doi: 10.1111/j.1365-2966.2008.13555.x

Birkinshaw, M. 1999, PhR, 310, 97, doi: 10.1016/S0370-1573(98)00080-5

Birkinshaw, M., Hughes, J. P., & Arnaud, K. A. 1991, ApJ, 379, 466, doi: 10.1086/170522

Bobin, J., Moudden, Y., Starck, J. L., Fadili, J., & Aghanim, N. 2008, Statistical Methodology, 5, 307, doi: 10.1016/j.stamet.2007.10.003

Bobin, J., Sureau, F., & Starck, J.-L. 2015, arXiv e-prints, arXiv:1508.07131, doi: 10.48550/arXiv.1508.07131

Bonamente, M., Joy, M., LaRoque, S. J., et al. 2008, ApJ, 675, 106, doi: 10.1086/525517

Bregman, J. N. 2007, ARA&A, 45, 221, doi: 10.1146/annurev.astro.45.051806.110619

Bregman, J. N., Anderson, M. E., Miller, M. J., et al. 2018, ApJ, 862, 3, doi: 10.3847/1538-4357/aacafe

Bregman, J. N., Hodges-Kluck, E., Qu, Z., et al. 2022, ApJ, 928, 14, doi: 10.3847/1538-4357/ac51de

Burns, J. O., Skillman, S. W., & O'Shea, B. W. 2010, ApJ, 721, 1105, doi: 10.1088/0004-637X/721/2/1105

Cardoso, J.-F., Le Jeune, M., Delabrouille, J., Betoule, M., & Patanchon, G. 2008, IEEE Journal of Selected Topics in Signal Processing, 2, 735, doi: 10.1109/JSTSP.2008.2005346

Carlstrom, J. E., Holder, G. P., & Reese, E. D. 2002, ARA&A, 40, 643, doi: 10.1146/annurev.astro.40.060401.093803

Casas, J. M., Bonavera, L., González-Nuevo, J., et al. 2022, A&A, 666, A89, doi: 10.1051/0004-6361/202243450

Cavaliere, A., Menci, N., & Setti, G. 1991, A&A, 245, L21

Chandran, J., Remazeilles, M., & Barreiro, R. B. 2023, MNRAS, 526, 5682, doi: 10.1093/mnras/stad3156

Dai, X., Bregman, J. N., Kochanek, C. S., & Rasia, E. 2010, ApJ, 719, 119, doi: 10.1088/0004-637X/719/1/119

Danforth, C. W., & Shull, J. M. 2005, ApJ, 624, 555, doi: 10.1086/429285

Davé, R., Katz, N., & Weinberg, D. H. 2002, ApJ, 579, 23, doi: 10.1086/342706

Delabrouille, J., & Cardoso, J. F. 2007, arXiv e-prints, astro. https://arxiv.org/abs/astro-ph/0702198

Delabrouille, J., Cardoso, J. F., Le Jeune, M., et al. 2009, A&A, 493, 835, doi: 10.1051/0004-6361:200810514

Delabrouille, J., Betoule, M., Melin, J. B., et al. 2013, A&A, 553, A96, doi: 10.1051/0004-6361/201220019

Donahue, M., & Voit, G. M. 2022, PhR, 973, 1, doi: 10.1016/j.physrep.2022.04.005

Dopita, M. A., & Sutherland, R. S. 2003, Astrophysics of the diffuse universe, doi: 10.1007/978-3-662-05866-4

Driver, S. 2021, Nature Astronomy, 5, 852, doi: 10.1038/s41550-021-01441-w

Eckert, D., Gaspari, M., Gastaldello, F., Le Brun, A. M. C., & O'Sullivan, E. 2021, Universe, 7, 142, doi: 10.3390/universe7050142

Eckmiller, H. J., Hudson, D. S., & Reiprich, T. H. 2011, A&A, 535, A105, doi: 10.1051/0004-6361/201116734

Eriksen, H. K., Banday, A. J., Górski, K. M., & Lilje, P. B. 2004, ApJ, 612, 633, doi: 10.1086/422807

Eriksen, H. K., Jewell, J. B., Dickinson, C., et al. 2008, ApJ, 676, 10, doi: 10.1086/525277

Fabbri, R., Melchiorri, F., & Natale, V. 1978, Ap&SS, 59, 223, doi: 10.1007/BF00651052

Fabian, A. C. 2012, ARA&A, 50, 455, doi: 10.1146/annurev-astro-081811-125521

Farahi, A., Evrard, A. E., McCarthy, I., Barnes, D. J., & Kay, S. T. 2018, MNRAS, 478, 2618, doi: 10.1093/mnras/sty1179

Galloway, M., Andersen, K. J., Aurlien, R., et al. 2023, A&A, 675, A3, doi: 10.1051/0004-6361/202243137

Gaspari, M., Brighenti, F., D'Ercole, A., & Melioli, C. 2011, MNRAS, 415, 1549, doi: 10.1111/j.1365-2966.2011.18806.x

Gaspari, M., Brighenti, F., & Ruszkowski, M. 2013, Astronomische Nachrichten, 334, 394, doi: 10.1002/asna.201211865

Gaspari, M., Brighenti, F., Temi, P., & Ettori, S. 2014, ApJL, 783, L10, doi: 10.1088/2041-8205/783/1/L10

Gaspari, M., Temi, P., & Brighenti, F. 2017, MNRAS, 466, 677, doi: 10.1093/mnras/stw3108

Gaspari, M., Tombesi, F., & Cappi, M. 2020, Nature Astronomy, 4, 10, doi: 10.1038/s41550-019-0970-1

George, M. R., Leauthaud, A., Bundy, K., et al. 2012, ApJ, 757, 2, doi: 10.1088/0004-637X/757/1/2

Giodini, S., Lovisari, L., Pointecouteau, E., et al. 2013, SSRv, 177, 247, doi: 10.1007/s11214-013-9994-5

Giodini, S., Smolčić, V., Finoguenov, A., et al. 2010, ApJ, 714, 218, doi: 10.1088/0004-637X/714/1/218

Gioia, I. M., Henry, J. P., Mullis, C. R., et al. 2003, ApJS, 149, 29, doi: 10.1086/378229

Gitti, M., Brighenti, F., & McNamara, B. R. 2012, Advances in Astronomy, 2012, 950641, doi: 10.1155/2012/950641

Górski, K. M., Hivon, E., Banday, A. J., et al. 2005, ApJ, 622, 759, doi: 10.1086/427976

Guilloux, F., Fay, G., & Cardoso, J.-F. 2007, arXiv e-prints, arXiv:0706.2598, doi: 10.48550/arXiv.0706.2598

Guzman, E., & Meyers, J. 2022, JCAP, 2022, 030, doi: 10.1088/1475-7516/2022/01/030

Hallman, E. J., Burns, J. O., Motl, P. M., & Norman, M. L. 2007, ApJ, 665, 911, doi: 10.1086/519447

Han, D., Sehgal, N., & Villaescusa-Navarro, F. 2021, PhRvD, 104, 123521, doi: 10.1103/PhysRevD.104.123521

Hanany, S., Alvarez, M., Artis, E., et al. 2019, arXiv e-prints, arXiv:1902.10541, doi: 10.48550/arXiv.1902.10541

Henry, J. P., Mullis, C. R., Voges, W., et al. 2006, ApJS, 162, 304, doi: 10.1086/498749

Hill, J. C., Baxter, E. J., Lidz, A., Greco, J. P., & Jain, B. 2018, PhRvD, 97, 083501, doi: 10.1103/PhysRevD.97.083501

Holland, J. G., Böhringer, H., Chon, G., & Pierini, D. 2015, MNRAS, 448, 2644, doi: 10.1093/mnras/stv097

Hudson, D. S., Mittal, R., Reiprich, T. H., et al. 2010, A&A, 513, A37, doi: 10.1051/0004-6361/200912377

Hurier, G., Adam, R., & Keshet, U. 2019, A&A, 622, A136, doi: 10.1051/0004-6361/201732468

Hurier, G., Macías-Pérez, J. F., & Hildebrandt, S. 2013, A&A, 558, A118, doi: 10.1051/0004-6361/201321891

Ishibashi, W., & Fabian, A. C. 2016, MNRAS, 457, 2864, doi: 10.1093/mnras/stw182

Isobe, T., Feigelson, E. D., & Nelson, P. I. 1986, ApJ, 306, 490, doi: 10.1086/164359

Itoh, N., Kohyama, Y., & Nozawa, S. 1998, ApJ, 502, 7, doi: 10.1086/305876

Jansen, F., Lumb, D., Altieri, B., et al. 2001, A&A, 365, L1, doi: 10.1051/0004-6361:20000036

Jarosik, N., Barnes, C., Bennett, C. L., et al. 2003, ApJS, 148, 29, doi: 10.1086/377221

Ji, S., Zhang, C., Xu, A., Shi, Y., & Duan, Y. 2018, Remote Sensing, 10, doi: 10.3390/rs10010075

Jimeno, P., Diego, J. M., Broadhurst, T., De Martino, I., & Lazkoz, R. 2018, MNRAS, 478, 638, doi: 10.1093/mnras/sty987

Kaiser, N. 1986, MNRAS, 222, 323, doi: 10.1093/mnras/222.2.323

Keihänen, E., Kurki-Suonio, H., Poutanen, T., Maino, D., & Burigana, C. 2004, A&A, 428, 287, doi: 10.1051/0004-6361:200400060

Kettula, K., Giodini, S., van Uitert, E., et al. 2015, MNRAS, 451, 1460, doi: 10.1093/mnras/stv923

Kingma, D. P., & Ba, J. 2014, arXiv e-prints, arXiv:1412.6980, doi: 10.48550/arXiv.1412.6980

Klessen, R. S., & Glover, S. C. O. 2023, ARA&A, 61, 65, doi: 10.1146/annurev-astro-071221-053453

Kourkchi, E., & Tully, R. B. 2017, ApJ, 843, 16, doi: 10.3847/1538-4357/aa76db

Kozmanyan, A., Bourdin, H., Mazzotta, P., Rasia, E., & Sereno, M. 2019, A&A, 621, A34, doi: 10.1051/0004-6361/201833879

Kravtsov, A. V., & Borgani, S. 2012, ARA&A, 50, 353, doi: 10.1146/annurev-astro-081811-125502

Kravtsov, A. V., Vikhlinin, A., & Nagai, D. 2006, ApJ, 650, 128, doi: 10.1086/506319

Lacy, M., Mason, B., Sarazin, C., et al. 2019, MNRAS, 483, L22, doi: 10.1093/mnrasl/sly215

Laganá, T. F., Martinet, N., Durret, F., et al. 2013, A&A, 555, A66, doi: 10.1051/0004-6361/201220423

Lau, E. T., Nagai, D., Avestruz, C., Nelson, K., & Vikhlinin, A. 2015, ApJ, 806, 68, doi: 10.1088/0004-637X/806/1/68

Le Brun, A. M. C., McCarthy, I. G., & Melin, J.-B. 2015, MNRAS, 451, 3868, doi: 10.1093/mnras/stv1172

Le Brun, A. M. C., McCarthy, I. G., Schaye, J., & Ponman, T. J. 2017, MNRAS, 466, 4442, doi: 10.1093/mnras/stw3361

Leach, S. M., Cardoso, J. F., Baccigalupi, C., et al. 2008, A&A, 491, 597, doi: 10.1051/0004-6361:200810116

Li, Y., Bryan, G. L., Ruszkowski, M., et al. 2015, ApJ, 811, 73, doi: 10.1088/0004-637X/811/2/73

Lim, S. H., Mo, H. J., Li, R., et al. 2018, ApJ, 854, 181, doi: 10.3847/1538-4357/aaaa21

Liu, W., Sun, M., Nulsen, P., et al. 2019, MNRAS, 484, 3376, doi: 10.1093/mnras/stz229

Locatelli, N., Ponti, G., Zheng, X., et al. 2024, A&A, 681, A78, doi: 10.1051/0004-6361/202347061

Lovisari, L., Reiprich, T. H., & Schellenberger, G. 2015, A&A, 573, A118, doi: 10.1051/0004-6361/201423954

Macquart, J. P., Prochaska, J. X., McQuinn, M., et al. 2020, Nature, 581, 391, doi: 10.1038/s41586-020-2300-2

Mantz, A. B., Allen, S. W., Morris, R. G., & Schmidt, R. W. 2016, MNRAS, 456, 4020, doi: 10.1093/mnras/stv2899

Marrone, D. P., Smith, G. P., Okabe, N., et al. 2012, ApJ, 754, 119, doi: 10.1088/0004-637X/754/2/119

Mathur, S., Das, S., Gupta, A., & Krongold, Y. 2023, MNRAS, 525, L11, doi: 10.1093/mnrasl/slad085

McCarthy, F., & Hill, J. C. 2024, PhRvD, 109, 023528, doi: 10.1103/PhysRevD.109.023528

McCarthy, F., Hill, J. C., Coulton, W. R., & Hogg, D. W. 2024, arXiv e-prints, arXiv:2404.03557, doi: 10.48550/arXiv.2404.03557

McCarthy, I. G., Schaye, J., Bird, S., & Le Brun, A. M. C. 2017, MNRAS, 465, 2936, doi: 10.1093/mnras/stw2792

McCarthy, I. G., Schaye, J., Bower, R. G., et al. 2011, MNRAS, 412, 1965, doi: 10.1111/j.1365-2966.2010.18033.x

McDonald, M., Gaspari, M., McNamara, B. R., & Tremblay, G. R. 2018, ApJ, 858, 45, doi: 10.3847/1538-4357/aabace

McDonald, M., McNamara, B. R., Voit, G. M., et al. 2019, ApJ, 885, 63, doi: 10.3847/1538-4357/ab464c

McNamara, B. R., & Nulsen, P. E. J. 2007a, ARA&A, 45, 117, doi: 10.1146/annurev.astro.45.051806.110625

—. 2007b, ARA&A, 45, 117, doi: 10.1146/annurev.astro.45.051806.110625

Meece, G. R., Voit, G. M., & O'Shea, B. W. 2017, ApJ, 841, 133, doi: 10.3847/1538-4357/aa6fb1

Mukherjee, S., Bhattacharjee, A., Chatterjee, S., Newman, J. A., & Yan, R. 2019, ApJ, 872, 35, doi: 10.3847/1538-4357/aaf9b7

Mulchaey, J. S. 2000, ARA&A, 38, 289, doi: 10.1146/annurev.astro.38.1.289

Nagai, D. 2006, ApJ, 650, 538, doi: 10.1086/506467

Nagai, D., Kravtsov, A. V., & Vikhlinin, A. 2007, ApJ, 668, 1, doi: 10.1086/521328

Nicastro, F., Kaastra, J., Krongold, Y., et al. 2018, Nature, 558, 406, doi: 10.1038/s41586-018-0204-1

Nicastro, F., Krongold, Y., Fang, T., et al. 2023, ApJL, 955, L21, doi: 10.3847/2041-8213/acec70

Oppenheimer, B. D., Babul, A., Bahé, Y., Butsky, I. S., & McCarthy, I. G. 2021, Universe, 7, 209, doi: 10.3390/universe7070209

Pandey, S., Baxter, E. J., Xu, Z., et al. 2019, PhRvD, 100, 063519, doi: 10.1103/PhysRevD.100.063519

Pasini, T., Brüggen, M., de Gasperin, F., et al. 2020, MNRAS, 497, 2163, doi: 10.1093/mnras/staa2049

Paul, S., John, R. S., Gupta, P., & Kumar, H. 2017, MNRAS, 471, 2, doi: 10.1093/mnras/stx1488

Pfrommer, C., Springel, V., Enßlin, T. A., & Jubelgas, M. 2006, MNRAS, 367, 113, doi: 10.1111/j.1365-2966.2005.09953.x

Piffaretti, R., Arnaud, M., Pratt, G. W., Pointecouteau, E., & Melin, J. B. 2011, A&A, 534, A109, doi: 10.1051/0004-6361/201015377

Planck Collaboration, Ade, P. A. R., Aghanim, N., et al. 2011a, A&A, 536, A1, doi: 10.1051/0004-6361/201116464

—. 2011b, A&A, 536, A11, doi: 10.1051/0004-6361/201116458

—. 2013a, A&A, 550, A131, doi: 10.1051/0004-6361/201220040

—. 2013b, A&A, 554, A140, doi: 10.1051/0004-6361/201220247

—. 2014a, A&A, 571, A20, doi: 10.1051/0004-6361/201321521

—. 2014b, A&A, 571, A1, doi: 10.1051/0004-6361/201321529

—. 2014c, A&A, 571, A28, doi: 10.1051/0004-6361/201321524

—. 2014d, A&A, 571, A29, doi: 10.1051/0004-6361/201321523

—. 2016a, A&A, 594, A27, doi: 10.1051/0004-6361/201525823

Planck Collaboration, Aghanim, N., Arnaud, M., et al. 2016b, A&A, 594, A22, doi: 10.1051/0004-6361/201525826

Planck Collaboration, Ade, P. A. R., Aghanim, N., et al. 2016c, A&A, 596, A101, doi: 10.1051/0004-6361/201527743

Planck Collaboration, Adam, R., Ade, P. A. R., et al. 2016d, A&A, 594, A1, doi: 10.1051/0004-6361/201527101

Planck Collaboration, Ade, P. A. R., Aghanim, N., et al. 2016e, A&A, 594, A26, doi: 10.1051/0004-6361/201526914

Planck Collaboration, Aghanim, N., Akrami, Y., et al. 2020a, A&A, 641, A1, doi: 10.1051/0004-6361/201833880

—. 2020b, A&A, 641, A6, doi: 10.1051/0004-6361/201833910

Planck Collaboration, Akrami, Y., Andersen, K. J., et al. 2020c, arXiv e-prints, arXiv:2007.04997. https://arxiv.org/abs/2007.04997

Planelles, S., Fabjan, D., Borgani, S., et al. 2017, MNRAS, 467, 3827, doi: 10.1093/mnras/stx318

Poutanen, T., Maino, D., Kurki-Suonio, H., Keihänen, E., & Hivon, E. 2004, MNRAS, 353, 43, doi: 10.1111/j.1365-2966.2004.08043.x

Prasad, D., Voit, G. M., O'Shea, B. W., & Glines, F. 2020, ApJ, 905, 50, doi: 10.3847/1538-4357/abc33c

Pratt, C. T., & Bregman, J. N. 2020, ApJ, 890, 156, doi: 10.3847/1538-4357/ab6e6c

Pratt, C. T., Qu, Z., & Bregman, J. N. 2021, ApJ, 920, 104, doi: 10.3847/1538-4357/ac1796

Pratt, C. T., Qu, Z., Bregman, J. N., & Miller, C. J. 2024, ApJ, 964, 122, doi: 10.3847/1538-4357/ad24f9

Pratt, G. W., Croston, J. H., Arnaud, M., & Böhringer, H. 2009, A&A, 498, 361, doi: 10.1051/0004-6361/200810994

Remazeilles, M., Aghanim, N., & Douspis, M. 2013, MNRAS, 430, 370, doi: 10.1093/mnras/sts636

Remazeilles, M., Delabrouille, J., & Cardoso, J.-F. 2011, MNRAS, 410, 2481, doi: 10.1111/j.1365-2966.2010.17624.x

Rephaeli, Y., Sadeh, S., & Shimon, M. 2006, Nuovo Cimento Rivista Serie, 29, 1, doi: 10.1393/ncr/i2007-10015-9

Rossetti, M., & Molendi, S. 2010, A&A, 510, A83, doi: 10.1051/0004-6361/200913156

Roychowdhury, S., Ruszkowski, M., & Nath, B. B. 2005, ApJ, 634, 90, doi: 10.1086/496910

Roychowdhury, S., Ruszkowski, M., Nath, B. B., & Begelman, M. C. 2004, ApJ, 615, 681, doi: 10.1086/424502

Rozo, E., Vikhlinin, A., & More, S. 2012, ApJ, 760, 67, doi: 10.1088/0004-637X/760/1/67

Russell, H. R., McNamara, B. R., Fabian, A. C., et al. 2019, MNRAS, 490, 3025, doi: 10.1093/mnras/stz2719

Ryu, D., Kang, H., Hallman, E., & Jones, T. W. 2003, ApJ, 593, 599, doi: 10.1086/376723

Sarkar, A., Su, Y., Randall, S., et al. 2021, MNRAS, 501, 3767, doi: 10.1093/mnras/staa3858

Sayers, J., Czakon, N. G., Mantz, A., et al. 2013, ApJ, 768, 177, doi: 10.1088/0004-637X/768/2/177

Sehgal, N., Bode, P., Das, S., et al. 2010, ApJ, 709, 920, doi: 10.1088/0004-637X/709/2/920

Sereno, M., Umetsu, K., Ettori, S., et al. 2020, MNRAS, 492, 4528, doi: 10.1093/mnras/stz3425

Shallue, C. J., & Vanderburg, A. 2018, AJ, 155, 94, doi: 10.3847/1538-3881/aa9e09

Shimon, M., & Rephaeli, Y. 2004, NewA, 9, 69, doi: 10.1016/j.newast.2003.08.003

Shull, J. M., Smith, B. D., & Danforth, C. W. 2012, ApJ, 759, 23, doi: 10.1088/0004-637X/759/1/23

Stein, G., Alvarez, M. A., Bond, J. R., van Engelen, A., & Battaglia, N. 2020, JCAP, 2020, 012, doi: 10.1088/1475-7516/2020/10/012

Stern, J., Fielding, D., Faucher-Giguère, C.-A., & Quataert, E. 2019, MNRAS, 488, 2549, doi: 10.1093/mnras/stz1859

Stocke, J. T., Penton, S. V., Danforth, C. W., et al. 2006, ApJ, 641, 217, doi: 10.1086/500386

Stocke, J. T., Keeney, B. A., Danforth, C. W., et al. 2014, ApJ, 791, 128, doi: 10.1088/0004-637X/791/2/128

Sun, M., Voit, G. M., Donahue, M., et al. 2009, ApJ, 693, 1142, doi: 10.1088/0004-637X/693/2/1142

Sunyaev, R. A., & Zeldovich, Y. B. 1970, Ap&SS, 7, 3, doi: 10.1007/BF00653471

—. 1972, Comments on Astrophysics and Space Physics, 4, 173

Thölken, S., Lovisari, L., Reiprich, T. H., & Hasenbusch, J. 2016, A&A, 592, A37, doi: 10.1051/0004-6361/201527608

Thorne, B., Dunkley, J., Alonso, D., & Næss, S. 2017, MNRAS, 469, 2821, doi: 10.1093/mnras/stx949

Tremblay, G. R., Combes, F., Oonk, J. B. R., et al. 2018, ApJ, 865, 13, doi: 10.3847/1538-4357/aad6dd

Tripp, T. M., Sembach, K. R., Bowen, D. V., et al. 2008, ApJS, 177, 39, doi: 10.1086/587486

Tröster, T., Ferguson, C., Harnois-Déraps, J., & McCarthy, I. G. 2019, MNRAS, 487, L24, doi: 10.1093/mnrasl/slz075

Truong, N., Rasia, E., Mazzotta, P., et al. 2018, MNRAS, 474, 4089, doi: 10.1093/mnras/stx2927

Tully, R. B. 2015a, AJ, 149, 171, doi: 10.1088/0004-6256/149/5/171

—. 2015b, AJ, 149, 54, doi: 10.1088/0004-6256/149/2/54

Tully, R. B., Courtois, H. M., & Sorce, J. G. 2016, AJ, 152, 50, doi: 10.3847/0004-6256/152/2/50

Tully, R. B., Shaya, E. J., Karachentsev, I. D., et al. 2008, ApJ, 676, 184, doi: 10.1086/527428

Tully, R. B., Courtois, H. M., Dolphin, A. E., et al. 2013, AJ, 146, 86, doi: 10.1088/0004-6256/146/4/86

Vazza, F., Brunetti, G., & Gheller, C. 2009, MNRAS, 395, 1333, doi: 10.1111/j.1365-2966.2009.14691.x

Vikhlinin, A., Kravtsov, A., Forman, W., et al. 2006, ApJ, 640, 691, doi: 10.1086/500288

Vikhlinin, A., Burenin, R. A., Ebeling, H., et al. 2009, ApJ, 692, 1033, doi: 10.1088/0004-637X/692/2/1033

Vikram, V., Lidz, A., & Jain, B. 2017, MNRAS, 467, 2315, doi: 10.1093/mnras/stw3311

Voskresenskaia, S., Meshcheryakov, A., & Lyskova, N. 2023, arXiv e-prints, arXiv:2309.17077. https://arxiv.org/abs/2309.17077

Wagner-Carena, S., Hopkins, M., Diaz Rivero, A., & Dvorkin, C. 2020, MNRAS, 494, 1507, doi: 10.1093/mnras/staa744

Weinberg, D. H., Miralda-Escudé, J., Hernquist, L., & Katz, N. 1997, ApJ, 490, 564, doi: 10.1086/304893

Weisskopf, M. C. 2003, Advances in Space Research, 32, 2005, doi: 10.1016/S0273-1177(03)90639-9

White, D. A., Jones, C., & Forman, W. 1997, MNRAS, 292, 419, doi: 10.1093/mnras/292.2.419

White, R. L., & Becker, R. H. 1992, ApJS, 79, 331, doi: 10.1086/191656

Xu, B., Wang, N., Chen, T., & Li, M. 2015, arXiv e-prints, arXiv:1505.00853, doi: 10.48550/arXiv.1505.00853

Zeldovich, Y. B., & Sunyaev, R. A. 1969, Ap&SS, 4, 301, doi: 10.1007/BF00661821

Zhang, C., Churazov, E., Dolag, K., Forman, W. R., & Zhuravleva, I. 2020, MNRAS, 494, 4539, doi: 10.1093/mnras/staa1013

Zhu, X.-P., Dai, J.-M., Bian, C.-J., et al. 2019, Ap&SS, 364, 55, doi: 10.1007/s10509-019-3540-1

Zonca, A., Singer, L., Lenz, D., et al. 2019, Journal of Open Source Software, 4, 1298, doi: 10.21105/joss.01298